A COMPLEX NETWORK APPROACH TO UNDERSTAND CLIMATE VARIABILITY

QingYi Feng

QingYi Feng
Institute for Marine and Atmospheric research Utrecht (IMAU)
Ocean and climate group

Present address:
Institute for Marine and Atmospheric research Utrecht (IMAU)
Utrecht University
P.O. Box 80005, 3508 TA Utrecht, The Netherlands
Q.Feng@uu.nl

ISBN: 978-94-6299-19-3
Printing: Ridderprint BV

A COMPLEX NETWORK APPROACH TO UNDERSTAND CLIMATE VARIABILITY

Toepassingen van Complexe Netwerktheorie in Klimaatdynamica

(met een samenvatting in het Nederlands)

Proefschrift

ter verkrijging van de graad van doctor aan de Universiteit Utrecht op gezag van de rector magnificus, prof.dr. G.J. van der Zwaan, ingevolge het besluit van het college voor promoties in het openbaar te verdedigen op

maandag 7 december 2015 des middags te 4.15 uur

door

QINGYI FENG

geboren op 3 juli 1986
te Ningyuan, China

PROMOTOR: Prof. dr. ir. H. A. Dijkstra

This thesis was accomplished with financial support from the LINC project (no. 289447) funded by the Marie-Curie ITN program (FP7-PEOPLE-2011-ITN) of the European Commission.

CONTENTS

SUMMARY xi

SAMENVATTING xiii

ZHAIYAO xv

1 INTRODUCTION 1
1.1 Climate Variability: Phenomena and Impacts 1
1.1.1 El Niño-Southern Oscillation 1
1.1.2 Atlantic Multidecadal Oscillation 4
1.1.3 The Atlantic MOC 5
1.1.4 Impact 7
1.2 Central Questions and Approach 8
1.3 Overview of this Thesis 9

2 COMPLEX NETWORKS IN CLIMATE 11
2.1 What is a Climate Network 11
2.2 Climate Network Reconstruction 13
2.2.1 Unweighted and undirected links 15
2.2.2 Weighted and directed links 16
2.3 Properties of Climate Networks 17
2.4 Data and Analysis Software 18
2.4.1 Data 18
2.4.2 Software 19

3 EARLY WARNING INDICATORS FOR THE ATLANTIC MOC COLLAPSE 21
3.1 Introduction 22
3.2 Models and Data 23
3.2.1 Idealized ocean model 23
3.2.2 FAMOUS model 27
3.3 Results from the Idealized Ocean Model 29
3.3.1 Equilibrium flows 29
3.3.2 Slowly forced flows 34
3.4 Results from the FAMOUS Model 36
3.5 Determine Optimal Observation Locations 42
3.6 Summary and Discussions 46

4 ARE NORTH ATLANTIC MULTIDECADAL SST ANOMALIES WESTWARD PROPAGATING? 49
4.1 Introduction . . . 50
4.2 Model and Data . . . 51
4.2.1 Idealized ocean model . . . 51
4.2.2 Observational data . . . 54
4.3 Results . . . 56
4.3.1 MICN versus PCCN . . . 56
4.3.2 Robustness tests . . . 59
4.4 Pattern Comparison . . . 61
4.5 Discussion . . . 64

5 CLIMATE NETWORK BASED STABILITY INDEX FOR EL NIÑO VARIABILITY 67
5.1 Introduction . . . 68
5.2 Model and Data . . . 70
5.2.1 ZC model . . . 70
5.2.2 The response of the ZC model to the red noise . . . 74
5.2.3 BJ index calculation . . . 76
5.3 Results . . . 77
5.3.1 From the ZC model . . . 77
5.3.2 From CMIP5 models . . . 81
5.3.3 From observational data . . . 83
5.4 Discussion . . . 85

6 IMPROVING THE SKILL OF EL NIÑO PREDICTIONS USING MACHINE LEARNING TECHNIQUES AND NETWORK MEASURES 87
6.1 Introduction . . . 88
6.2 Machine Learning Toolbox . . . 91
6.2.1 Algorithm overview . . . 91
6.2.2 Methods overview . . . 92
6.2.3 Data overview . . . 93
6.3 Results . . . 93
6.3.1 Prediction for El Niño events occurrence . . . 93
6.3.2 Prediction for NINO3.4 index development . . . 95
6.3.3 Prediction for ENSO Variability in 2014 . . . 99
6.4 Discussion . . . 101

7 SUMMARY AND DISCUSSION 103

BIBLIOGRAPHY 109

ACKNOWLEDGMENTS 121

CURRICULUM VITAE 123

LIST OF PUBLICATIONS 125

LIST OF FIGURES

Figure 1.1 A Guide to Climate Variability . . . 2
Figure 1.2 ENSO Indices . . . 3
Figure 1.3 El Niño Pattern . . . 3
Figure 1.4 AMO Index . . . 4
Figure 1.5 AMO Pattern . . . 5
Figure 1.6 Deep Ocean Circulations Overview . . . 6
Figure 1.7 Observed Atlantic MOC Anomalies . . . 7
Figure 1.8 Global Impacts of Climate Variability . . . 8
Figure 2.1 Network Demos . . . 12
Figure 2.2 Climate Network Visualization . . . 13
Figure 2.3 Climate Network Methodology . . . 14
Figure 2.4 Degree Field of a Climate Network . . . 17
Figure 2.5 Software Architecture of `pyunicorn` . . . 20
Figure 3.1 Bifurcation Diagram of the MOC Collapse . . . 27
Figure 3.2 FAMOUS Model of the MOC Collapse . . . 29
Figure 3.3 Degree Fields and Distributions of PCCNs . . . 30
Figure 3.4 Clustering Fields and Distributions of PCCNs . . . 31
Figure 3.5 EOF Patterns of Temperature Fields . . . 33
Figure 3.6 Results from Equilibrium Flows . . . 34
Figure 3.7 Results from Slowly Forced Flows . . . 35
Figure 3.8 Degree Fields of PCCNs . . . 37
Figure 3.9 EOF Patterns of MOC Fields . . . 38
Figure 3.10 Kurtosis Indicator Compared with Classic Indicators . . . 40
Figure 3.11 Determination of $max(K_d^{control})$ . . . 41
Figure 3.12 Kurtosis Indicator Reconstructed at Optimal Locations . . . 46
Figure 4.1 Schematic Diagram of the Oscillation Mechanism . . . 51
Figure 4.2 Hovmöller Diagrams of North Atlantic SST Anomalies . . . 55
Figure 4.3 North Atlantic Net Heat Flux Anomalies . . . 56
Figure 4.4 MICN versus PCCN . . . 57
Figure 4.5 Hovmöller Diagrams of Degree Fields . . . 58
Figure 4.6 Influence of Different Noise Levels . . . 59
Figure 4.7 Influence of Linear Detrending . . . 60
Figure 4.8 Conditional Hamming Distance . . . 62
Figure 4.9 Robustness Test of the Conditional Hamming Distance . . . 63
Figure 4.10 Pattern Comparison from Surrogate Data . . . 64
Figure 5.1 Stochastic Hopf Bifurcation . . . 69

Figure 5.2 Overview of the Coupled Ocean-Atmosphere System 71
Figure 5.3 Response of the ZC Model to the Red Noise 74
Figure 5.4 EOFs and PCs of the Wind Stress Residual 75
Figure 5.5 BJ Index Calculation 78
Figure 5.6 Degree Fields of PCCNs 79
Figure 5.7 Results from the ZC Model 80
Figure 5.8 Comparison of BJ index and S_d Index in CMIP5 Models 82
Figure 5.9 Results from Observational Data 84
Figure 6.1 Model Forecasts Overview in 2014 89
Figure 6.2 Climate Network Based El Niño Forecasting Scheme 90
Figure 6.3 Prediction for El Niño Events Occurrence 95
Figure 6.4 Prediction Accuracy of El Niño Events Occurrence 96
Figure 6.5 NINO3.4 Index Forecast Disappointment in 2014 97
Figure 6.6 NINO3.4 Index Forecast by ANN 98
Figure 6.7 Cross Validation of the NINO3.4 Index Forecast 99
Figure 6.8 Smoothed Prediction Results by ANNs and GP 100
Figure 6.9 Prediction for ENSO Variability in 2014 101

LIST OF TABLES

Table 3.1 Parameters of the Idealized Ocean Model for MOC 25
Table 3.2 Variance Explained by the EOFs 32
Table 3.3 Performance of Kurtosis Indicator from Zonal Sections Sets . 42
Table 3.4 Performance of Kurtosis Indicator from Single Zonal Sections 43
Table 3.5 Performance of Variance Indicator from Single Zonal Sections 44
Table 3.6 Performance of Autocorrelation Indicator from Single Zonal Sections 45
Table 3.7 Sensitivity Test of the Kurtosis Indicator 47
Table 4.1 Parameters of the Idealized Ocean Model for AMO 53

Table 5.1 Parameters of the ZC Model 73

FREQUENTLY USED ACRONYMS

AMO	Atlantic Multidecadal Oscillation
CN	Climate Network
ENSO	El Niño-Southern Oscillation
EOF	empirical orthogonal function
GCM	general circulation model
MICN	Mutual Information Climate Network
MOC	Meridional Overturning Circulation
PCCN	Pearson Correlation Climate Network
SST	sea surface temperature

SUMMARY

Climate variability, especially on the low frequency time scales (e.g. years to centuries), has considerable impact on society, particularly agriculture, fisheries, water resources, and recreation throughout recorded history. If we would like to make informed decisions about our own future, it is essential that we could identify, quantify, understand such climate variability, and then eventually predict it so as to minimize its negative consequences and maximize its positive ones.

Complex network theory has been successfully applied to many complex systems, and leads to the emergence of new research fields, such as Social Network and Biological Network. The idea of complex network also has been recently extended to climate studies which is referred to as Climate Network (CN). The novelty of complex network theory is that it maps out the topological features that are related to the physics of the dynamical systems. Therefore, CN is an innovative and powerful tool to investigate the patterns and the dynamics of climate variability.

In this thesis, several specific phenomena of climate variability are studied by using the techniques from complex network theory. The first one is the reduction of the Atlantic Meridional Overturning Circulation (MOC). We develop an early warning indicator for a future collapse of the Atlantic MOC. We explore the performance of this indicator using data both from an idealized ocean model and a general circulation model that show such a collapse. We also determine optimal observation locations through quality measures of the indicator, and show that one needs multiple sections in the Atlantic to have a high quality indicator of the MOC collapse.

The second phenomenon is the multidecadal variability associated with the Atlantic Multidecadal Oscillation (AMO). We investigate the existence of the westward propagation in the North Atlantic sea surface temperature (SST) observations. We reconstruct CNs by using a linear Pearson correlation measure and a nonlinear mutual information measure of spatial correlations between SST variations. Analysis of the topological properties of CNs shows that the nonlinear measure is better in capturing the main features of propagating patterns from the noisy SST signals than the linear ones, and that westward propagation of multidecadal SST anomalies indeed seems to occur in the North Atlantic.

The third phenomenon is the interannual variations of El Niño-Southern Oscillation (ENSO). One of the crucial aspects that is currently limiting the success of El Niño predictions is the stability of the slowly varying Pacific climate. We present a stability index which does not only efficiently monitor the changes in spatial correlations in the Pacific climate, but also can be evaluated by using only SST data. We show the difference in Pacific climate stability between the 1982 and 1997 El Niño

events, and argue that a strong El Niño event did not develop in 2014 because the Pacific climate was too stable.

In the end, we use the measures of CNs in a machine-learning approach to develop new schemes for El Niño prediction. We present one scheme that can give a skillful prediction for the occurrence of El Niño events one year ahead, and another scheme provides reasonable NINO3.4 index forecasts with a lead time of three months.

SAMENVATTING

Klimaatschommelingen hebben, vooral op de laagfrequente tijdschaal (bijv. jaren tot eeuwen), altijd al een aanzienlijke impact gehad op de maatschappij, vooral op landbouw, visserij, waterbronnen en recreatie. Als we afgewogen beslissingen over onze toekomst willen maken is het belangrijk om deze variaties in het klimaat te kunnen herkennen, kwantificeren, begrijpen en uiteindelijk te kunnen voorspellen om de negatieve gevolgen te beperken en de positieve gevolgen te kunnen benutten. Complexe netwerktheorie is succesvol toegepast op vele complexe systemen en leidt tot de opkomst van nieuwe onderzoeksgebieden, zoals sociale en biologische netwerken. Het idee van complexe netwerken is recentelijk ook uitgebreid naar klimaatstudies waar naar verwezen wordt als 'Climate Network' (CN). Het vernieuwende hiervan is dat de topologische kenmerken van een dergelijk netwerk gerelateerd zijn aan de fysica van het dynamische systeem dat het beschrijft. Daarom is CN een innovatief en krachtig middel om de patronen en de dynamica van klimaatschommelingen te onderzoeken.

In dit proefschrift worden verschillende specifieke verschijnselen in de variabiliteit van het klimaat bestudeerd door het gebruik van complexe netwerktheorie. Het eerste is de verzwakking van de Atlantic Meridional Overturning Circulation (MOC). We ontwikkelen een vroegtijdige waarschuwingsindicator voor een ineenstorting van de Atlantic MOC in de toekomst. We verkennen het vermogen van deze indicator door gebruik te maken van simulaties van een dergelijke ineenstorting met een geïdealiseerd model en een algemeen circulatiemodel. Door middel van de kwaliteit van de indicator bepalen we optimale observatielocaties en laten we zien dat er meerdere secties nodig zijn in de Atlantische oceaan om een hoge kwaliteit indicator te krijgen van de MOC ineenstorting.

Het tweede verschijnsel is de multidecadale schommeling geassocieerd met de Atlantic Multidecadal Oscillation (AMO). We onderzoeken het bestaan van westwaartse verplaatsing in de oppervlaktetemperatuur van de Noord-Atlantische Oceaan. Door middel van lineaire Pearson correlaties en een maat voor niet-lineaire mutual information wordt een CN opgesteld voor ruimtelijke correlaties van variaties in de oppervlaktetemperatuur. Analyse van de topologische eigenschappen van deze twee CN's laat zien dat de niet-lineaire maat, in vergelijking met de lineaire, de kenmerken van verplaatsende patronen in het temperatuurveld beter representeert en minder last heeft van de ruis op het signaal. Ook laat de analyse zien dat de westwaartse verplaatsing van multidecadale anomalieën in het temperatuurveld zich inderdaad voordoet in de Noord-Atlantische Oceaan.

Het derde verschijnsel betreft de interjaarlijkse variaties van El Niño-Southern Oscillation (ENSO). Één van de cruciale aspecten die het succes van El Niño voorspellingen momenteel beperken, is de stabiliteit van het langzaam variërende klimaat van de Pacifische Oceaan. We presenteren een stabiliteitsindex die niet alleen efficiënt de ruimtelijke correlaties monitort in de Pacifische Oceaan, maar ook geëvalueerd kan worden door alleen gebruik te maken van oppervlaktetemperatuurdata. We tonen het verschil aan tussen de stabiliteit van het Pacifisch klimaat tijdens de El Niño's van 1982 en 1997 en we betogen dat er in 2014 geen sterke El Niño was vanwege een te stabiel klimaat in de Pacifische Oceaan.

Als laatste gebruiken we de topologische eigenschappen van CN's in een machine-learning toepassing om zo nieuwe methoden te ontwikkelen voor El Niño voorspellingen. We presenteren één concept dat een jaar van tevoren een adequate voorspelling kan geven voor het ontwikkelen van El Niño. Een andere methode presenteert aannemelijke voorspellingen voor de NINO3.4 index met een doorlooptijd van drie maanden.

摘要 (ZHAIYAO)

在整个有记录的历史上，气候变化对社会，特别是农业、渔业、水资源以及人类的休闲娱乐都有着相当大的影响，尤其是在低频尺度上的变化（比如，从以“年”到以“世纪”为时间单位计的变化）。如果我们想对自己的未来做出明智的决定，如何识别、量化、理解这样的气候变化具有十分重要的意义，因为这样我们才能预测气候变化，从而最小化其消极的后果，并最大限度地发挥其积极的作用。

复杂网络理论已被成功地应用于许多复杂系统的研究中，从而催生了新的研究领域，如“社交网络”和“生物网络”。近年来，复杂网络的思路也延伸到了气候领域的研究中，被称为“气候网络”。复杂网络理论的新颖性在于，其充分运用了与网络相关的拓扑特征能映射出该动力系统物理特性的性质。因此，气候网络是一个极具创新的、功能强大的研究气候变化模式和动力学的工具。

在本论文中，我们运用复杂网络理论研究了一些具体气候变化的现象。第一个现象是大西洋经向翻转环流(Meridional Overturning Circulation，MOC)的减缓。我们建立了一个预警指标来监控大西洋经向翻转环流未来可能的崩盘（停止或反转）。我们使用了能模拟出大西洋经向翻转环流崩盘的理想化海洋模型和大气环流模型的数据来探讨这个预警指标的适用性，从而确定了监测大西洋经向翻转环流的最佳观测位置。结果显示，建立一个高质量的大西洋经向翻转环流崩盘的预警指标，我们需要多条横跨大西洋的观测线。

第二个现象是与大西洋年代际振荡(Atlantic Multidecadal Oscillation，AMO)相关的年代际气候变化。我们研究了北大西洋海水表面温度向西传播的存在性。我们运用了两种度量时间序列相关性的方法来建立气候网络，一种是线性的皮尔

逊相关(Pearson correlation)，另一种是非线性的互信息(mutual information)。通过分析这两种不同气候网络的拓扑性质，我们发现非线性的度量能更好地从比较嘈杂的海水表面温度的信号中捕捉到其传播模式的主要特点，并且海水表面温度异常的向西传播确实发生在北大西洋中。

第三个现象是厄尔尼诺-南方涛动的年际变化(El Niño-Southern Oscillation，ENSO)。当前限制厄尔尼诺准确预测的其中一个重要的因素是缓慢变化的太平洋气候的稳定性。我们提出了一个稳定性指标，不仅能有效地监视太平洋气候在空间相关性的变化，而且评估方式极其简单——仅使用海水表面温度的数据。通过这个指标，我们展示了 1982 年和 1997 年的厄尔尼诺现象存在着太平洋气候稳定性上的差异，并认为大型的厄尔尼诺事件并没有发生在 2014 年，是因为太平洋气候过于稳定。

最后，我们使用气候网络的度量数据结合机器学习的技术开发出了一套厄尔尼诺预测的新方案。在我们提出的一个方案中，厄尔尼诺事件的发生可以提前一年预测，而在另一个方案中，我们可以提前三个月提供合理的厄尔尼诺指数（NINO3.4）的预测。

1

INTRODUCTION

1.1 CLIMATE VARIABILITY: PHENOMENA AND IMPACTS

To understand climate variability, it is important to realize the phenomena differ not only at different time scales but also at different subsystems in the climate system. In practice, people tend to use different terms to describe climate variability at different time scales, as shown in Fig. 1.1: "weather" varies on shorter time-scales, like days to weeks; on time scales of years to decades, we enter the realm of "climate"; variability on time scales longer than a few decades is usually referred to as "climate change".

For each subsystem of the climate system, such as atmosphere, ocean, cryosphere, biosphere, and lithosphere, a response time scale can be obtained by perturbing the specific subsystem out of an equilibrium and then monitor how long it takes for it to reach equilibrium again [Dijkstra, 2013]. Such characteristic (or response) time scales of atmospheric processes range from a few seconds to a few days (e.g., precipitation and cyclones). For the ocean, these scales range from a few decades (e.g., the surface ocean circulation) to hundreds even thousands of years (e.g. deep ocean circulation).

An example of such variability is the Atlantic Multidecadal Oscillation (AMO) involving sea surface temperature variations in the North Atlantic Ocean. This variability can be coupled to changes in the Atlantic Meridional Overturning Circulation (MOC), which is the zonally integrated volume transport in the Atlantic. In addition, feedbacks between the different subsystems of the climate system may also introduce new time scales of variability. One of the most important examples is the coupling between the equatorial ocean and the global atmosphere, which introduces the interannual time scale of variability associated with the El Niño-Southern Oscillation (ENSO) phenomenon.

1.1.1 *El Niño-Southern Oscillation*

About once every four years, the sea surface temperature (SST) in the eastern equatorial Pacific increases by a few degrees over a period of about one year [Philander,

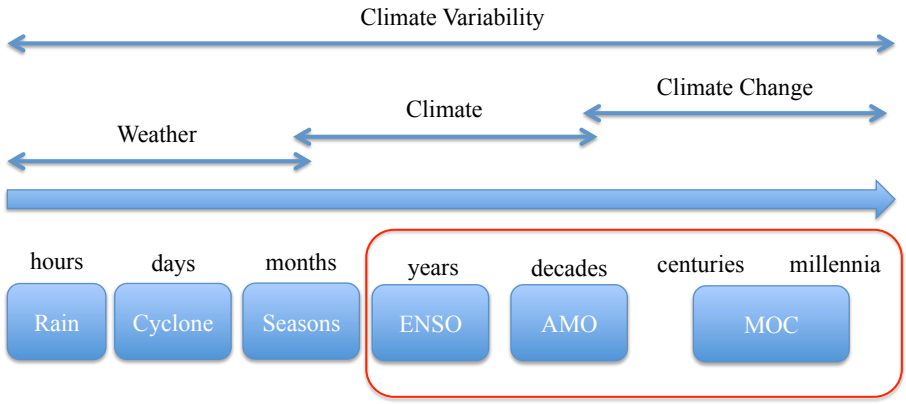

Figure 1.1: A guide to the timescales applicable to climate variability. The red cycle indicates the main topics of this thesis.

1990]. Near the South American coast, this warming of the ocean water is usually at its maximum around Christmas, and it is named after the "Christ Child" called "El Niño". This phenomenon arises through large-scale interaction between the Pacific Ocean and the overlying atmosphere, associated with variations in atmospheric pressure which are known as the "Southern Oscillation".

One measure of the temperature variations of the eastern equatorial Pacific is the NINO3.4 index, defined as the SST anomaly averaged over the region [120°W-170°W]×[5°S-5°N]. In the time series (blue curve in Fig. 1.2), the high NINO3.4 periods are known as El Niño's and the low NINO3.4 periods as La Niña's. The strongest El Niño were those of 1982/1983 and 1997/1998. Changes in the tropical atmospheric circulation are strongly connected to changes in SST, which can be captured by the Southern Oscillation Index (SOI) - the normalized difference of the pressure anomalies between Tahiti (18°S, 150°W) and Darwin (12°S, 131°E). The SOI is plotted as the red curve in Fig. 1.2, when this index is negative, the westward trade winds are weak and vice versa. The anti-correlation of the NINO3.4 index and the SOI is obvious from Fig. 1.2. As El Niño and the Southern Oscillation are one phenomenon, it is referred to as the El Niño-Southern Oscillation (ENSO) phenomenon.

ENSO is one the most prominent phenomena of climate variability on interannual time scales. It is also one of the best studied climate phenomena and its spatio-temporal development is well-known [Wallace et al., 1998]. The annual mean state of the equatorial Pacific SST is characterized by a "cold tongue" of 24°C water in the eastern Pacific and a "warm pool" of 30°C water near the western boundary of the Pacific basin. The pattern of the SST anomaly (with respect to this annual mean state)

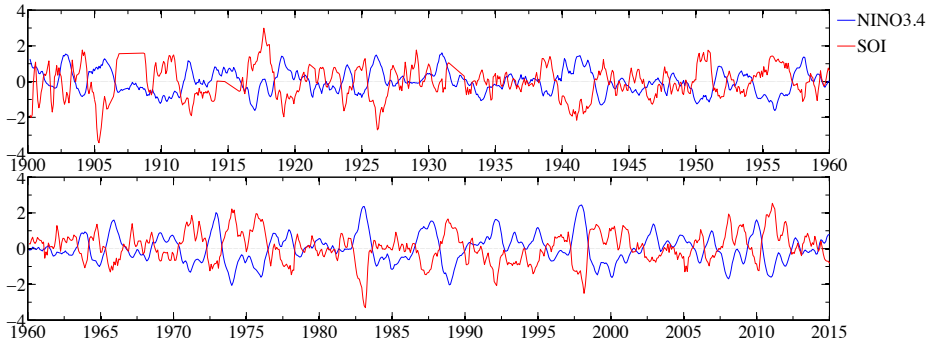

Figure 1.2: Time series of 3-month running mean NINO3.4 index (blue) and SOI (red) over the years 1900-2014. NINO3.4 index is from HadISST dataset [Rayner et al., 2003b] and SOI is provided by NCEP from `http://www.cpc.ncep.noaa.gov/`.

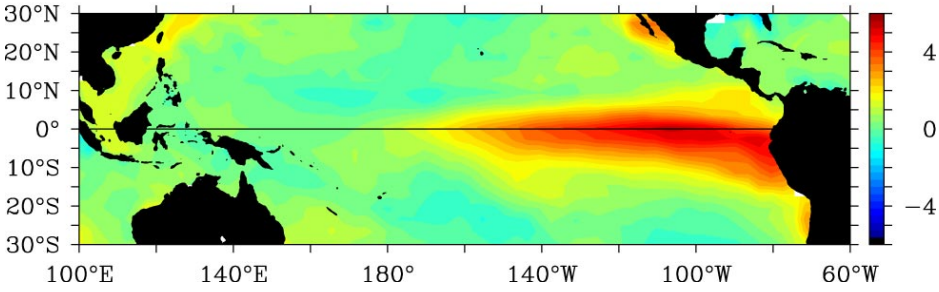

Figure 1.3: Sea-surface temperature anomaly field (with respect to the 1950-79 mean) of December 1997, at the height of the 1997/1998 El Niño. Figure from [McPhaden, 1999].

for December 1997 is plotted in Fig. 1.3 and shows the SST anomalies in the eastern Pacific exceeded 5°C.

The classical or conventional type of ENSO is also called Eastern Pacific (EP) ENSO [Kao and Yu, 2009]. However, in the last two decades, another type of ENSO was observed, in which the temperature anomaly near the South American coast is not affected, but an anomaly arises in the central Pacific [Larkin and Harrison, 2005]. This variant is called Central Pacific (CP) ENSO [Kao and Yu, 2009], "dateline" ENSO (because the anomaly arises near the dateline) [Yuan and Yan, 2013], or ENSO "Modoki" (Modoki is Japanese for "similar but different")[Cai and Cowan, 2009].

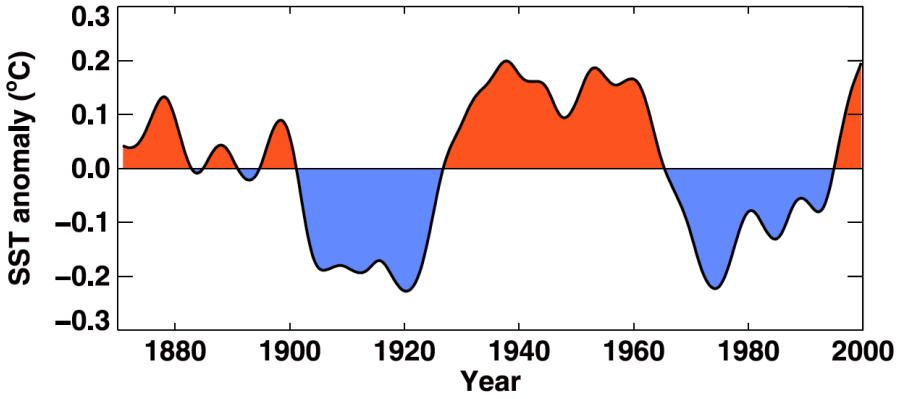

Figure 1.4: The AMO index derived from detrended area weighted mean North Atlantic SST anomalies by using the HadISST data set. Figure from [Knight et al., 2005].

1.1.2 *Atlantic Multidecadal Oscillation*

The North Atlantic SST appears to have a distinct signal of multidecadal variability. The first analyses of this variability was done by [Schlesinger and Ramankutty, 1994a] from a singular spectrum analysis of four global-mean temperature records. [Delworth and Mann, 2000a] extended the instrumental record with proxy data stretching back at least 300 years and demonstrated that there is a significant spectral peak in the 50-70 year frequency band. This variability was named the Atlantic Multidecadal Oscillation (AMO) by [Kerr, 2000], and an AMO index was defined by [Enfield et al., 2001a] as the ten-year running mean of detrended Atlantic SST anomalies north of the equator. An AMO index (the SST anomaly over the North Atlantic from 10°N - 70°N) is plotted in Fig. 1.4. Warm periods were in the 1940s and from 1995 onwards, whereas during the 1910s and 1970s the North Atlantic was relatively cold.

A first impression of the pattern of the AMO was obtained from an analysis of the instrumental SST record in the North Atlantic over the years 1950-1990. [Kushnir, 1994] found a specific pattern characterizing the difference between the years 1950-1964 and 1970-1984. Fig. 1.5 shows the difference between the average SST during the relatively warm years 1950-1964 and the relatively cool years 1970-1984. There is a negative SST anomaly near the coast of Newfoundland and a positive SST anomaly over the rest of the North Atlantic basin. Although the pattern of multidecadal variability has been characterized more accurately [Deser and Blackmon, 1993; Latif, 1998; Moron et al., 1998] by subsequent analysis of longer and better quality SST and sea level pressure (SLP), it is still difficult to extract a dominant pattern of multidecadal

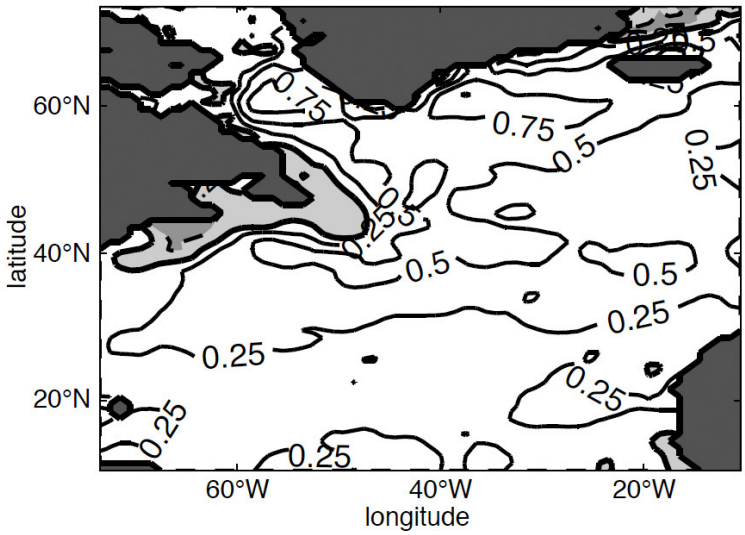

Figure 1.5: An impression of the AMO pattern as shown by the difference in observed average North Atlantic SST between the periods 1950-1964 (warm period) and 1970-1984 (cold period). Units are in °C and negative values are shaded. Figure from [Dijkstra, 2013].

variability with much confidence, because the observational time series is relatively short (about 150 year of SST and SLP).

1.1.3 *The Atlantic MOC*

The Atlantic Meridional Overturning Circulation (MOC) is a crucial component of the global ocean circulation as it is strongly coupled to meridional heat transport. In the North Atlantic, the Gulf Stream transports relatively warm and saline waters northwards, contributing to the relatively mild European climate. The heat is quickly taken up by the atmosphere, making the water denser. When there is strong cooling in winter, the water column becomes unstably stratified resulting in strong convection in certain areas (e.g., the Greenland Sea and the Labrador Sea). The net result of this process is the formation of a water mass called North Atlantic Deep Water (NADW), which overflows the various ridges that are present in the topography and enters the Atlantic basin.

A cartoon of the global ocean circulation is provided in Fig 1.6. The NADW flows southwards at mid depth in the Atlantic, enters the Southern Ocean and from there

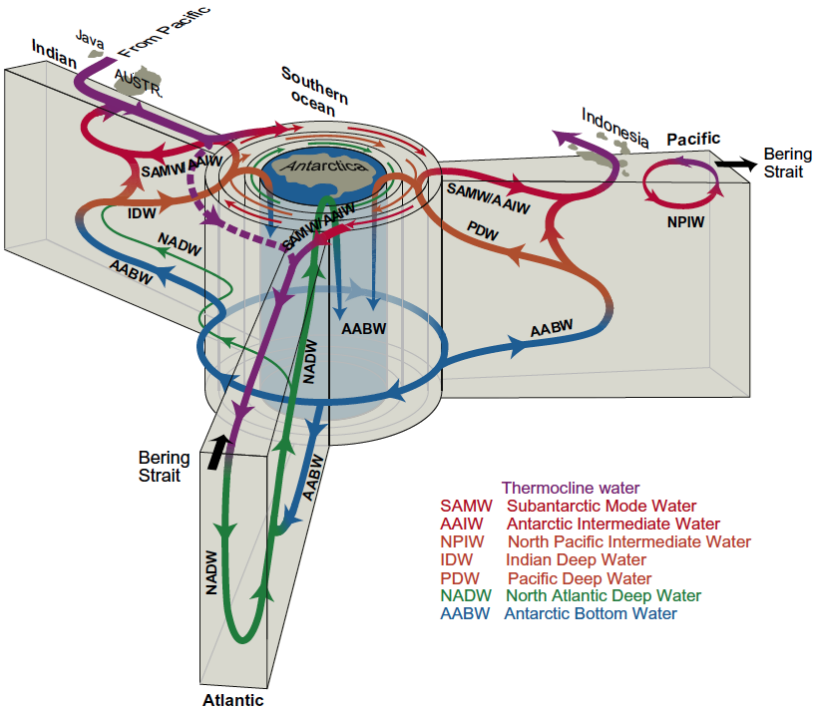

Figure 1.6: Highly idealized cartoon-type overview of the deep ocean circulations connecting the three major ocean basins with an indication of the various water masses involved in this flow. Figure from `http://asl.umbc.edu/pub/chepplew/OceanTD_intro.html`.

reaches the other ocean basins. Through upwelling in the Atlantic, Southern, Pacific and Indian Ocean, water is slowly brought back to the surface and the mass balance is closed by transporting back to the sinking areas in the North Atlantic. The MOC is the zonally averaged volume transport (at each latitude-depth) and its strength at 26°N in the Atlantic is now routinely monitored by the RAPID-MOCHA array [Cunningham et al., 2007]. The currently available time series of the Atlantic MOC strength is shown in Fig. 1.7, indicating the large amplitude variability, also a trend of slowing down.

During the last glacial period, large fluctuations in temperature occurred on Greenland with an average period of about 1,500 years [Bond et al., 1993]. These so-called Dansgaard-Oeschger events are thought to be caused by a rapid reduction in strength (or even reversal) of the MOC [Knutti et al., 2004; Rahmstorf, 1996]. Such an abrupt change is an example of a bifurcation point (or, more general, a tipping point).

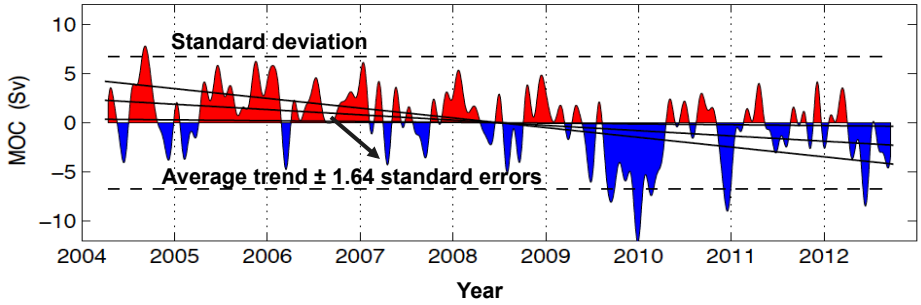

Figure 1.7: Observed MOC anomalies (positive is northward) relative to mean annual cycle. Figure from `http://www.rapid.ac.uk/rapidmoc/`.

1.1.4 *Impact*

The impacts of climate variability can be profound and global. A correlation map by [Muller et al., 2013] shows how AMO and ENSO influence the global surface temperature anomaly.

The influence of ENSO is locally strong, for example in the Indian Ocean, but also extends to the continents in the Southern Hemisphere. The effects of the CP ENSO are different from those of the conventional EP ENSO. The El Niño Modoki leads to more hurricanes and more frequently making landfall in the Atlantic [Kim et al., 2009]. The La Niña Modoki leads to a rainfall increase over northwestern Australia, rather than over the eastern part as in a conventional La Niña [Cai and Cowan, 2009].

The effect of AMO on the temperature is broadly distributed, and not just in Atlantic region, but also in Africa, southern Asia, and Canada. [Enfield et al., 2001a] showed that the AMO has a strong negative correlation with US continental rainfall, with less (more) rain over most of the central US during a high (low) AMO index period. [Sutton and Hodson, 2005a] found that sea level pressure, precipitation and temperature over Europe and North America, particularly during June-August, are affected by the AMO. Positive correlations have also been found between the AMO index and rainfall in the Sahel, the hurrican intensity in the Atlantic, and the strength of the Indian summer monsoon [Feng and Hu, 2008; Gray et al., 1997; Knight et al., 2006; Zhang and Delworth, 2006].

Model simulations of the global ocean circulation by [Jungclaus et al., 2005] also show that the low-frequency variability of the MOC contributes substantially to SST and sea-ice fluctuations in the North Atlantic. Due to the anthropogenic greenhouse forcing, the high-latitude temperature and precipitation is expected to increase [Meehl et al., 2007], as well as the freshwater input in the northern North Atlantic from the melting of the Greenland Ice Sheet. All the effects decrease the density of the polar

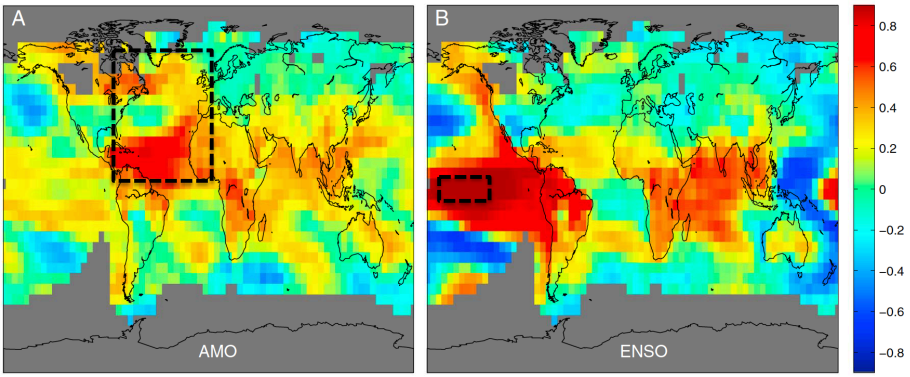

Figure 1.8: Short-term correlation maps of the (A) AMO index and (B) ENSO (NINO3.4) index 1950-2010 with the global surface temperature. Dashed black lines indicate the index areas, and colors show the degree of correlation at each location. Figure adopted from [Muller et al., 2013].

surface water, and therefore, the stability of the stratification increases and convective processes are inhibited, which may lead to a collapse of the Atlantic MOC. Such a reduction in Atlantic MOC is likely to have strong implications for the ENSO phenomenon [Timmermann et al., 2005], the position of the Intertropical Convergence Zone [Vellinga et al., 2002], the marine ecosystem in the Atlantic [Schmittner et al., 2005], and the sea level in the North Atlantic [Levermann et al., 2005].

1.2 CENTRAL QUESTIONS AND APPROACH

Climate variability, especially on the low frequency time scales (e.g. years to centuries), has considerable impact on society, particularly agriculture, fisheries, water resources, and recreation throughout recorded history [Committee et al., 1996]. If we would like to make informed decisions about our own future, it is essential that we could identify, quantify, understand such climate variability, and then eventually predict it so as to minimize its negative consequences and maximize its positive ones.

This thesis mainly focuses on the low frequency time scales of climate variability, especially the phenomena of the reduction of the Atlantic MOC, the multidecadal variability associated with the AMO, and the interannual variations of ENSO. As will be shown in later chapters, all these phenomena are connected to critical behavior, where climate feedbacks amplify perturbations, leading to transitions in behavior when critical boundaries are crossed. Important issues in such critical phenomena is to develop relatively simple indicators of the physical mechanisms of the transition

behavior to develop indicators which provide an early warning of the occurrence of rapid changes.

Over the last decade, complex network theory has been successfully applied to many complex systems, and leads to novel application areas, such as in sociology and biology [Dorogovtsev and Mendes, 2013; Wasserman, 1994]. The idea of complex network theory also has been recently extended to climate studies [Donges et al., 2009a; Tsonis and Swanson, 2006]. The innovation of complex network theory in the climate field is that a connection can be made between behavior in the climate system and topological changes in networks derived from observations and/or climate models. The main novel element in this thesis is to show that network theory can provide very useful information on specific critical phenomena of climate variability, such as ENSO and AMO variability and the reduction of the MOC.

With complex network theory as a new approach, we aim to answer the following questions:

(i) Can network based indicators be developed that provide useful "peaky" early warning indicators of a collapse of the Atlantic MOC?

(ii) Can network theory be used to identify patterns of low-frequency climate variability, such as the AMO, using the relatively short instrumental record?

(iii) Does network theory provide a possibility to develop indicators of the stability of the Pacific climate, important for the amplitude and development of ENSO?

(iv) Can network-based information be used to enhance the skill of ENSO prediction?

1.3 OVERVIEW OF THIS THESIS

The content of this thesis aims at answering the central questions above and answers to those questions are given in four chapters, each covering one question:

1. In **chapter 3**, we develop and explore the performance of an early warning indicator for a collapse of the Atlantic MOC, based on the changes in the topology of complex networks reconstructed from temperature or MOC time series.

2. In **chapter 4**, we investigate the existence of the westward propagation in the North Atlantic SST observations, by reconstructing complex networks using both a linear correlation measure (i. e. Pearson correlation) and a nonlinear correlation measure (i. e. mutual information).

3. In **chapter 5**, we develop a new index monitoring the stability of the Pacific climate which is a crucial aspect in predictions of the occurrence of El Niño variability. Although several indices have been developed in the past, the unique

feature of our complex network based index is that it can be evaluated by using only SST data.

4. In **chapter 6**, we present a machine learning toolbox using the measures of networks to improve the skill of El Niño predictions, especially for the occurrence of El Niño events and the development of NINO3.4 index.

Finally, **chapter 7** is a summary and discussion of the results of the whole thesis.

2

COMPLEX NETWORKS IN CLIMATE

2.1 WHAT IS A CLIMATE NETWORK

Network theory, derived from graph theory, is recognized as a structurally simple but informative representation of relations between the components in a dynamical system [Newman, 2010]. In the context of network theory, a complex network (Fig. 2.1b) is a graph (network) with non-trivial topological features which do not occur in simple networks such as regular lattices (Fig. 2.1a) or random graphs (Fig. 2.1c) [Kim and Wilhelm, 2008]. In most complex systems in nature, such as social, biological, and technological systems, the relations between their components display substantial non-trivial topological features that are neither purely regular nor purely random. The novelty of complex network theory is that it maps out the topological features that are related to the physics of the dynamical systems. Therefore, complex network theory is an innovative and powerful tool to investigate the structure and the dynamics of complex systems.

Complex network theory has now been successfully applied to many complex systems and revealed interesting mechanisms underlying their functions, for example, small-world networks [Watts and Strogatz, 1998] and scale-free networks [Barabási et al., 2009]. Such successful applications, particularly in sociology and biology, lead to the emergence of new concepts, such as Social Network [Wasserman, 1994] and Biological Network [Dorogovtsev and Mendes, 2013]. In recent years, the idea of complex network theory also has been extended to climate studies which is referred to as Climate Network (CN) [Donges et al., 2009a; Tsonis and Swanson, 2006]. A visualization of CN is shown in Fig. 2.2. It is reported that the CN also has small-world like global properties, scale-free like degree distributions, typical edge length distributions as well as distinctively different large-scale network structures [Tsonis and Roebber, 2004; Tsonis and Swanson, 2006; Tsonis, 2007].

In a CN, the nodes and links are not directly obvious such as in a social network or a biological network. For example, in a social network, people who participate in the network are considered as nodes, and the relationships between these people

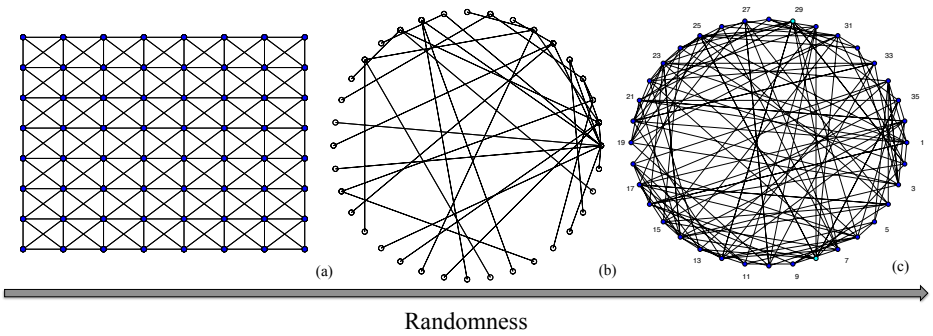

Figure 2.1: Network Demos sorted by increasing randomness starting from (a) a regular lattice, (b) a complex network like the Barabási-Albert scale-free network [Barabási and Albert, 1999] to (c) a fully random Erdos-Rényi graph [Erdös and Réyi, 1959]. All three networks are simple networks of 36 nodes.

naturally bring in the concept of "links"; while in climate systems, nodes and links are not so obvious. Depending on the availability of the climate data, nodes in a CN can be identified by the data points of a single time series, or by regular latitude-longitude grids or station data of spatiotemporal time series.

A nice overview on the definition of "nodes" in recent literature can be found in Tab. 3.1 of Donges' thesis [Donges, 2013]. The nodes in CNs are usually defined as locations on a longitude-latitude grid at various resolutions. The links in CNs are constructed based on the concept of "connectedness", which is determined with techniques from nonlinear time series analysis [Donner et al., 2011]. In general, there are two classes of these techniques:

1) work in the time domain (mainly for a single time series) and focus on studying stochastic properties of time series, for example, visibility graphs [Schleussner et al., 2015];

2) use graph representation for the similarity relationships between time series, such as correlation networks or interaction networks [Donges et al., 2009a; Mheen et al., 2013; Tsonis and Roebber, 2004] and ϵ-recurrence networks [Donner et al., 2010; Marwan et al., 2009].

Equipped with these techniques a CN defines a mapping from the time series of climate data to a graph (in the network domain), and then investigates the underlying dynamics of the climate system by interpreting changes in the topological properties of the graph.

In this thesis, the climate data that are used are spatiotemporal time series and the techniques we use for time series analysis are correlation based. Therefore, the nodes in our CNs are regular special grids (i.e., latitude-longitude) over the research

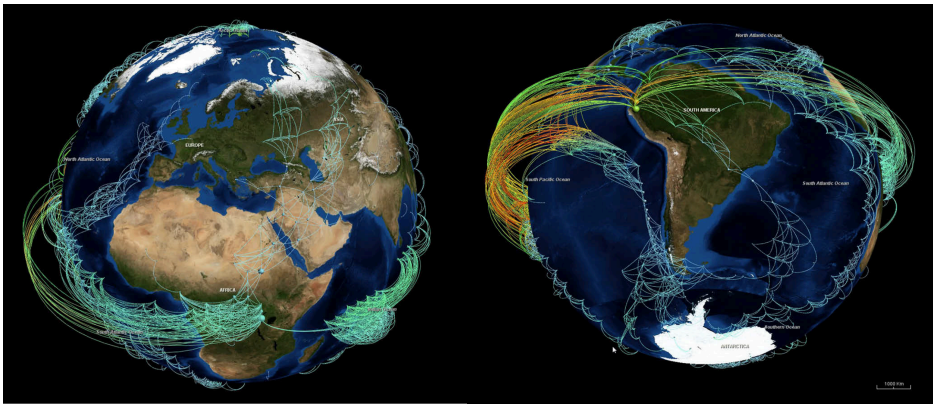

Figure 2.2: Visualization of a climate network taking into account the spatial embedding of vertices on the Earth's surface. Figure from [Tominski et al., 2011].

domains, and a link connecting two nodes is based on their similarity shared in climate variability, obtained from the degree of statistical correlation between the time series of observables (e.g. sea surface temperature (SST)).

2.2 CLIMATE NETWORK RECONSTRUCTION

Climate scientists have been long interested in studying the statistical correlation between climatological variables for gaining a good understanding of the large-scale dynamics of the climate system [Katz, 2002]. By investigating the correlation structures of global or regional fields of observables, such as surface air temperature, pressure, or geopotential height, a better view on spatial as well as temporal patterns accounting for a large fraction of the fields' variance could be given.

A CN based on statistical correlation offers a complementary way and novel insights by transferring the measures and techniques from complex network theory to the study of climate system dynamics. An overview of the methodology of reconstructing and analyzing CNs has been given by [Steinhaeuser et al., 2010]. As shown in Fig. 2.3, there are generally three steps of this methodology: first, create a network from gridded climate data; then, build links from correlations of the time series; next, investigate the dynamics of the climate system through the properties of the network.

There are many measures for quantifying the correlations of time series, here we name the types of CNs by the correlation measures. For instance, a Pearson Correlation Climate Network (PCCN) is the CN using Pearson correlation to quantify the correlations of time series, while a Mutual Information Climate Network (MICN) is using mutual information. Measures of different types of synchronization like phase

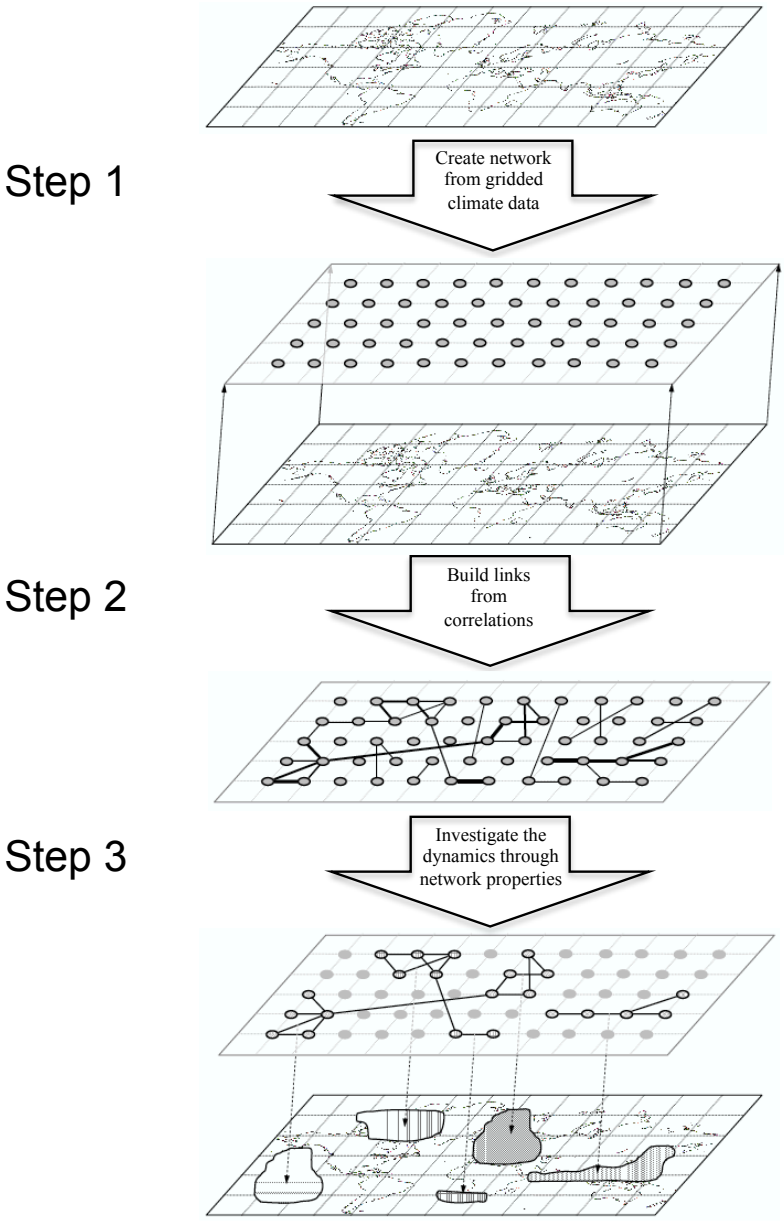

Figure 2.3: Step-by-step overview of Climate Network methodology. Figure adopted from [Steinhaeuser et al., 2010].

or generalized synchronization are also frequently used [Stolbova et al., 2014], but in this thesis, we only reconstruct the former two types of CNs.

Suppose that the observables like SST, either from observations, proxy reconstructions, reanalyses, or simulations, are gathered at fixed measurement stations, certain predefined regions, or grid cells, represented by a $n \times N$ matrix F, ordered in such a way that each column vector $\mathbf{p}_i = (p_i(t_1), \cdots, p_i(t_n))^T$ at a grid point $(i = 1, \ldots, N)$ contains a time series of length n.

To reconstruct a PCCN , the linear Pearson correlation coefficient is used to determine the correlation between the time series of observables at two grid points i and j. The elements R_{ij} of the correlation matrix R are given by

$$R_{ij} = \frac{\sum_{k=1}^{n} p_i(t_k) p_j(t_k)}{\sqrt{(\sum_{k=1}^{n} p_i^2(t_k))(\sum_{k=1}^{n} p_j^2(t_k))}}. \tag{2.1}$$

To reconstruct a MICN , the correlation between the time series of two grid points i and j is determined by the nonlinear mutual information coefficient. The elements R_{ij} of the correlation matrix R are then given by

$$R_{ij} = \sum_{x \in \mathbf{p_i}} \sum_{y \in \mathbf{p_j}} p(x,y) \ \log\left(\frac{p(x,y)}{p(x)p(y)}\right), \tag{2.2}$$

where $p(x,y)$ is the joint probability density function of events x and y and $p(x)$ and $p(y)$ are the marginal probability density functions.

If we take $\mathbf{R}$ as a generalized measure of quantifying the correlation between two time series represented by matrices F_1 and F_2 , the calculation of the correlation matrix R of CNs can be expressed by

$$R = \mathbf{R}(F_1, F_2). \tag{2.3}$$

Each grid point is seen as a node in a network and the link between a pair of nodes is determined by R. A link could be weighted/unweighted and directed/undirected. In this thesis, we mostly consider the links are unweighted and undirected when reconstructing a CN. However, we also use the results from the CN defined by [Gozolchiani et al., 2011; Wang et al., 2013], in which links are weighted and directed, for El Niño prediction in **chapter 6**.

2.2.1 *Unweighted and undirected links*

We consider that two nodes i and j have an unweighted link, if the absolute value of their correlation coefficient R_{ij} is above a certain threshold value τ, which gives a statistical significance above the 95% level. All links are then represented in the

$N \times N$ adjacency matrix A, which can be determined from the correlation matrix R as

$$A_{ij} = \mathscr{H}(|R_{ij}| - \tau), \tag{2.4}$$

where $\mathscr{H}$ is the Heaviside function.

From eq. 2.1 or eq. 2.2 one can see that the correlation matrix R at zero time lag both from PCCN and MICN are symmetric which is essential for defining an undirected link. However, if a lagged correlation is considered, then the correlation matrix $R^{\Delta t}$ at time lag Δt is then given by

$$R^{\Delta t} = \mathbf{R}(F^0, F^{\Delta t}), \tag{2.5}$$

where F^0 is the zero lag matrix and $F^{\Delta t}$ is the Δt lagged matrix. Because of the time lag, in general $R^{\Delta t}$ is asymmetric; to get undirected links, we can symmetrize $R^{\Delta t}$ through

$$\bar{R}^{\Delta t} = 0.5(R^{\Delta t} + (R^{\Delta t})^T), \tag{2.6}$$

2.2.2 *Weighted and directed links*

One way to define a weighted link between nodes i and j is to normalize the correlation function $\mathbf{R}$. An advantage of this method is that it overcomes the problem of strong auto-correlation values in the data [Guez et al., 2014], specifically when the link is calculated as the cross-correlation function $C_{ij}(\Delta t \geq 0)$, where Δt is the time lag and $C_{ij}(\Delta t) = C_{j,i}(-\Delta t)$.

In this way, a weighted and directed link between nodes i and j is defined by [Gozolchiani et al., 2011; Wang et al., 2013]. They take the time lag Δt^*, at which $C_{ij}(\Delta t)$ is maximal (or minimal), as the time delay between the time series of nodes i and j, and distinguish between positive and negative links and their weights as follows:

$$W_{ij}^{+} = \frac{\mathrm{MAX}(C_{ij}) - \mathrm{MEAN}(C_{ij})}{\mathrm{STD}(C_{ij})}, \tag{2.7}$$

and

$$W_{ij}^{-} = \frac{\mathrm{MIN}(C_{ij}) - \mathrm{MEAN}(C_{ij})}{\mathrm{STD}(C_{ij})}, \tag{2.8}$$

where MAX and MIN are the maximum and minimum values of the cross-correlation function, MEAN and STD are the mean and standard deviation.

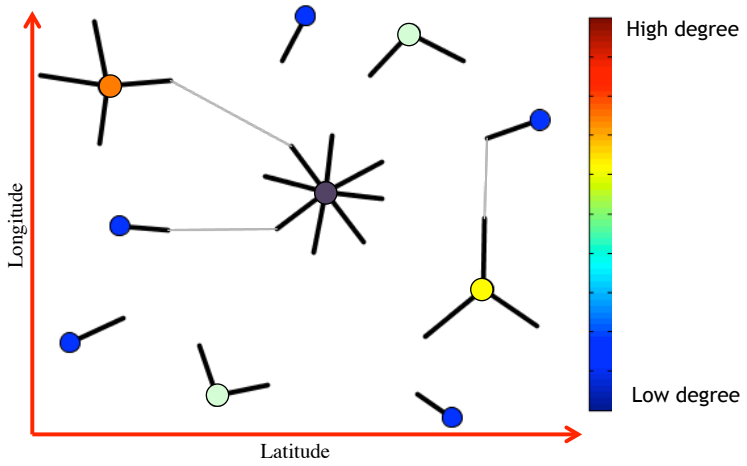

Figure 2.4: A sketch to demonstrate the degree field of a Climate Network.

2.3 PROPERTIES OF CLIMATE NETWORKS

By reconstructing CNs, we map the three-dimensional correlation structure of climate observables into a two-dimensional graph. Next step is to analyze the underlying dynamics of the climate system through changes in network properties. There is a good summary of network properties in Tab. 4.2 of Donges' thesis [Donges, 2013]. In this thesis, we mainly focus on the following properties:

Degree: A measure for the connectivity of a node i is given by the degree d_i given by

$$d_i = \sum_{j=1}^{N} A_{ij}. \tag{2.9}$$

The degree of a node measures the total number of links that a node possesses. Therefore, a higher degree means that a certain node is connected to a larger amount of other nodes in the network; in this thesis, we label it with warmer color, like red in Fig. 2.4; whereas a lower degree indicates that a node is more 'isolated' from the rest of the network, and we mark it with colder color, such as blue in Fig. 2.4.

Clustering coefficient: The extent to which nodes cluster together in a network is measured by the clustering coefficient. For the computation of the clustering coefficient c_i of node i, first all the nodes connected to node i, the k_i neighbors of node i, are determined. Next, the links Δ_i between these neighbors are calculated. For a

number of k_i neighbors the total possible connections between them is $k_i(k_i-1)/2$. The clustering coefficient c_i is then determined as

$$c_i = \frac{2\Delta_i}{k_i(k_i-1)} \tag{2.10}$$

A high value of c_i indicates that a lot of nodes in the neighborhood of node i are connected to each other, i.e., there is high clustering.

2.4 DATA AND ANALYSIS SOFTWARE

2.4.1 *Data*

For climate studies, in general, there are two types of data: recorded data, such as instrumental observations and proxy reconstructions, and simulated data from climate models. For example, for SST data, we mainly use Hadley Centre Sea Ice and Sea Surface Temperature (HadISST) dataset [Rayner et al., 2003b] as instrumental observations (in **chapter 4** and **chapter 5**). This SST data is provided by the Met Office Marine Data Bank, which is a combination of monthly globally complete fields of SST and sea ice concentration from 1871 onwards. We also use the extended reconstructed sea surface temperature (ERSST) [Smith and Reynolds, 2003] in **chapter 5** as proxy reconstructions. This dataset is a global monthly SST analysis derived from the International Comprehensive Ocean-Atmosphere Dataset with missing data filled in by statistical methods, which begins in January 1854 continuing to the present and includes anomalies computed with respect to a 1971-2000 monthly climatology.

As we cannot investigate most of the phenomena of climate variability in the laboratory, and observations are limited, climate models also provide important results for understanding the basic processes in the climate system. There is a wide rang of climate models in use, from "very simple" conceptual models to "very complex" state-of-the-art general circulation model (GCM)s. One way to classify climate models is based on the scales (both spatial and temporal) and processes (either physical, chemical or biological) taking place in the climate subsystems (atmosphere, ocean, cryosphere, biosphere, lithosphere) [Dijkstra, 2013].

The climate models with a limited number of scales and processes are usually referred to as conceptual models or idealized models. In these models only very specific interactions in the climate system are described. A typical example is the zonally-averaged ocean model to study the stability of the MOC, and we use this model in **chapter 3** to develop an early warning indicator for a future collapse of the Atlantic Meridional Overturning Circulation (MOC). We also use another idealized model in **chapter 4** to understand the mechanism of Atlantic Multidecadal Oscillation (AMO). Another example is the Zebiak-Cane model for studying the El Niño-Southern Oscillation (ENSO) phenomenon [Zebiak and Cane, 1987], and we use this model in **chapter 5**.

At the other extreme is the state-of-the-art GCMs which usually have a higher spatial resolution and include more processes. The outstanding example is the 5th Coupled Model Intercomparison Project (CMIP5) models. The CMIP5 is an internationally coordinated activity to perform climate model simulations for a common set of experiments across all the world's major climate modelling centres. In **chapter 3**, we use data from the Fast Met Office/UK Universities Simulator (FAMOUS) model which is a version of CMIP5 model provided by the Met Office – Hadley Centre Coupled Model version 3 (HadCM3), with a lower resolution ocean and atmosphere component [Hawkins et al., 2011]. In **chapter 5**, we use data from five different CMIP5 models: Coupled Physical Model version 3 (GFDL-CM3) and Earth System Models (GFDL-ESM2M) provided by Geophysical Fluid Dynamics Laboratory, ModelE/Russell coupled atmosphere-ocean model (GISS-E2-R) by NASA Goddard Institute for Space Studies, Norwegian Earth System Model (NorESM1-ME) by Norwegian Climate Centre, and Community Earth System Model version 4 (CCSM4) by National Center for Atmospheric Research.

2.4.2 *Software*

To provide a performant, modular and flexible way of reconstructing and analysing CNs, in this section [1], we give brief overview of the Python software package - `pyunicorn` (available at `https://github.com/pik-copan/pyunicorn`). This package implements concepts and techniques from complex network theory, as well as nonlinear time series analysis, and integrates these approaches to develop new innovative methodologies, such as functional networks like CNs, and network-based time series analysis [Donner et al., 2011].

With a focus on complex network theory, `pyunicorn` is a valuable complement to traditional non-linear time series analysis tools such as TISEAN [Hegger et al., 1999]. Its main mode of operation is to import, generate and export complex networks from time series or fields thereof, and to compute appropriate measures on these networks in order to derive insights about the causal structure and dynamical regimes of underlying processes. Fig. 2.5 shows two examples for the software architecture, one for recurrence networks [Donner et al., 2010; Marwan et al., 2009] (Fig. 2.5a) and the other for MICN (Fig. 2.5b).

Although the development of `pyunicorn` has mostly accompanied advances in climate research, the generality of the network approach and its extensions, such as spatio-temporal and time-delayed embedding, node weighted measures, coupled functional networks and recurrence networks, render this software package widely

1 Based on: 1. J. F. Donges, J. Heitzig, B. Beronov, M. Wiedermann, J. Runge, **Q. Y. Feng**, L. Tupikina, V. Stolbova, R. V. Donner, N. Marwan, H. A. Dijkstra, and J. Kurths. Unified Functional Network and Nonlinear Time Series Analysis for Complex Systems Science: The `pyunicorn` Package. *Chaos: An Interdisciplinary Journal of Nonlinear Science*, 2015 (resubmitted).

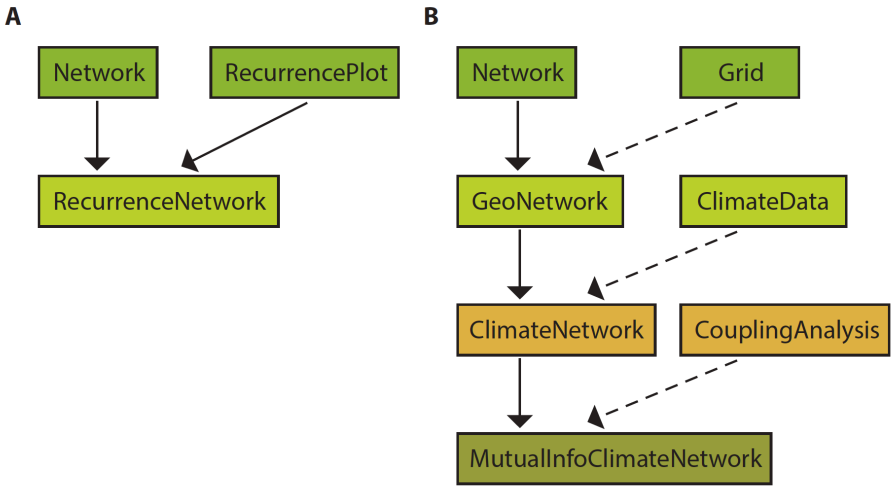

Figure 2.5: Examples for the software architecture of `pyunicorn` displayed as a Unified Modeling Language (UML) diagram of class relationships: ancestry of the `pyunicorn` class (A) `timeseries.RecurrenceNetwork` and (B) `climate.MutualInfoClimateNetwork`. Inheritance (class B inherits from class A, solid arrows) and object composition relationships (class B contains class A, dashed arrows) are indicated.

applicable in numerous fields, e.g. medicine, neuroscience, sociology, economics and finance.

The `pyunicorn` library is fully object-oriented and its inheritance and composition hierarchy reflects the relationships between the analysis methods in use (Fig. 2.5). As is usually the case with Python libraries, `pyunicorn` tries to provide simple interfaces and clear architecture, while delegating the heavy lifting to specialized tools for performance. The basic network measures and generative models are inherited from `igraph`. Wherever possible, numerically intensive computations are expressed as combinations of highly optimized linear algebra methods from `Numpy` and `Scipy`, and implemented in embedded C otherwise. Thus all costly computations are performed in compiled C, C++ or FORTRAN code.

Since `pyunicorn` internally represents networks as sparse adjacency matrices, it can handle relatively large data sets. However, when the number of nodes is larger than $\mathcal{O}(10^3)$, for example, reconstructing CNs from high-resolution climate model simulations output, this software may be bounded by the single-machine's memory and speed; in this case more specialized software has to be used [Ihshaish et al., 2015].

3

EARLY WARNING INDICATORS FOR THE ATLANTIC MOC COLLAPSE

A future collapse of the Atlantic Meridional Overturning Circulation (MOC) has been identified as one of the most dangerous tipping points in the climate system. It is therefore crucial to develop early warning indicators for such a potential collapse based on relatively short time series. So far, attempts to use indicators based on temporal correlations in single time series have been marginally successful. By reconstructing Climate Networks (CNs), this chapter presents a promising new indicator based on special correlations for the Atlantic MOC collapse that efficiently monitors spatial changes in deep ocean circulation. To demonstrate the application potential of the new indicator, the CN methodology is applied not only to temperature time series from an idealized ocean model of the Atlantic MOC, but also to Atlantic MOC strength time series from a coupled atmosphere-ocean general circulation model. Furthermore, through the analysis of the performance of this indicator, the optimal locations of measurement of the Atlantic MOC are formulated to provide early warning signals of a collapse. The results imply that an increase in spatial resolution of the Atlantic MOC observations (i.e., at more sections) can advance the detection, because the spatial coherence in the deep ocean arising near the transition is better captured.

This chapter has been published as:
[1] M. Van der Mheen , H. A. Dijkstra, A. Gozolchiani, M. Den Toom, **Q. Feng**, J. Kurths, and E. Hernandez-Garcia. Interaction network based early warning indicators for the Atlantic MOC collapse. *Geophysical Research Letters*, 2013, 40(11): 2714-2719. DOI: 10.1002/grl.50515.
[2] **Q. Y. Feng**, J. P. Viebahn, and H. A. Dijkstra. Deep Ocean Early Warning Signals of an Atlantic MOC Collapse. *Geophysical Research Letters*, 2014, 41(16): 6009-6015. DOI: 10.1002/2014GL061019.

3.1 INTRODUCTION

The Atlantic Meridional Overturning Circulation (MOC) is a crucial part of the climate system because of its associated northward heat transport [Ganachaud and Wunsch, 2000; Johns et al., 2011]. Since Stommel's seminal paper [Stommel, 1961] many model studies have shown that the Atlantic MOC may be sensitive to changes in the freshwater balance of the northern North Atlantic [Bryan, 1986]. When an anomalous freshwater flux is gradually applied over a broad swath in the subpolar North Atlantic, the Atlantic MOC collapses in many ocean-climate models [Rahmstorf et al., 2005]. Freshening of the surface waters in the Nordic and Labrador Seas inhibits the production of North Atlantic Deep Water (NADW), which feeds the deep southward branch of the Atlantic MOC. The Atlantic MOC collapse occurs due to the existence of a tipping point associated with the salt-advection feedback [Dijkstra and Ghil, 2005; Lenton, 2011].

The Atlantic MOC has been identified as one of the important tipping elements in the climate system [Lenton et al., 2008], as it may collapse to a state with a strongly reduced northward heat transport [Bryan, 1986; Rahmstorf, 2000]. Although there are studies which argue that such tipping point events are unlikely to occur within the 21st century [Tietsche et al., 2011], we should be modest in our confidence in this statement as state-of-the-art general circulation model (GCM)s have not been extensively tested for this behavior [Collins et al., 2013; Huisman et al., 2010].

Over the last few years there has been a growing interest in developing early warning indicators for proximity of tipping points in systems for which the external conditions change very slowly with time [Barnosky et al., 2012; Kuehn, 2011; Scheffer et al., 2009; 2012]. For the Atlantic MOC collapse problem, the slow change is caused by the gradually varying freshwater forcing in the northern North Atlantic.

Early warning indicators for regime shifts in ecosystems have been based on either temporal or spatial correlations [Donangelo et al., 2010], however, early warning indicators of the approach to the tipping point for the Atlantic MOC have so far been mostly based on temporal characteristics of the single time series [Held and Kleinen, 2004] or an ensemble of such time series [Livina and Lenton, 2007]. The techniques currently used (for an overview, see [Lenton, 2011]) are based on the concepts of critical slowdown (degenerate fingerprinting [Held and Kleinen, 2004], detrended fluctuation analysis [Livina and Lenton, 2007]) and the existence of multiple equilibria (potential analysis [Livina et al., 2011; 2010]).

Critical slowdown has been a key phrase in the detection of tipping points in ecosystems [Dakos et al., 2011] and the climate system [Lenton, 2011]. Indeed in many natural and man-made systems, there is an increase in response times to perturbations as a tipping point is approached [Scheffer et al., 2009]. Critical slowdown induces changes in variance and lag-1 autocorrelation in the time series that can be connected to the distance to the tipping point, and hence these quantities are frequently served as early warning indicators [Scheffer et al., 2009].

In this chapter, we present a new early warning indicator for the collapse of the Atlantic MOC which is based on spatial correlations. The Climate Network (CN) approach is one of the novel aspects of this indicator, which could effectively detect the changes in spatial correlations [Bialonski et al., 2011; Donges et al., 2009a; Gozolchiani et al., 2011; Tsonis and Roebber, 2004; Tsonis and Swanson, 2012]. In Section 3.2, we give a general overview on the models of the Atlantic MOC we used and the output data to reconstruct the CNs. The results from an idealized ocean model are presented in Section 3.3, and the ones from a coupled atmosphere-ocean GCM are presented in Section 3.4. In Section 3.5, we determine optimal observation locations through quality measures of the indicator. A summary and discussion of our results can be found in Section 3.6.

3.2 MODELS AND DATA

3.2.1 *Idealized ocean model*

To be able to develop an early warning indicator for detecting a tipping point of the MOC, it is beneficial to have a model where such tipping points can be explicitly computed. In [Den Toom et al., 2011], this is accomplished for a two-dimensional (meridional-depth) model of the Atlantic MOC.

The model is the B-grid version of the ThermoHaline Circulation Model [De Niet et al., 2007], which is a fully-implicit ocean-only model based on the hydrostatic primitive equations in spherical coordinates. A two-dimensional version is used here, as it has been shown that the bifurcation diagrams of two-dimensional and three-dimensional models (when only steady states are considered) are qualitatively the same [Weijer and Dijkstra, 2001]. There are two active tracers: temperature T and salinity S, which are related to the density ρ by a linear equation of state

$$\rho = \rho_0(1-\alpha_T(T-T_0)+\alpha_S(S-S_0)). \tag{3.1}$$

where α_T and α_S are the thermal expansion and haline contraction coefficients, respectively, and ρ_0, T_0, and S_0 are reference quantities.

In order to eliminate the longitudinal dependence from the problem, we consider a purely buoyancy-driven flow on a non-rotating Earth and prescribe free-slip conditions at the lateral boundaries (which avoids the necessity of boundary layer formation). We furthermore assume that inertia can be neglected in the meridional momentum equation. The mixing of momentum and tracers due to eddies is parameterized by simple anisotropic diffusion. The equations for the meridional velocity v, ver-

tical velocity w, pressure p, and the tracers T and S are given by (see e.g., [Den Toom et al., 2011])

$$\frac{1}{\rho_0 r_0}\frac{\partial p}{\partial \phi} - A_V\frac{\partial^2 v}{\partial z^2} = \frac{A_H}{r_0^2}\left(\frac{1}{\cos\phi}\frac{\partial}{\partial\phi}(\cos\phi\frac{\partial v}{\partial\phi}) + (1-\tan^2\phi)v\right), \quad (3.2a)$$

$$\frac{1}{\rho_0}\frac{\partial p}{\partial z} = g(\alpha_T T - \alpha_S S), \quad (3.2b)$$

$$0 = \frac{1}{r_0\cos\phi}\frac{\partial v\cos\phi}{\partial\phi} + \frac{\partial w}{\partial z}, \quad (3.2c)$$

$$\frac{\partial T}{\partial t} + \frac{v}{r_0}\frac{\partial T}{\partial\phi} + w\frac{\partial T}{\partial z} = \frac{K_H}{r_0^2\cos\phi}\frac{\partial}{\partial\phi}(\cos\phi\frac{\partial T}{\partial\phi}) + K_V\frac{\partial^2 T}{\partial z^2} + \mathrm{CA}(T), \quad (3.2d)$$

$$\frac{\partial S}{\partial t} + \frac{v}{r_0}\frac{\partial S}{\partial\phi} + w\frac{\partial S}{\partial z} = \frac{K_H}{r_0^2\cos\phi}\frac{\partial}{\partial\phi}(\cos\phi\frac{\partial S}{\partial\phi}) + K_V\frac{\partial^2 S}{\partial z^2} + \mathrm{CA}(S). \quad (3.2e)$$

Here t indicates time, ϕ latitude, z the vertical coordinate, r_0 the radius of Earth, g the acceleration due to gravity, A_H (A_V) the horizontal (vertical) eddy viscosity, and K_H (K_V) the horizontal (vertical) eddy diffusivity. The term CA represents convective adjustment.

The equations are solved on an equatorially symmetric, flat-bottomed domain. The basin is bounded by latitudes $\phi = \phi_S$ and $\phi = \phi_N$ (ϕ_S and ϕ_N are the southern and northern boundaries) and has depth D. In order to calculate transports, we assume it has a width of 64°. The resolution is 3.75° in the horizontal and 250 m in the vertical. Free-slip conditions apply at the lateral walls and at the bottom. Rigid lid conditions are assumed at the surface and atmospheric pressure is neglected. The wind stress is zero everywhere, and "mixed" boundary conditions apply for temperature and salinity,

$$K_V\frac{\partial T}{\partial z} = \frac{H_m}{\tau_T}(T_S(\phi) - T), \quad (3.3a)$$

$$K_V\frac{\partial S}{\partial z} = S_0 F_S(\phi). \quad (3.3b)$$

with $T_S(\phi) = 10.0\cos(\pi\phi/\phi_N)$. This formulation implies that temperatures in the upper model layer (of depth H_m) are relaxed to a prescribed profile T_S at a rate τ_T^{-1}, while salinity is forced by a net freshwater flux F_S, which is converted to an equivalent virtual salinity flux by multiplication with S_0. The surface freshwater forcing F_S is chosen as

$$F_S(\phi) = \frac{(\gamma+\eta)}{\cos\phi}\cos\pi\frac{\phi}{\phi_N} + \beta F_p(\phi) - Q \quad (3.4)$$

γ (in m/yr) is the strength of the background freshwater forcing and η is a white noise term, with $<\eta(t)\eta(t')>=\eta_0\delta(t-t')$. Furthermore, β is the strength of an

Table 3.1: *Fixed model parameters of the idealized ocean model.*

D	=	4.0×10^3	[m]	H_m	=	2.5×10^2	[m]
ϕ_N	=	$-\phi_S = 60°$		ρ_0	=	1.0×10^3	[kg m^{-3}]
r_0	=	6.371×10^6	[m]	T_0	=	15.0	[°C]
g	=	9.8	[m s^{-2}]	S_0	=	35.0	[psu]
A_H	=	2.2×10^{12}	[m^{2}s^{-1}]	α_T	=	1.0×10^{-4}	[K^{-1}]
A_V	=	1.0×10^{-3}	[m^{2}s^{-1}]	α_S	=	7.6×10^{-4}	[psu^{-1}]
K_H	=	1.0×10^3	[m^{2}s^{-1}]	ϵ	=	2.0×10^3	
K_V	=	1.0×10^{-4}	[m^{2}s^{-1}]	τ_T	=	75.0	[days]

anomalous freshwater flux which is only applied over the area $[40°\text{N}, 60°\text{N}]$ (where $F_p = 1$; it is zero elsewhere). With the area given over which the freshwater is applied, the total freshwater flux in m^3/yr is easily converted to Sv. The constant Q appears due to the requirement that the surface integrated salt flux is zero for all parameter values. Although in a crude way, these equations express that ocean-atmosphere interaction affects temperature and salinity in a fundamentally different way.

The introduction of CA is the only change to the model analyzed in section 3a of the paper by Weijer *et al.* [Weijer and Dijkstra, 2001]. It acts solely on the tracers and is implemented as enhanced diffusion, which for a tracer C takes the form

$$\text{CA}(C) = K_V F_0 \frac{\partial}{\partial z}(\mathscr{F}(\frac{D}{\rho_0}\frac{\partial \rho}{\partial z})\frac{\partial C}{\partial z}). \tag{3.5}$$

Here, F_0 is the efficiency of convection and $\mathscr{F}$ is a continuous approximation of the Heaviside step function,

$$\mathscr{F}(x) = \max(0, \tanh\left[(\epsilon x)^3\right]). \tag{3.6}$$

The steepness of the transition from 0 to 1 is determined by the selectivity ϵ; in the limit $\epsilon \to \infty$ the function $\mathscr{F}$ tends to the step function. The numerical values of the model parameters used (apart from those in the freshwater flux) are summarized in Table 3.1.

The spatially discretized model equations (on a meridional grid of N_x points and a vertical grid of N_z points) can be written in the form

$$\mathbf{M}\frac{d\mathbf{x}}{dt} = \mathbf{F}(\mathbf{x}) = \mathbf{L}(\mathbf{x}) + \mathbf{N}(\mathbf{x}, \mathbf{x}), \tag{3.7}$$

where the state vector $\mathbf{x}$ contains the unknowns (v, w, p, T, S) at each grid point and hence has dimension $d = 5 \times N_x \times N_z$. The operators $\mathbf{M}$ and $\mathbf{L}$ are linear and $\mathbf{N}$

represents the nonlinear terms in the equations. In the results of this model, we take equidistant grids, with $N_x = 32$, $N_z = 16$ which provides sufficiently accurate results for the bifurcation diagrams [Weijer and Dijkstra, 2001].

The meridional overturning stream function Ψ is defined by

$$w = \frac{1}{r_0 \cos\phi}\frac{\partial \Psi}{\partial \phi}, \tag{3.8a}$$

$$v\cos\phi = -\frac{\partial \Psi}{\partial z}. \tag{3.8b}$$

and provides a measure of the volume transport. To obtain the bifurcation diagrams, we determine steady solutions directly versus β using a pseudo-arclength continuation technique. From (3.7) it follows that steady state solutions can be found from the nonlinear algebraic equations

$$\mathbf{F}(\mathbf{x}, \beta) = 0. \tag{3.9}$$

To determine branches of steady solutions of the equations (3.9) as β is varied, the pseudo-arclength method [Keller, 1977] is used. The branches $(\mathbf{x}(s), \beta(s))$ are parameterized by an "arclength" parameter s. An additional equation is obtained by "normalizing" the tangent

$$\dot{\mathbf{x}}_0^T(\mathbf{x}-\mathbf{x}_0) + \dot{\beta}_0(\beta-\beta_0) - \Delta s = 0 \tag{3.10}$$

where $(\mathbf{x}_0, \beta_0)$ is an analytically known starting solution or a previously computed point on a particular branch and Δs is the step-length. Euler-Newton continuation is used to solve the system of equations (3.9-3.10).

For the transient simulations, we use a fully-implicit Crank-Nicholson [Atkinson, 1976] time integration scheme (which is second order in the time step Δt). Using a time index n, this scheme applied to (3.7) becomes

$$\mathbf{M}\frac{\mathbf{x}^{n+1}-\mathbf{x}^n}{\Delta t} = \frac{1}{2}(\mathbf{F}(\mathbf{x}^n) + \mathbf{F}(\mathbf{x}^{n+1})). \tag{3.11}$$

The equations for $\mathbf{x}^{n+1}$ are solved again by the Newton-Raphson technique and lead to the same type of numerical problems as that for the steady state computation. In the results of this model we take a time step Δt of approximately 0.1 year, which gives sufficiently accurate solutions.

For $\eta_0 = 0$ and $\gamma = 0.3$ m/yr, the so-called bifurcation diagram [Dijkstra and Ghil, 2005] in β is shown in Fig. 3.1a. In this diagram, a measure of the steady solutions of the model is plotted versus the forcing parameter β. The diagram contains two so-called saddle-node bifurcations (indicated by L_1 and L_2) connected by a branch of unstable steady states. The MOC patterns of the stable steady states for $\beta = 0$ are

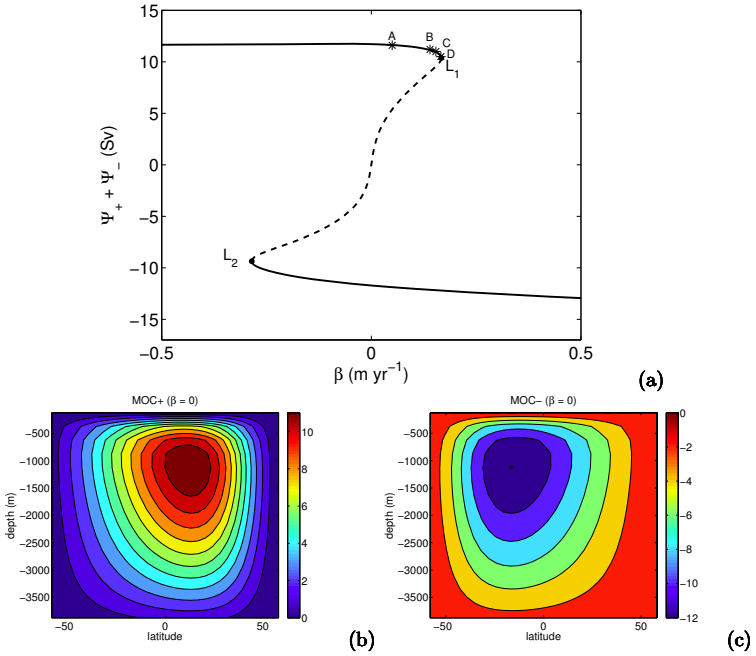

Figure 3.1: *(a) Bifurcation diagram in which the sum of the maximum (Ψ_+) meridional overturning stream function and minimum (Ψ_) meridional overturning stream function values is plotted versus the anomalous freshwater flux amplitude β. Solid (dashed) branches indicate stable (unstable) steady states. (b) Pattern of the meridional overturning stream function (Ψ) at the upper stable branch in (a) for $\beta = 0$. (c) Pattern of the meridional overturning stream function at the lower stable branch in (a) for $\beta = 0$.*

shown in Fig. 3.1b-c. We will focus on the upper tipping point indicated in Fig. 3.1a as the saddle-node bifurcation L_1.

Next, four values of β are chosen close to L_1, as indicated by the labels (A, B, C and D) in Fig. 3.1a. Starting from the steady state solution, transient computations over 500 years were performed for these values of β with a noise amplitude $\eta_0 = 0.1$. In these simulations the MOC fluctuates with a typical peak-to-peak amplitude of about 5 Sv.

3.2.2 *FAMOUS model*

The Fast Met Office/UK Universities Simulator (FAMOUS) model is a version of the HadCM3 (abbreviation for Hadley Centre Coupled Model, version 3, a coupled atmosphere-ocean GCM) with a lower resolution ocean and atmosphere component.

The model has horizontal resolution of 2.5° × 3.75° and a vertical resolution of 20 levels. The details of the model are described in Hawkins *et al.* [Hawkins et al., 2011]. For this study, we use the annual mean of MOC strength data from the control simulation and the freshwater perturbed (from now on referred to as 'hosing') simulation of the FAMOUS model.

In the hosing simulation, the freshwater flux over the extratropical North Atlantic is increased linearly from zero to 1.0 Sv (1 Sv $= 10^6$ m^{3}s^{-1}) over 2000 years [Hawkins et al., 2011]. Figure 3.2a displays the annual mean time series of the Atlantic MOC value at latitude 26°N and at 1000 m depth, the location of the maximum MOC before the collapse, for the control simulation (green curve) and the hosing simulation (blue curve). Whereas the control MOC values are statistically stationary over the 2000 year integration period, the MOC values for the hosing simulation show a rapid decrease between the years 800-1050.

We also use the MOC data from the FAMOUS simulations in which the freshwater flux was fixed after a certain integration time and the model was integrated to equilibrium [Hawkins et al., 2011]. Time series of the MOC of the last 100 years of these simulations were analyzed and the mean MOC values (again at 26°N and 1000 m depth) are plotted as the red dots labeled from 1 to 6 in Fig. 3.2a. Figure 3.2b-d show mean MOC streamfunction patterns of three of these equilibrium simulations (labelled with 1, 4 and 6 in Fig. 3.2a). Although the equilibrium value of the MOC decreases with larger freshwater inflow, the changes in the MOC pattern are relatively minor. For a slightly higher value of the freshwater flux than the one at point 6, the equilibrium solution is a collapsed state [Hawkins et al., 2011]. In the hosing simulation, the freshwater is, however, added relatively fast compared to the equilibration time scale of the MOC. Hence the MOC maintains its pattern for much higher freshwater inflow and collapses near 900 years (Fig. 3.2a). To determine a collapse time τ_c more precisely, we first determine the time with a Student t-test , say τ_s, at which the trend of the MOC time series of the hosing simulation deviates significantly ($p = 0.05$) from that of the control simulation. Subsequently, the standard deviation σ of the MOC values of the control simulation over the first τ_s years is computed. Next, the first time when the MOC anomaly value (with respect to the mean of the first τ_s years) in the hosing simulation decreases below - 3σ, we consider the MOC to start collapsing which defines τ_c. In the FAMOUS model, when considering the MOC values at 26°N and 1000 m depth, we find $\tau_s = 350$ years and $\tau_c = 874$ years which is shown as the red dashed line in Fig. 3.2a.

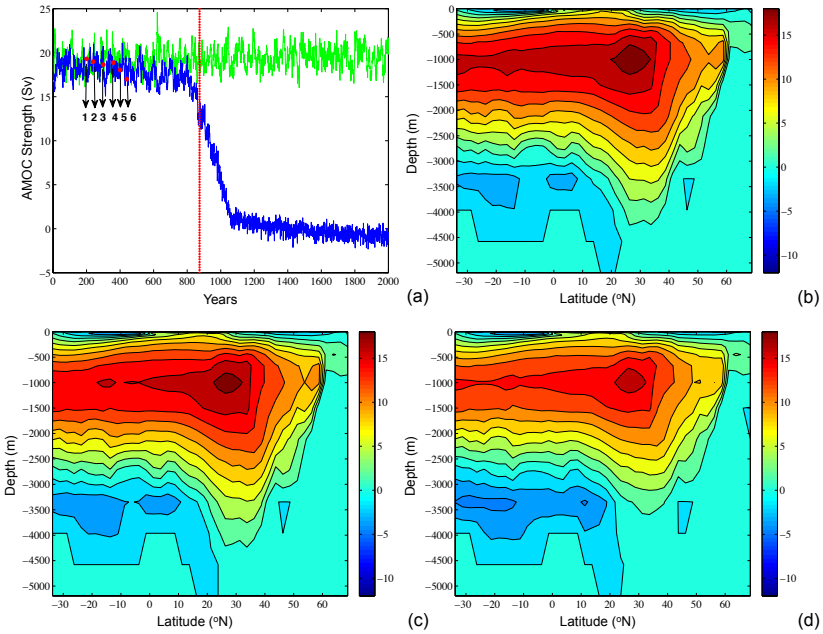

Figure 3.2: *(a) Time series of the MOC (in Sv, 1 Sv* $= 10^6\ m^3 s^{-1}$*) at 26°N and 1000m depth in the Atlantic for the control simulation (green curve) and the freshwater perturbed simulation (blue curve) of the FAMOUS model. The red dots labeled from 1 to 6 show the average values of MOC from the corresponding equilibrium simulations and the red broken line indicates the collapse time* $\tau_c = 874$ *years. (b) Annual mean MOC streamfunction pattern of equilibrium simulation 1. (c) Same as (b) but of equilibrium simulation 4. (d) Same as (b) but of equilibrium simulation 6.*

3.3 RESULTS FROM THE IDEALIZED OCEAN MODEL

3.3.1 *Equilibrium flows*

We first reconstruct Pearson Correlation Climate Network (PCCN)s using the temperature field time series at the different values of β (locations A, B, C and D in Fig. 3.1a). In the results below, we will analyze the topological properties of these PCCNs using threshold $\tau = 0.7$. The degree fields of these four PCCNs are shown in Fig. 3.3 (left panels). Note that the maximum degree of a node (connections to other nodes) is $d_{max} = 32 \times 16 - 1 = 511$. Relatively far from L_1, all temperature grid points have a relatively small degree. When β is increased, high degree first appears at nodes in the deep ocean. Close to L_1, there is a large area (below ∼1000 m) where the degree

values are very large and a relatively low degree only occurs for nodes located in the upper ocean, north of 30°N.

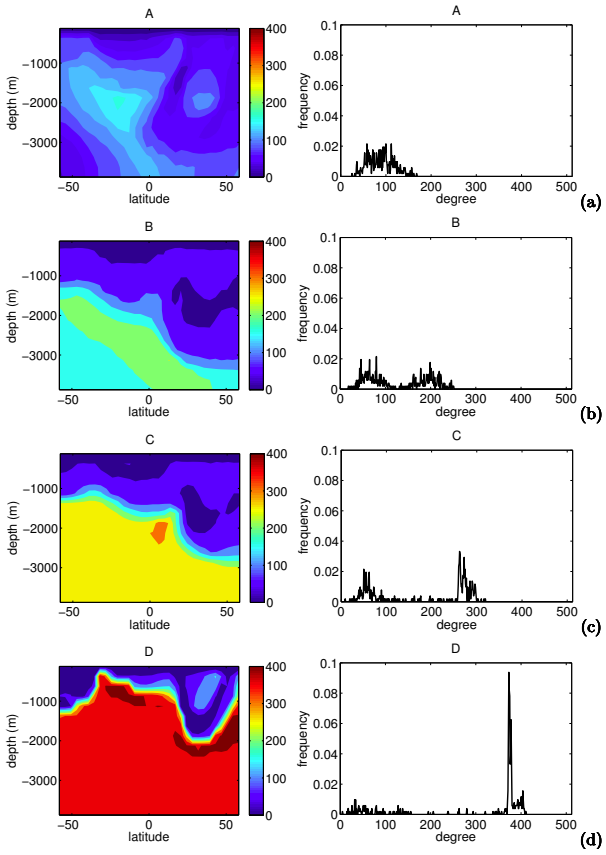

Figure 3.3: *Degree fields (left panel) and degree distributions (right panel) of the PCCNs (with a threshold $\tau = 0.7$) for the temperature field time series obtained at different locations A, B, C and D as indicated in Fig. 3.1a under transient noise ($\eta = 0.1$) forcing and $\gamma = 0.3$. (a) Point A: $\beta = 0.05$ m/yr; (b) Point B: $\beta = 0.139$ m/yr; (c) Point C: $\beta = 0.154$ m/yr; (d) Point D: $\beta = 0.166$ m/yr.*

The histograms of the degree fields (the degree distributions) for different β are also plotted in Fig. 3.3 (right panels). For relatively small β, the degree distribution is unimodal and the mean is located near $d = 100$. A second peak for $d = 200$ appears in Fig. 3.3b, where the degree distribution becomes bimodal and the maximum degree of the first peak shifts to slightly smaller values of d. This tendency strengthens in Fig. 3.3c, where the maximum of the second peak shifts to an even higher degree.

For location D, near L_1, about 10% of the grid points have a high degree of $d = 370$ (Fig. 3.3d). Also the clustering coefficient fields and the clustering coefficient distribution show the same pattern changes and peak shift with β (Fig. 3.4).

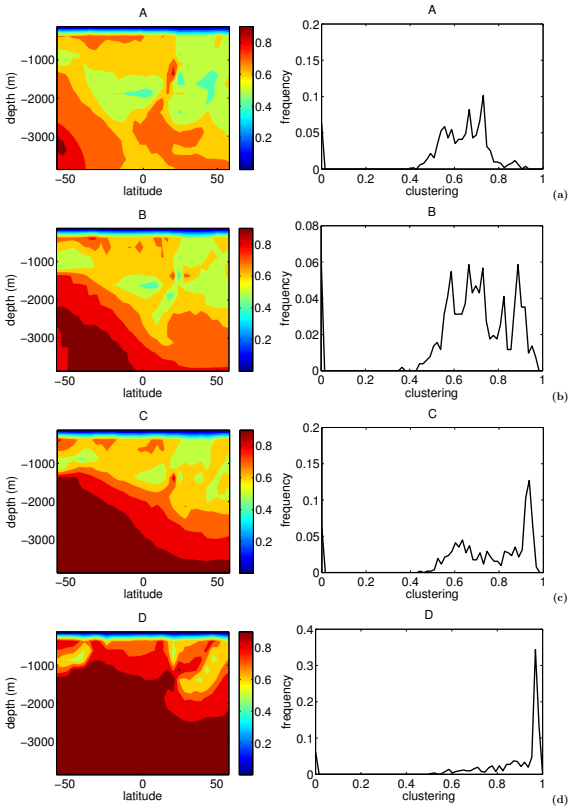

Figure 3.4: *Fields of the clustering coefficient (left panel) and clustering distributions (right panel) of the* PCCNs *(with a threshold $\tau = 0.7$) for the temperature field time series obtained at different locations A, B, C and D as indicated in Fig. 3.1a under transient noise ($\eta_0 = 0.1$) forcing and $\gamma = 0.3$. (a) Point A: $\beta = 0.05$ m/yr; (b) Point B: $\beta = 0.139$ m/yr; (c) Point C: $\beta = 0.154$ m/yr; (d) Point D: $\beta = 0.166$ m/yr.*

The results in Fig. 3.3 can be explained by looking at the changes in the first few empirical orthogonal function (EOF)s of the temperature field versus β. The patterns of the first three EOFs at locations *A* to *D* are shown in Fig. 3.5 with variances provided in Table 3.2. The first three EOFs account for about 90% of the variability in each case. It is interesting to see that from point A up to point C the first two EOFs of

Table 3.2: *Variance explained by each of the EOFs.*

Label	β (m/yr)	EOF1 (%)	EOF2 (%)	EOF3 (%)
A	0.05	49	32	13
B	0.14	47	31	13
C	0.154	45	29	17
D	0.166	60	21	13

the temperature decrease in importance, while the third one increases. In point D however, EOF1 increases from roughly 45% to 60%, EOF2 decreases from 29% to 21% and EOF3 from 17% to 13%. Hence, only very near L_1, the amount of variance explained by EOF1 increases rapidly. Temperature anomalies are most pronounced in the northern part of the domain and at the surface. When the variance would be completely dominated by only one EOF, it is easy to show that the network is fully connected and hence the degree of each node is maximal. The deviation maximal degree at each node is hence related to the relative variance explained by each of the EOFs at this node. When L_1 is approached, the amount of variance explained becomes dominated by EOF1 (in particular in the deeper ocean), and hence many nodes in the network will get a high degree and also a high clustering coefficient.

The results in Fig. 3.3 strongly motivate us to use properties of the degree distribution as early warning indicators of the approach to the tipping point. Although there are values of β where the degree distribution is clearly bimodal, near the tipping point this distribution is changing substantially and again becomes more unimodal. Hence, the expectation value E_d of the normalized degree distribution d/d_{max} is expected to show a strong shift towards larger values at L_1 is approached. A similar measure E_c is computed from the distribution of the clustering coefficients and both will be used as new indicators of early warning.

In Fig. 3.6, the indicator E_d shows a strong increase with β when the tipping point is approached (solid black curve). The same holds for the indicator E_c plotted as the dashed black curve in Fig. 3.6. As soon as $\beta > 0.14$ myr^{-1}, a new regime in spatial correlations appears where the degree and clustering distributions become dominated by high values in the deeper ocean. We also computed both indicators when only a part of the grid points are used to compute the degree distribution. The blue (red) curves in Fig. 3.6 arise when only the northern and southern (top and bottom) grid points are taken into account to reconstruct the PCCN. The indicator E_d reconstructed from the north-south grid points also smoothly increases with β (and

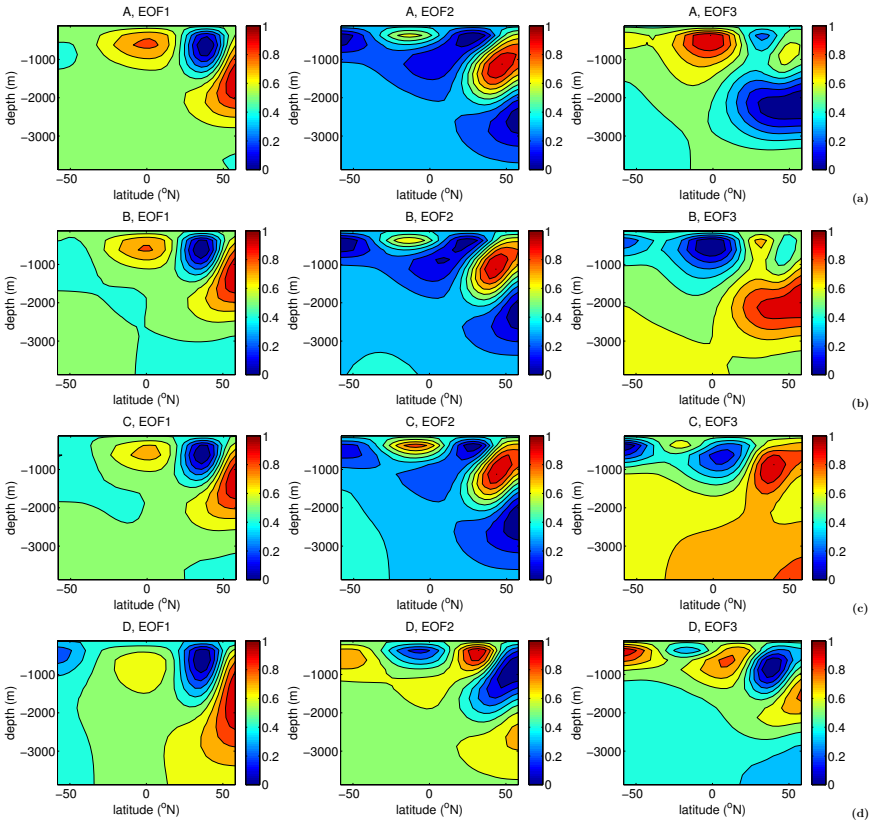

Figure 3.5: *Pattern of the first three EOFs of the temperature fields for the time series obtained at different values of β as indicated in Fig. 1a. (a) Point A: $\beta = 0.05$ m/yr; (b) Point B: $\beta = 0.14$ m/yr; (c) Point C: $\beta = 0.154$ m/yr; (d) Point D: $\beta = 0.166$ m/yr. The variance explained by each of the EOFs is shown in Table 3.2.*

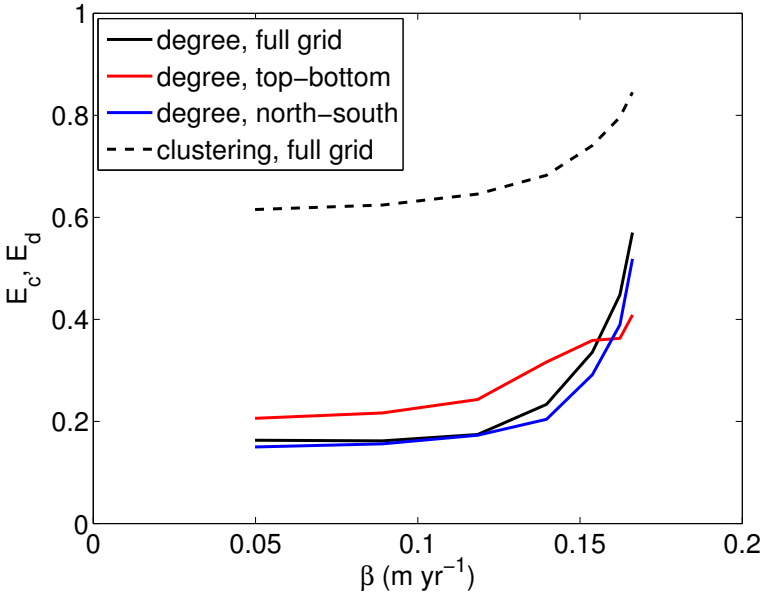

Figure 3.6: *Results from the equilibrium flow simulations. The expectation value E_d (solid) of the normalized degree distribution (d/d_{max}) and the expectation value E_c (dashed) of the distribution of the clustering coefficient versus β. The black curves are for all grid points. The red (blue) curve for the degree shows the indicators for a* PCCN *where only the bottom and top (northern and southern) boundary grid points of the domain are considered.*

has much better behavior than that for the top-bottom grid) as it captures the high spatial correlations in the deep ocean.

3.3.2 *Slowly forced flows*

We next investigated the performance of both indicators E_c and E_d in a transient simulation. Over a period of 35,000 year, β was linearly increased from 0.05 up to 0.17 m yr^{-1} (Fig. 3.7a) and again noise ($\eta_0 = 0.1$) was applied to the freshwater flux. When the zonal dimension of the basin is assumed to be 64°, this amounts to about 10^{-3} Sv/1000yr, which is comparable to other model studies [Rahmstorf et al., 2005]. A time series of the maximum value of the MOC (Fig. 3.7a) indicates that the MOC starts collapsing after about 27,000 year (indicated by the vertical dashed line in Fig. 3.7) when β approaches L_1. At this time, the actual value of $\beta = 0.142$ yr^{-1}

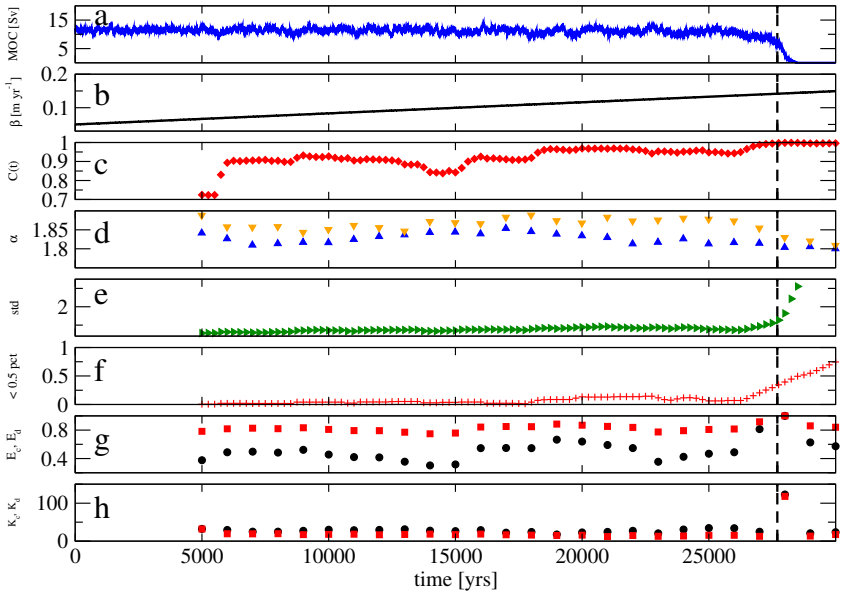

Figure 3.7: *Results from the slowly forced flow simulations. (a) Time series of the maximum value of the MOC. (b) Transient change of β versus time from 0.05 to 0.17 myr^{-1} in 35,000 years. (c) The (rescaled) lag-1 autocorrelation of the projection of the time series onto the first EOF. (d) Power of the fluctuation function, as determined by the DFA procedure, using linear (up marker) and quadratic (down marker) detrending. (e) Standard deviation of the MOC time series shown in (a). (f) Fraction of the time spent below the 0.5 percentile of the MOC amplitude. (g) Results from the CN based indicators E_d (circles) and E_c (squares) for the full network as in Fig. 3.6. (h) Same as (g) but now the kurtosis (K_d (circles) and K_c (squares)) is plotted. The vertical dashed line indicates the tipping point.*

which is slightly larger than the value of point B in Fig. 3.1a. Note that because point B is in the multiple equilibrium regime, the MOC can already decrease substantially under the presence of noise even before reaching L_1.

Previously suggested that early warning indicators of the transition in this MOC time series are plotted in panels (c-f) of Fig. 3.7. Below we present only the results for a sliding window of 5000 years, but the robustness of the results with respect to the sliding window (5,000-15,000) years was tested by using the Mann-Kendall trend test [Hamed and Rao, 1998; Lenton et al., 2012].

In Fig. 3.7c, the (rescaled) lag-1 autocorrelation of the projection of the time series onto the first EOF (degenerate fingerprinting) is plotted. Here, we used an aggregation window of 50 years. The first EOF is generated from results of the first 5000 years

of the simulation and the lagged autocorrelation is calculated in a time window of 5000 years. The coefficient reaches zero indeed near the transition showing a critical slowdown of the MOC. However, the indicator is not monotonic and also increases when the MOC is still far from the transition.

Fig. 3.7d shows the power of the fluctuation function, as determined by the detrended fluctuation analysis (DFA) procedure, using linear and quadratic detrending. The largest window taken in fitting the fluctuation function to a power law is 100 years. In most of the cases the fitting quality coefficient is close to 1 (perfect fit), and the typical error in the coefficient is 0.5 %. The quality of the sampling is assessed with respect to fluctuations of the measure during time. We have checked different orders of polynomial detrending in the DFA procedure, between 1 (linear) and 4 (quartic); the qualitative behavior is similar. The average power coefficient is 1.82, 1.85, 1.71 and 1.62, with respect to the 4 detrending orders 1–4, and there is no warning of a transition.

Fig. 3.7e gives the standard deviation of the MOC record. Each point is calculated using a sliding window of 5000 years with a shift of 200 years; it indeed shows a steady increase towards the transition but it is difficult to set a threshold for an alarm. In Fig. 3.7f, the fraction of the time spent below the 0.5 percentile (estimated based on the first 5000 year) of the MOC strength is plotted using the same sliding window as in Fig. 3.7e. This indicator displays a much sharper increase but it is a rather ad-hoc measure which also depends on a calibration in the far past.

Finally, the CN based indicators E_c and E_d are plotted in Fig. 3.7g and the kurtosis of the degree and clustering coefficient distributions in Fig. 3.7h. Both are determined by PCCNs reconstructed from the full spatial temperature field using a sliding window of 5000 years with a shift of 1000 years. Both indicators E_c and E_d exhibit similar behavior with an increase before the collapse. The kurtosis distributions (Fig. 3.7h) are even more clearly showing a strong increase before collapse. By considering reconstructed PCCNs for different sliding window lengths, it was found that the time at which the peak occurs in the indicators is not sensitive to a sliding window length in the range 5,000-15,000 years. Similar peaks are found in the standard deviation and skewness of both distributions. Of all the indicators considered, the CN based kurtosis indicators are least susceptible to cause false alarms of the MOC collapse.

3.4 RESULTS FROM THE FAMOUS MODEL

To further test the performance of the CN based indicators for the collapse of the Atlantic MOC, we use more realistic MOC time series from the FAMOUS model. The same as we did in Section 3.3.1, we first reconstruct PCCNs using the complete Atlantic MOC field for each of the six 100-year equilibrium simulations (red dots in Fig. 3.2a). Similar results are obtained as in Fig. 3.3 using PCCNs from the temperature field of the idealized ocean model, Fig. 3.8 shows the changes in the degree field at the equilib-

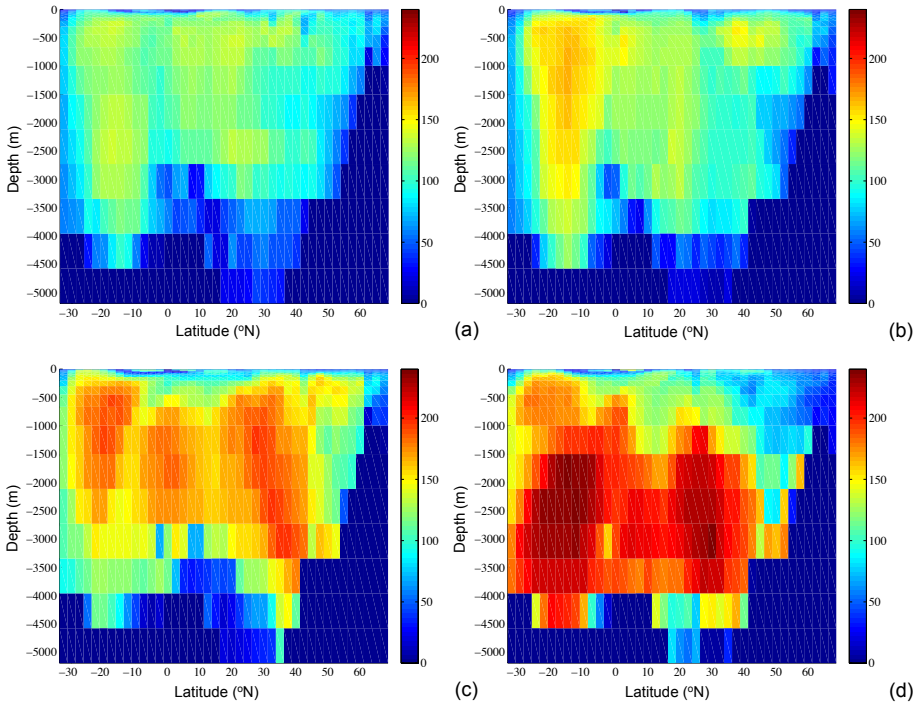

Figure 3.8: *(a) Degree field of the PCCN reconstructed from the MOC data of equilibrium simulation 1 in Fig. 3.2 a using a threshold* $\tau = 0.5$*. (b) Same as (a) but of equilibrium simulation 2. (c) Same as (a) but of equilibrium simulation 4. (d) Same as (a) of equilibrium simulation 6.*

rium solutions 1, 2, 4 and 6 in Fig. 3.2a are distinct. When the freshwater forcing is increased, high degree in the network – indicating high spatial MOC correlations – first appears at nodes in the South Atlantic at about 1000 m depth (Fig. 3.8a-b). It subsequently extends to the whole Atlantic with highest amplitudes in the deep ocean at midlatitudes (Fig. 3.8c-d).

The EOFs of the MOC field are shown in Fig. 3.9. The first EOF becomes more dominant (i.e., the value of explained variance increases) when the freshwater forcing is increased (from 1 to 6). From Fig. 3.9 one observes that for small freshwater forcing (panels a-b) most of the variability takes place near 15°N and at about 1000m depth. However, the maximum shifts to higher latitudes and deeper locations when the freshwater is increased (panels c) and closest to the transition (panel d) the maximum occurs at about 2000m depth at both 20°S and 20°N. In a word, once the

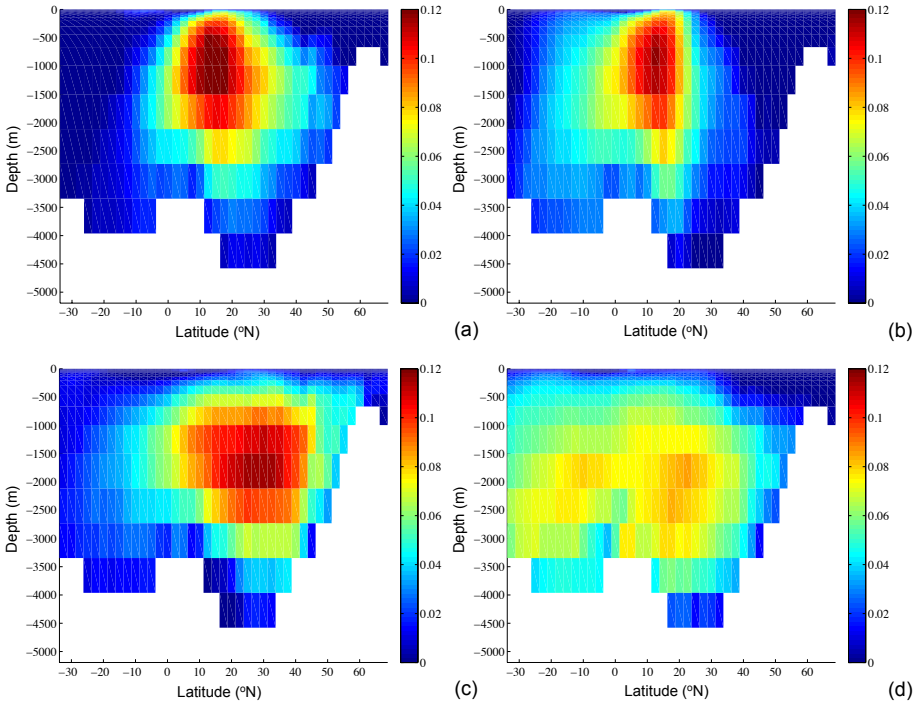

Figure 3.9: *(a) The first EOF of the MOC data of equilibrium simulation 1, explaining 26.3% of the variance. (b) Same as (a) but of equilibrium simulation 2, explaining 24.1% of the variance. (c) Same as (a) but of equilibrium simulation 4, explaining 37.1% of the variance. (d) Same as (a) but of equilibrium simulation 6, explaining 37.6% of the variance.*

transition is approached, one of the EOFs becomes most dominant in the variability. The network can be seen as a coarse-graining of the variability and by focussing only on the largest correlations, it is ideally suited to monitor the changes in spatial correlations of the system once the transition is approached.

Next, we study the transient behavior of the hosing simulation by reconstructing similar PCCNs. In Section 3.3, the kurtosis K_d of the degree distribution was introduced as an effective indicator to capture the changes in the topology of the degree field. For the complete Atlantic MOC field, the values of K_d for the hosing simulation (blue curve) and for the control simulation (green curve) are plotted in Fig. 3.10a. For the hosing simulation, there is indeed a strong increase of K_d to values far extending those for the control simulation significantly before the collapse time τ_c. For

comparison, the critical slowdown indicators variance (Fig. 3.10b) and lag-1 autocorrelation (Fig. 3.10c) based on the complete Atlantic MOC data (and using the same sliding window) do not show any early warning signal of the MOC transition before the collapse time τ_c.

To provide a measure of the performance of an indicator I, we introduce an evaluation scheme, which consists of determination of $max(I^{control})$, the detection time, the reliability of the indication, and the intensity of the indication, γ^I.

1) *Determination of* $max(I^{control})$: Here the maximum of the control is taken over the total time interval $[0, \tau_c]$. This choice for the control is based on the fact that the FAMOUS model simulation data indicate that the control solution is not yet in a statistically equilibrated stationary state. This is due to a slight climate drift in the model, which can be seen from the MOC data in Fig. 3.2a. The results of the hosing experiment hence depend on the initial state of the control simulation. In other words, one may find a larger $max(I^{control})$ after the first 1000 years of the control simulation by considering e.g. 1000 years more. However, if the hosing simulation would have been started accordingly at year 1000 of the control simulation, then the I signal would also be stronger, eventually giving similar results as now here. Hence, the first 1000 years of control simulation (with the origin being the starting point of the hosing simulation) are most adequate to represent the variability of the control simulation. For example, in Fig. 3.11, it is shown how $max(K_d^{control})$ over the interval $[0, \tau_{max}]$ depends on τ_{max} (the dashed black curve) for the first 1000 years. One can see that $max(K_d^{control})$ quickly saturates (before the year 200). Therefore, it is reasonable to take the maximum of the control over the time interval $[0, \tau_c]$.

2) *Detection time*: When a value of an indicator for the hosing simulation exceeds $max(I^{control})$, we flag an alarm of a collapse. For example, the maximum of K_d for the control simulation (green curve in Fig. 3.10a) is plotted as the blue dashed line in Fig. 3.10a. In this case, an early warning signal is detected at year 738, which is 136 years before the MOC collapse time $\tau_c = 874$ years.

3) *False Alarm*: We label a detection time which is smaller than $\tau_c - 300$ years as a false alarm. The reason we choose this time frame is that in the hosing simulation the system needs about 300 years to adapt to the changes in freshwater flux. This time span is visible in Fig. 3.2a as the time between the system passing the freshwater flux related to equilibrium point 6 and its actual collapse. Moreover, the 300 years is based on the horizon considered in IPCC-AR5 [Collins et al., 2013] for the evolution of the climate system (such as reflected in the Extended Concentration Pathway Emissions and Forcing scenarios, ECPs). Such a time period is also considered to be a political time horizon [Lenton et al., 2008] such that decisions taken within this period are able to affect the occurrence of a collapse. In addition, when the detection time is within $[\tau_c - 300, \tau_c]$, but the signal only lasts less than 5 years it is also considered as a false alarm.

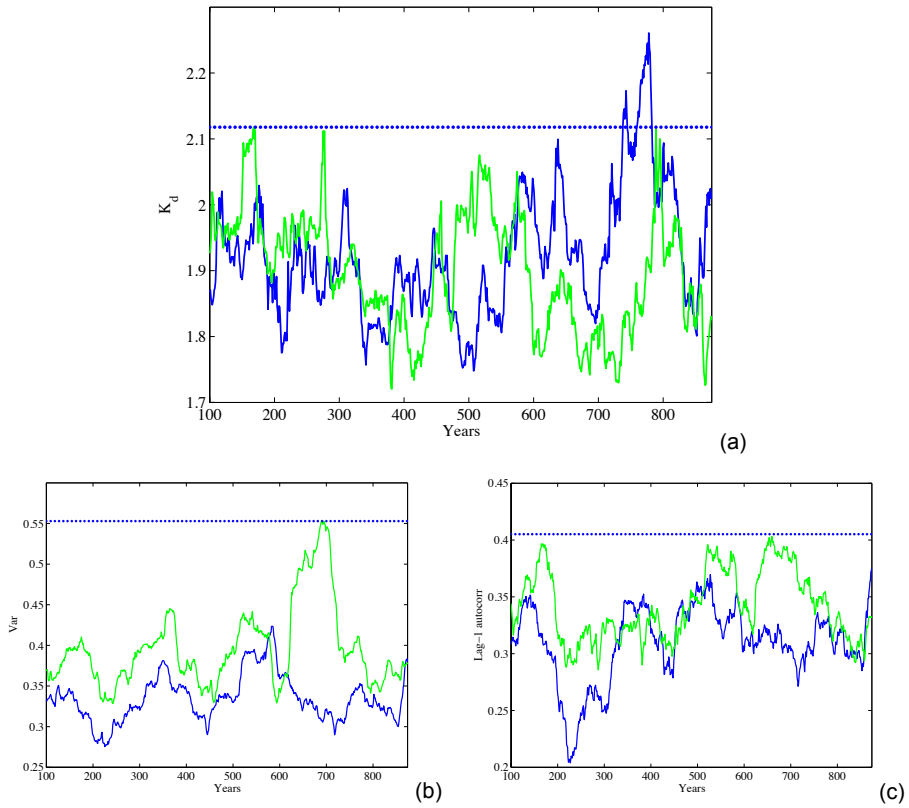

Figure 3.10: *For the complete Atlantic MOC field, (a) the kurtosis indicator K_d gives the early warning signal at 738 years and lasts for 44 years. (b) The traditional variance indicator Var gives no early warning signal before the collapse time $\tau_c = 874$ years. (c) The traditional lag-1 autocorrelation indicator Autocorr gives no early warning signal before the collapse time τ_c. Green solid curves are related to the control simulation and blue solid curves are related to the hosing simulation. The dashed blue horizontal lines indicate the corresponding maximum values of the control simulation taken over the total time interval $[0, \tau_c]$.*

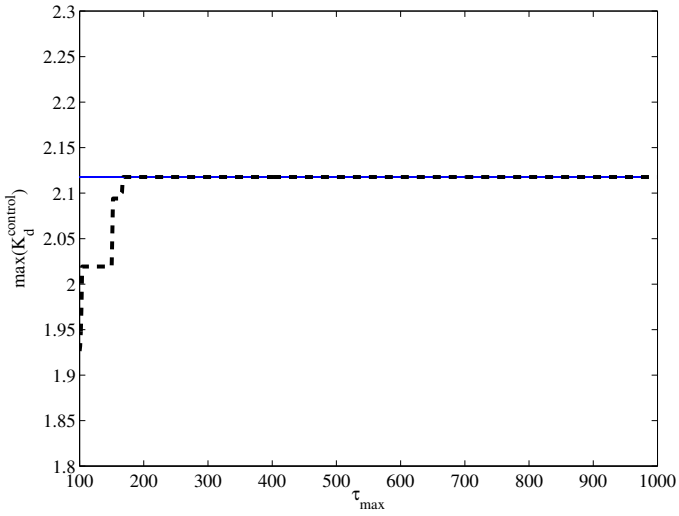

Figure 3.11: *Curve showing* $max(K_d^{control})$ *over the interval* $[0, \tau_{max}]$ *(dashed black curve) for the data of the control simulation in Fig. 3.10a; also the value* $max(K_d^{control})$ *over the interval* $[0, \tau_c]$ *is plotted (solid horizontal line).*

4) *Detection intensity* γ^I: The amplitude of the peak of the indicator is also important. Therefore, we additionally define another quality measure γ^I for indicator I as

$$\gamma^I = \frac{\max_P(I^{hosing})}{\max_{[0,\tau_c]}(I^{control})} - 1 \tag{3.12}$$

The larger the value of γ^I the better the quality of the indicator I; if $\gamma^I \leq 0$ no detection occurs. For example, based on the results in Fig. 3.10a the value of γ^{K_d} for the complete Atlantic MOC field is about 0.07 (see entry No. 1 in Table 3.3). Values of γ for both the variance (Fig. 3.10b) and the lag-1 autocorrelation (Fig. 3.10c) are smaller than zero.

The excellent performance of the kurtosis indicator K_d (with a detection time at 738 years, no false alarm and a positive value of γ^{K_d}) in Fig. 3.10a is shown in entry No.1 in Table 3.3.

Table 3.3: *The performance of the kurtosis indicator K_d based on complex networks reconstructed from sets of section data at different latitudes. In the sets of sections indicated by brackets, the first entry indicates the southern boundary, the second entry the northern boundary and the third entry is the latitudinal step.*

No.	Section	Detection Time (Year)	False Alarm	γ^{K_d}
1	(35°S, 70°N, 2.5°)	738	No	0.0675
2	26°N	384/567/868	Yes/Yes/No	0.1031/0.0451/0.0105
3	33°S	-	-	-0.1252
4	(35°S, 70°N, 5°)	739	No	0.0472
5	(20°N, 70°N, 5°)	-	-	0
6	(35°S, 20°N, 5°)	785	No	0.0559
7	(35°S, 35°N, 5°)	785	No	0.0773
8	(20°S, 35°N, 5°)	785	No	0.0584
9	Latitude set I	753	No	0.1248
10	Latitudes set II	740	No	0.0951
11	Latitude set III	-	-	-0.0810
12	Latitude set IV	-	-	-0.0454

I : 18°S, 13°S, 8°S, 11°N, 16°N, 21°N, 26°N and 31°N

II : 33°S, 18°S, 13°S, 11°N, 16°N, 21°N, 26°N and 31°N

III : 13°N, 16°N, 18°N, 21°N, 23°N, 26°N, 28°N and 31°N

IV : 33°S, 31°S, 28°S, 26°S, 23°S, 21°S, 18°S and 16°S

3.5 DETERMINE OPTIMAL OBSERVATION LOCATIONS

So far, we mainly used the complete Atlantic MOC field, but at the moment, MOC observations are only routinely made at 26°N through the RAPID-MOCHA program [Cunningham et al., 2007]. There are also initiatives to monitor the MOC at 35°S (SAMOC, see www.aoml.noaa.gov/phod/SAMOC_international) and at about 60°N (OSNAP, see www.o-snap.org). Motivated by the fact that current and near future available observations of the MOC will only be available along zonal sections in the Atlantic, we next reconstructed networks (and the indicator K_d) from limited section MOC data of the FAMOUS model results.

The performance of the kurtosis indicator K_d for different sections and combinations of sections is shown in Table 3.3. The indicator K_d provides two false alarms and one relatively late alarm for data at 26°N (entry No. 2 in Table 3.3), no alarm at all for data at 33°S (entry No. 3 in Table 3.3) and does not perform well for all other

Table 3.4: *The performance of the kurtosis indicator K_d based on complex networks reconstructed from different single zonal sections.*

Section	Detection Time (Year)	False Alarm	γ^{K_d}
33°S	-	-	-0.1252
28°S	-	-	-0.1540
23°S	-	-	-0.0090
18°S	-	-	-0.0456
13°S	-	-	-0.1774
8°S	-	-	-0.0595
3°S	-	-	-0.1937
1°N	-	-	0
6°N	-	-	-0.0840
11°N	-	-	-0.0202
16°N	872	No	0.1792
21°N	396/866	Yes/No	0.0045/0.0420
26°N	384/567/868	Yes/Yes/No	0.1031/0.0451/0.0105
31°N	384	Yes	0.0161
36°N	382	Yes	0.0909
41°N	586[(a)]	Yes	0.0057
46°N	-	-	-0.1463
51°N	-	-	-0.0260

(a) : Signal only lasts for 2 years.

single section data as shown in Table 3.4 (55°N is excluded as the MOC amplitude is very small). When the varriance and the lag-1 autocorrelation of time series averaged over a single section are considered, the variance indicator (Table 3.5) does not give any warning for all single sections, while the lag-1 autocorrelation indicator (Table 3.6) performs best at 21°N although it still gives a false alarm.

To determine the optimal observation locations of the MOC using K_d, we systematically deleted sections from the complete Atlantic MOC field and evaluated the performance of the indicator K_d for the remaining sections. Entry No. 4 in Table 3.3 shows that the indicator K_d still works well for the Atlantic MOC field with halved horizontal

Table 3.5: *The performance of the variance indicator Var at different single zonal sections*

Section	Detection Time (Year)	False Alarm	γ^{Var}
33°S	-	-	-0.0694
28°S	-	-	-0.0697
23°S	-	-	-0.0747
18°S	-	-	-0.0868
13°S	-	-	-0.0500
8°S	-	-	-0.0515
3°S	-	-	-0.0326
1°N	-	-	-0.0402
6°N	-	-	-0.1279
11°N	-	-	-0.1505
16°N	-	-	-0.2153
21°N	-	-	-0.3104
26°N	-	-	-0.3773
31°N	-	-	-0.3389
36°N	-	-	-0.3116
41°N	-	-	-0.3482
46°N	-	-	-0.4464
51°N	-	-	-0.4735

resolution (21(depth) × 21(latitude)= 441 nodes), as well as for the sets of sections including midlatitudes both in the Northern and Southern Hemisphere (entries No. 6-8 in Table 3.3). However, detection fails for the set of sections located only in the Northern Hemisphere at mid- and high latitudes (entry No. 5 in Table 3.3).

The most reduced latitude set for which the performance of the indicator K_d is still comparable to the case of the complete Atlantic MOC field (Fig. 3.10a and entry No. 1 in Table 3.3) is latitude set I, which consists of 18°S, 13°S, 8°S, 11°N, 16°N, 21°N, 26°N and 31°N (blue curve in Fig. 3.12 and entry No. 9 in Table 3.3). This set consist of 21(depth)×8(latitude)= 168 grid points and hence the number of nodes is considerably reduced (by 81%) in comparison to the complete Atlantic MOC field. Further analysis (Table 3.7) indicates that the data at sections 18°S and 31°N are essential for a good detection of the MOC collapse.

In order to examine the importance of monitoring the MOC at 35°S (SAMOC), we substituted 8°S in the latitude set I by 33°S and formed the latitude set II (green curve in Fig. 3.12 and entry No. 10 in Table 3.3). The results in entries No. 9 and 10 in Table

Table 3.6: *The performance of the Lag-1 Autocorrelation indicator AC at different single zonal sections*

Section	Detection Time (Year)	False Alarm	γ^{AC}
33°S	-	-	-0.1470
28°S	-	-	-0.0265
23°S	497	Yes	0.0593
18°S	-	-	-0.0987
13°S	870	No	0.0416
8°S	-	-	-0.0582
3°S	-	-	-0.0904
1°N	-	-	-0.0993
11°N	-	-	-0.1168
16°N	-	-	-0.0512
21°N	506	Yes	0.1769
26°N	-	-	-0.0471
31°N	-	-	-0.0654
36°N	-	-	-0.0820
41°N	-	-	-0.0455
46°N	-	-	-0.1420
51°N	-	-	-0.1107

3.3 indicate that including the MOC data at 33°S (near the SAMOC section) would advance the detection time of a future collapse of the MOC compared to including a section at 8°S, but the detection intensity γ^{K_d} of the kurtosis indicator K_d would be slightly decreased.

The physical reason for the optimal observation regions is the following. In ocean-climate models, the MOC collapse is due to a robust feedback involving the transport of salinity by the ocean circulation, the salt-advection feedback [Stommel, 1961; Walin, 1985]. The subtropics are strong evaporation regions and hence the largest salinity gradients, central in the salt-advection feedback, are located in these regions. Consequently, it is expected that here the strongest response due to the salt-advection feedback appears and hence the strongest spatial correlations in the MOC field. Support for this comes from the structure of the dominant EOFs of the equilibrium solu-

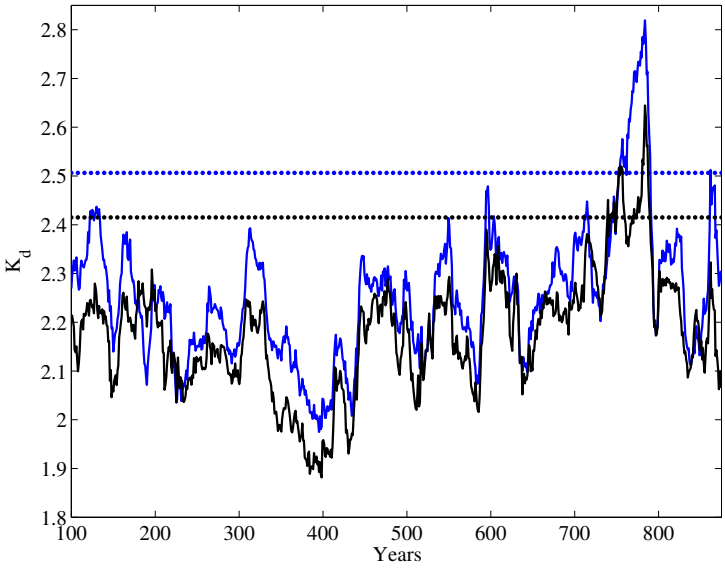

Figure 3.12: *The kurtosis indicator K_d for section data reconstructed from 21 depth levels and 8 latitudes. (a) Data from 31°N, 26°N, 21°N, 16°N, 11°N, 8°S, 13°S and 18°S (blue solid curve), gives the early warning signal at 753 years and lasts for 38 years. (b) Data from 31°N, 26°N, 21°N, 16°N, 11°N, 13°S, 18°S and 33°S (black solid curve), gives the early warning signal at 740 years and lasts for 49 years. The dotted blue horizontal line indicates the maximum K_d value of the control simulation of section data (a) taken over the total time interval $[0, \tau_c]$, and the dotted black horizontal line indicates the corresponding maximum K_d value of section data (b) taken over the total time interval $[0, \tau_c]$.*

tions where the largest amplitude is also located in these midlatitude regions (see Fig. 3.9).

3.6 SUMMARY AND DISCUSSIONS

The strength of the Atlantic MOC is currently actively monitored [Cunningham et al., 2007] with the motivation that the MOC may rapidly (within a few decades) change in strength. Up to now, there is about 10 years of data on the MOC from the RAPID-MOCHA array (see Fig. 1.7), and although this array will likely be operational up to the year 2020, the temporal extend of the time series proceeds only slowly. Thus, the time series of the MOC strength derived from the RAPID-MOCHA program are cer-

Table 3.7: *Sensitivity test of the kurtosis indicator K_d by excluding, in each case, one single section from the set I of optimal sections given in Table 3.3.*

Section	Detection Time (Year)	False Alarm	γ^{K_d}
7 latitudes (I *without* 18°S)	-	-	-0.0303
7 latitudes (I *without* 13°S)	768	No	0.0233
7 latitudes (I *without* 8°S)	773	No	0.0047
7 latitudes (I *without* 11°N)	$596^{(a)}/712^{(b)}/772^{(c)}$	Yes/Yes/Yes	0.0175/0.0096/0.0163
7 latitudes (I *without* 16°N)	443	Yes	0.1303
7 latitudes (I *without* 21°N)	862	No	0.0977
7 latitudes (I *without* 26°N)	859	No	0.0317
7 latitudes (I *without* 31°N)	-	-	-0.0033

(a) : Signal only lasts for 2 years.

(b) : Signal only lasts for 1 years.

(c) : Signal only lasts for 3 years.

tainly too short to be able to apply early warning indicators based on the slow down and increased variance of the MOC [Lenton, 2011; Thompson and Sieber, 2011].

Using techniques of complex network theory, we have provided a novel indicator based on spatial correlations which can give an early warning signal for a collapse of the MOC. We first studies the performance of the indicator by looking at solutions of an idealized ocean model of the MOC for which the critical conditions for collapse could be computed in detail. We showed that the kurtosis value of the normalized degree distribution K_d increases steeply when the tipping point L_1 is approached. The explanation for this increase is based on the increased dominance of the first EOF in the variance of the solution in a large part of the domain. When applied to the data from the FAMOUS model [Hawkins et al., 2011], our results show that when the appropriate midlatitude North and South Atlantic MOC data are available, the kurtosis indicator K_d provides a strong anomalous signal at least 100 years before the transition.

Due to the insufficient length of the observational record, the indicator K_d is not yet applicable to observational data and hence cannot be used to determine whether the recent downward trend in the observed MOC strength at 26°N [Smeed et al., 2013] is the start of a collapse (see Fig. 1.7). Such MOC behavior may just be related to natural variability such as that associated with the Atlantic Multidecadal Oscillation [Kerr, 2000; Knight et al., 2005]. However, the strong element of an indicator such as K_d, in contrast to indicators based on a single-point time series, is that it is based on spatial correlations. Our results indicate that an increase in spatial resolution of

the MOC observations (i.e., at more sections) can improve early detection using this indicator, because the spatial coherence arising near the transition is better captured. This is another reason that such observations should be given high priority in climate research.

Although at the moment a collapse of the MOC is considered a high-impact but low-probability event [Collins et al., 2013], modesty is required regarding our confidence in this statement. The processes controlling the behavior of the MOC, such as the downwelling in the northern North Atlantic boundary currents, are not well represented in many of the climate models on which this statement is based. In state-of-the-art GCMs, such as those used in the IPCC AR5, MOC collapses have not been found yet, but it is fair to say that these models have not been extensively tested for this behavior [Collins et al., 2013; Huisman et al., 2010].

In a potential application to determine whether transitions in the MOC have been involved in the Dansgaard-Oeschger oscillations, well synchronized records of ocean bottom temperatures are needed.

4

ARE NORTH ATLANTIC MULTIDECADAL SST ANOMALIES WESTWARD PROPAGATING?

The westward propagation of sea surface temperature (SST) anomalies is one of the main characteristics of one of the theories of the Atlantic Mutidecadel Oscillation. In this chapter, we use techniques from complex network modeling to investigate the existence of the westward propagation in the North Atlantic SST observations. We reconstruct Climate Networks (CNs) by using a linear Pearson correlation measure (resulting in Pearson Correlation Climate Networks (PCCNs)) and a (nonlinear) mutual information measure (resulting in Mutual Information Climate Networks (MICNs)) of spatial correlations betweenSST variations. Analysis of the topological properties of both types of CNs shows that the MICNs are better in capturing the main features of propagating patterns from the noisy SST data than PCCNs, and that westward propagation of multidecadal SST anomalies indeed seems to occur in the North Atlantic.

This chapter has been published as:
Q. Y. Feng, and H. A. Dijkstra. Are North Atlantic Multidecadal SST Anomalies Westward Propagating? *Geophysical Research Letters*, 2014, 41(2): 541-546. DOI: 10.1002/2013GL058687.

4.1 INTRODUCTION

The Atlantic Multidecadal Oscillation (AMO) is characterized by low frequency variability in sea surface temperature (SST) occurring in the North Atlantic Ocean [Delworth and Mann, 2000b; Schlesinger and Ramankutty, 1994b]. The AMO is thought to have significant effects on summer temperatures and precipitation variations in western Europe and North America [Enfield et al., 2001b; Sutton and Hodson, 2005b], and possibly hurricane development in tropical Atlantic regions [Andronova and Schlesinger, 2000]. There is a debate and still unsolved question on whether the North Atlantic SST anomalies in the 20th century is an expression of an internal climate mode or an imprint of external forcing [Ting et al., 2009]. Thus a mechanistic understanding of the AMO is important and a theory should explain the processes responsible for the multidecadal time scale and the spatial patterns of the SST anomalies [Dijkstra et al., 2008].

In one of the theories of the AMO [Te Raa and Dijkstra, 2002], the variability arises due to internal ocean dynamics through an oscillatory instability of the background Meridional Overturning Circulation (MOC). A sketch of this so-called thermal Rossby mode mechanism is provided in Fig. 4.1. A warm anomaly in the north-central part of the basin causes a northward meridional perturbation temperature gradient, which induces – via the thermal wind balance – an anti-clockwise or westward surface zonal flow (Fig. 4.1a). Because of a southward background temperature gradient, the anomalous anticyclonic circulation around the warm anomaly causes southward (northward) advection of cold (warm) water to the east (west) of the anomaly, resulting in westward phase propagation of the warm anomaly. Due to this westward propagation, the zonal perturbation temperature gradient becomes eastward, inducing an anti-clockwise or southward surface meridional flow (Fig. 4.1b). The resulting upwelling (downwelling) perturbations along the northern (southern) boundary cause a southward meridional perturbation temperature gradient, inducing an eastward zonal surface flow, and the second half of the oscillation starts.

In this mechanism, the basin-crossing time of the SST anomalies sets the time scale of variability and, based on the observations, it was argued to be 20-30 years [Frankcombe et al., 2010]. Evidence of westward propagation was found in subsurface temperature observations [Frankcombe et al., 2008], but the length of the time series (XBT data since 1960) used was relatively short. Indications for westward propagation in sea-level records were found in Frankcombe and Dijkstra [Frankcombe and Dijkstra, 2009] and more recently in Vianna and Menezes [Vianna and Menezes, 2013], who show that after 1960, clear westward propagation in sea level occurs in the North Atlantic.

SST is certainly a complex field controlled by a diversity of (nonlinear) processes such as advection in an eddying ocean and noisy surface heat fluxes. However, it should be possible to extract westward propagating SST anomalies in the Hadley

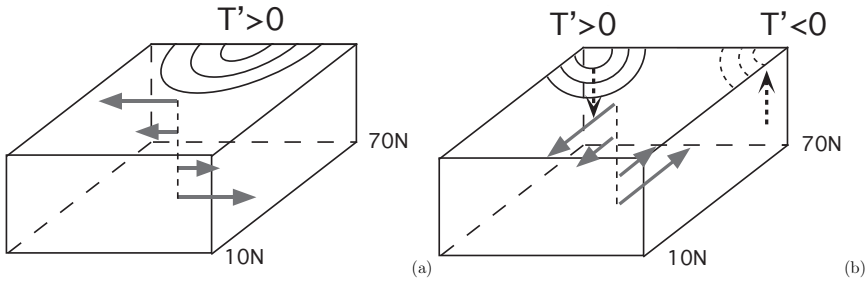

Figure 4.1: *Schematic diagram of the oscillation mechanism associated with the thermal Rossby mode caused by the westward propagation of the temperature anomalies T'. The phase difference between (a) and (b) is about a quarter period. See text and [Te Raa and Dijkstra, 2002] for a further explanation.*

Centre Sea Ice and Sea Surface Temperature (HadISST) dataset, if the thermal Rossby mechanism is dominant on the multidecadal time scale (which appears to follow from sea level anomaly analysis [Vianna and Menezes, 2013]).

In this chapter, we use the Climate Network (CN) [Gozolchiani et al., 2011; Tsonis and Swanson, 2006] to investigate the existence of the westward propagation of observed North Atlantic SST anomalies. Because temporal changes in spatial correlations between climate variables do lead to temporal changes in the topological properties of the network [Donges et al., 2009b], this methodology provides an innovative way to study propagating patterns of climate variability.

4.2 MODEL AND DATA

4.2.1 *Idealized ocean model*

We first use data from an idealized three-dimensional single-hemispheric sector ocean model from which the mechanism of the thermal Rossby mode was originally deduced [Te Raa and Dijkstra, 2002].

In this model, the ocean flow is forced only by a prescribed heat flux deduced from a steady state obtained under a fixed equator-to-pole temperature gradient. We consider ocean flows in a model domain on the sphere bounded by the longitudes $\phi_w = -74°$E and $\phi_e = -10°$E and by the latitudes $\theta_s = 10°$N and $\theta_n = 74°$N;

the ocean basin has a constant depth H. The flows in this domain are forced by a restoring heat flux Q_{rest} (in Wm^{-2}) given by

$$Q_{rest} = -\lambda_T (T^* - T_S), \tag{4.1}$$

where λ_T (in $\mathrm{Wm}^{-2}\mathrm{K}^{-1}$) is a constant surface heat exchange coefficient. The heat flux Q_{rest} is proportional to the temperature difference between the ocean temperature T^* taken at the surface and a prescribed atmospheric temperature T_S, chosen as

$$T_S(\phi,\theta) = T_0 + \frac{\Delta T}{2}\cos\left(\pi\frac{\theta-\theta_s}{\theta_n-\theta_s}\right), \tag{4.2}$$

where $T_0 = 15°\mathrm{C}$ is a reference temperature and ΔT is the temperature difference between the southern and northern latitude of the domain. The thermal forcing is distributed as a body forcing over the first (upper) layer of the ocean having a depth H_m.

Temperature differences in the ocean cause density differences according to

$$\rho = \rho_0(1-\alpha_T(T^*-T_0)), \tag{4.3}$$

where α_T is the volumetric expansion coefficient and ρ_0 is a reference density. Inertia is neglected in the momentum equations because of the small Rossby number, we use the Boussinesq and hydrostatic approximations and represent horizontal and vertical mixing of momentum and heat by constant eddy coefficients. With r_0 and Ω being the radius and angular velocity of the Earth, the governing equations for the zonal, meridional and vertical velocity u, v and w, the dynamic pressure p (the hydrostatic part has been subtracted) and the temperature $T = T^* - T_0$ become

$$-2\Omega\, v\sin\theta + \frac{1}{\rho_0 r_0\cos\theta}\frac{\partial p}{\partial\phi} - A_H L_u(u,v) - A_V\frac{\partial^2 u}{\partial z^2} = 0, \tag{4.4a}$$

$$2\Omega\, u\sin\theta + \frac{1}{\rho_0 r_0}\frac{\partial p}{\partial\theta} - A_H L_v(u,v) - A_V\frac{\partial^2 v}{\partial z^2} = 0, \tag{4.4b}$$

$$\frac{\partial p}{\partial z} - \rho_0 g\alpha_T T = 0, \tag{4.4c}$$

$$\frac{1}{r_0\cos\theta}\left(\frac{\partial u}{\partial\phi} + \frac{\partial(v\cos\theta)}{\partial\theta}\right) + \frac{\partial w}{\partial z} = 0, \tag{4.4d}$$

$$\frac{DT}{dt} - K_H\nabla_H^2 T - K_V\frac{\partial^2 T}{\partial z^2} - \frac{(T_S - T^*)}{\tau_T}\mathscr{H}\left(\frac{z}{H_m}+1\right) = 0, \tag{4.4e}$$

where $\mathscr{H}$ is a continuous approximation of the Heaviside function, g is the gravitational acceleration and $\tau_T = \rho_0 C_p H_m/\lambda_T$ is the surface adjustment time scale of heat (C_p is the constant heat capacity). In these equations, A_H and A_V are the horizontal and vertical momentum (eddy) viscosity and K_H and K_V the horizontal

Table 4.1: *Standard values of parameters used in the idealized ocean model.*

2Ω	=	1.4×10^{-4}	$[s^{-1}]$	r_0	=	6.4×10^{6}	[m]
H	=	4.0×10^{3}	[m]	τ_T	=	3.0×10^{1}	[days]
α_T	=	1.0×10^{-4}	$[K^{-1}]$	g	=	9.8	$[ms^{-2}]$
A_H	=	1.6×10^{5}	$[m^2s^{-1}]$	T_0	=	15.0	[°C]
ρ_0	=	1.0×10^{3}	$[kg\ m^{-3}]$	A_V	=	1.0×10^{-3}	$[m^2s^{-1}]$
K_H	=	1.0×10^{3}	$[m^2s^{-1}]$	K_V	=	1.0×10^{-4}	$[m^2s^{-1}]$
C_p	=	4.2×10^{3}	$[J(kgK)^{-1}]$	ΔT	=	20.0	[K]

and vertical (eddy) diffusivity of heat, respectively. In addition, the operators in the equations above are defined as

$$\frac{D}{dt} = \frac{\partial}{\partial t} + \frac{u}{r_0\cos\theta}\frac{\partial}{\partial\phi} + \frac{v}{r_0}\frac{\partial}{\partial\theta} + w\frac{\partial}{\partial z}, \tag{4.5a}$$

$$\nabla_H^2 = \frac{1}{r_0^2\cos\theta}\left[\frac{\partial}{\partial\phi}\left(\frac{1}{\cos\theta}\frac{\partial}{\partial\phi}\right) + \frac{\partial}{\partial\theta}\left(\cos\theta\frac{\partial}{\partial\theta}\right)\right], \tag{4.5b}$$

$$L_u(u,v) = \nabla_H^2 u + \frac{u\cos2\theta}{r_0^2\cos^2\theta} - \frac{2\sin\theta}{r_0^2\cos^2\theta}\frac{\partial v}{\partial\phi}, \tag{4.5c}$$

$$L_v(u,v) = \nabla_H^2 v + \frac{v\cos2\theta}{r_0^2\cos^2\theta} + \frac{2\sin\theta}{r_0^2\cos^2\theta}\frac{\partial u}{\partial\phi}. \tag{4.5d}$$

Slip conditions and zero heat flux are assumed at the bottom boundary, while at all lateral boundaries no-slip and zero heat flux conditions are applied. As the forcing is represented as a body force over the first layer, slip and zero heat flux conditions apply at the ocean surface. Hence, the boundary conditions are

$$z = -H, 0: \qquad \frac{\partial u}{\partial z} = \frac{\partial v}{\partial z} = w = \frac{\partial T}{\partial z} = 0, \tag{4.6a}$$

$$\phi = \phi_w, \phi_e: \qquad u = v = w = \frac{\partial T}{\partial\phi} = 0, \tag{4.6b}$$

$$\theta = \theta_s, \theta_n: \qquad u = v = w = \frac{\partial T}{\partial\theta} = 0. \tag{4.6c}$$

The parameters for the standard case are the same as in typical large-scale low-resolution ocean components of (4° horizontally) coupled ocean-atmosphere general circulation model (GCM) and their values are listed in Table 4.1.

The governing equations (4.4) and boundary conditions (4.6) are discretized on an Arakawa B-grid using central spatial differences. In the results in this chapter, a horizontal resolution of 4° is used. An equidistant grid with 16 levels is applied in

the vertical so that the first layer thickness $H_m = 250$ m. The model is first run under restoring conditions to a steady state equilibrium. From this equilibrium, the heat flux Q_{pres} is diagnosed. Subsequent simulations are done with a heat flux

$$Q_H = Q_{pres} + Q_{noise} \tag{4.7}$$

where Q_{noise} is the stochastic heat flux is taken as

$$Q_{noise}(\phi, \theta, t) = \eta(t) cos\theta \tag{4.8}$$

where η is a zero mean normally distributed random variable with a standard deviation σ.

We performed a 500-year (with a time step of 0.1 years) simulation with this model. The SST output of this model is considered on the domain [-66°E, -10°E] × [10°N, 74°N] with a 4° resolution. This provides a time series of 5000 SST anomaly fields (with respect to the time mean) on a 14×16 grid having $N_M = 224$ nodes.

A Hovmöller diagram of meridionally averaged (30-60°N) SST anomalies from the idealized model data (Fig. 4.2a) clearly shows the westward propagation associated with the thermal Rossby mode [Dijkstra et al., 2008]. The oscillation period in the model is about 40 years, which is between the 20-30 and 50-70 dominant periods in the observations [Frankcombe et al., 2010]. Note that the warm phase of the oscillation is slightly longer than the cold phase, reflecting the nonlinear effects in the variability.

4.2.2 *Observational data*

For the SST observations of the North Atlantic, we use the HadISST [Rayner et al., 2003b] dataset containing monthly SST data from Jan 1870 to Oct 2012 (1714 months) and covers the whole world with a resolution of 1°. To minimize the effects of the continental shape, the geographical zone we choose here is [-51°E, -9°E] × [9°N, 75°N]. Consistent with the resolution of the idealized model (which is 4°) we also lower the resolution of the observations from 1° to 3° to facilitate the comparison of results. By removing the mean of each time series, we obtain monthly mean SST anomalies on a 14×22 spatial grid for nearly 142 years, having $N_O = 308$ nodes.

When a running mean of 8-year is applied to the HadISST data, a similar Hovmöller diagram (Fig. 4.2b) does not clearly indicate westward propagation, in agreement with earlier studies [Delworth and Mann, 2000b; Tourre et al., 1999].

As part of the SST response is determined by the surface heat flux, one can do an attempt to remove this contribution. For example, using the surface heat flux field from the ORA-S3 reanalysis data to remove the SST contribution of the surface heat flux forcing from the HadISST data. Due to the availability of the ORA-S3 reanalysis data of the net surface heat flux, we choose the period of Jan 1959 to Dec 2009 (612

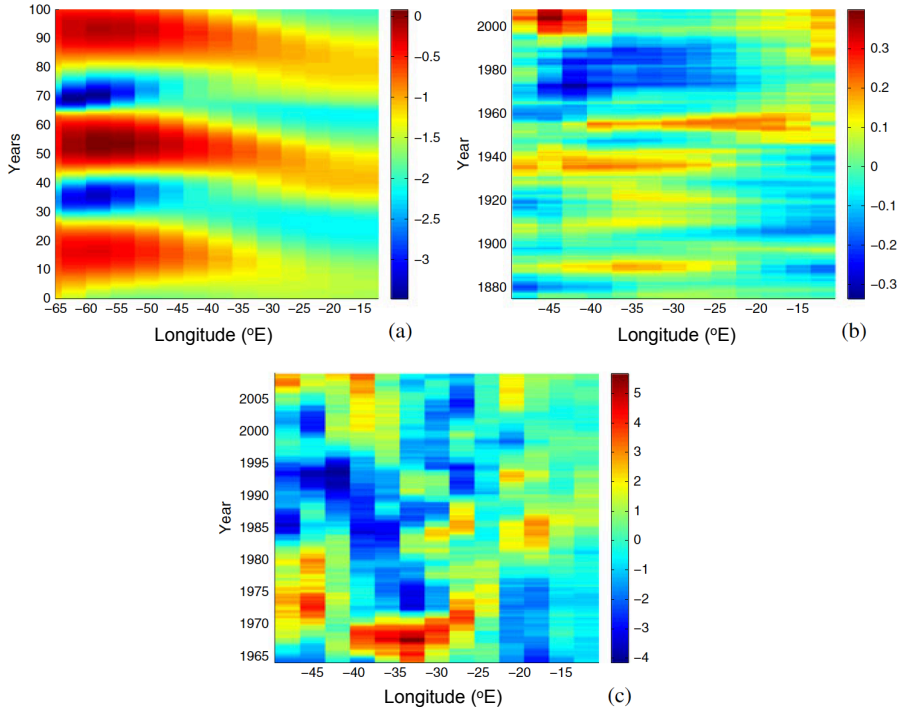

Figure 4.2: *Hovmöller diagram of the 30-60°N averaged North Atlantic SST anomalies from (a) the idealized ocean model simulations (b) 8-year running mean HadISST dataset (1870-2012) (c) the same as (b) but first the surface heat flux contribution (from the ORA-S3 data set, see http://apdrc.soest.hawaii.edu/) to SST is subtracted from HadISST dataset (only over the period 1959-2009).*

months) as an example (Fig. 4.3a). To quantify the SST contribution of surface heat flux forcing we assume that there is linear relationship (with correlation parameter α) between net heat flux anomalies (Q_h) and SST anomalies (T) at a similar latitude. For example, Fig. 4.3b shows the linear regression between these two quantities at 60°N giving $\alpha = 29.25$ Wm^{-2} K^{-1}. In this way, we can subtract the approximate surface heat flux forcing contribution from the HadISST dataset, by using $T^c = T^o - Q_h/\alpha$, where the subscripts c and o refer to corrected and original data, respectively. However, The result (Fig. 4.2c) still does not show a clear westward propagation. In addition, this correction cannot be performed over the whole HadISST data set, and it may also remove components of the thermal Rossby wave as the surface heat flux also depends on SST.

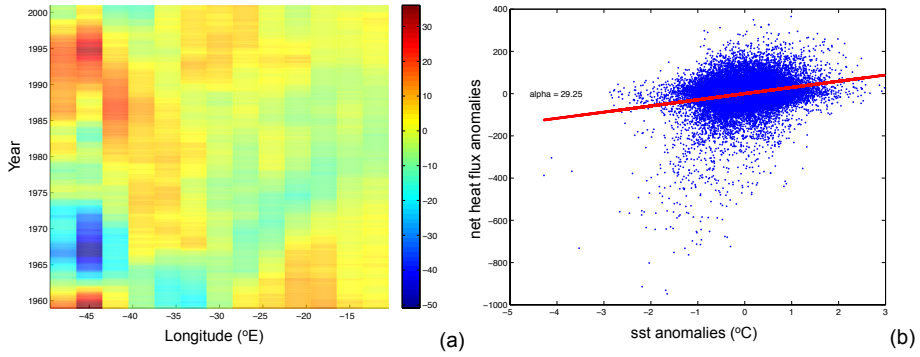

Figure 4.3: *(a) Hovmöller diagram of the 30-60°N averaged North Atlantic net heat flux anomalies from 8-year running mean reanalysis ORA-S3 dataset (1959-2009). (b) Linear regression between net heat flux anomalies and SST anomalies at 60°N*

To remove the influence of greenhouse gas-induced global warming, it seems appropriate to linear detrend the SST anomalies. However, if the global warming signal is substantially nonlinear in time (i.e. not just a smooth linear increase), or the current warming is partially due to the AMO, variations in detrended SST anomalies will be not consistent with the AMO phenomenon. Hence, for this study, we only implement a one-year running mean filter to smooth out short-term fluctuations.

4.3 RESULTS

4.3.1 *MICN versus PCCN*

Either a fixed threshold in correlation or a threshold in a fixed link density $\rho = 2E/(N(N-1))$ can be used to build unweighted and undirected links among nodes in a CN; here E is the total number of links and N the total number of nodes [Donges et al., 2009b]. E is negatively correlated with τ, which means that ρ will decrease when a higher value of τ is chosen, since the total number of nodes N is fixed. The minimum τ for the SST time series from the idealized model that gives a statistical significance above the 95% level is 0.3; this corresponds to a maximum value of $\rho = 0.99$. The minimum τ and maximum ρ for the observations are 0.12 and 0.62, respectively. When comparing Pearson Correlation Climate Network (PCCN) and Mutual Information Climate Network (MICN) reconstructed from the the data, it is better to constrain ρ than to fix τ [Donges et al., 2009b]. For example, if we fix τ at 0.9 for reconstructing the MICN of the idealized model data as in Fig. 4.4a, and $\tau = 0.5$ for the PCCN as in Fig. 4.4b, the similarity of degree fields between the MICN and PCCN

is lost, unlike the ones determined a fixed link density in the Fig. 4.5a and c. Therefore in the results below, we fix ρ at 0.2 for every CN, which guarantees significant correlations up to the 95% level in defining the links among the nodes in a CN.

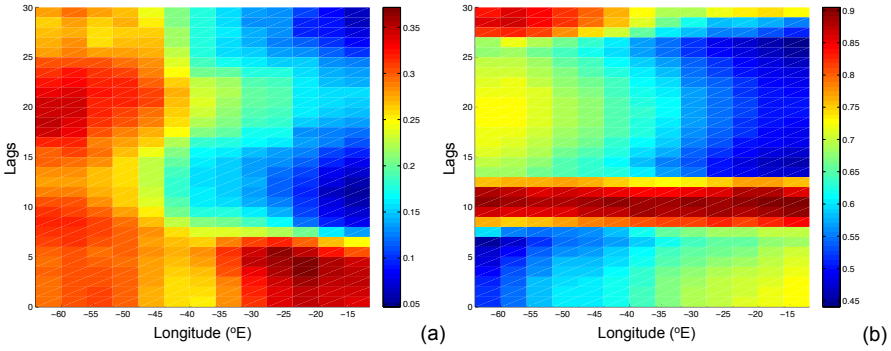

Figure 4.4: *Hovmöller diagram of 30-60°N averaged relative degree field of of the idealized model data, (a) the network reconstructed by using Mutual Information under a fixed threshold $\tau = 0.9$; (b) the network reconstructed by using Pearson Correlation under a fixed threshold $\tau = 0.5$*

For the MICN, the Hovmöller diagram of the relative degree field (degree divided by the maximum degree of this MICN $N_M - 1 = 223$), averaged over latitudes 30-60°N, for the idealized model data is plotted in Fig. 4.5a. The largest lag (Δt in e.q. 2.6) used in the reconstruction of the MICN is 30 years, so $\Delta t \in [0, 30]$. For small lags (0-10 years), the nodes with relatively high degree emerge from the eastern part and gradually high degree nodes are found more westwards. After approximately 15 years, the nodes with maximal degree appear at the western boundary of the domain. For the next 15 years (lags 15-30 years) there are only low degree nodes in the eastern part, while the degrees of the nodes in the western part remain high. This is consistent with Fig. 4.2a, where high spatial correlations are found for about 15 years in the west during the oscillation. Similar propagating features can also be found in the Hovmöller diagram of the relative degree field of the MICN reconstructed from the HadISST data (with $N_O - 1 = 307$), as seen in Fig. 4.5b. There is again a westward propagation of high degree over the lags 0-10 and the maximum occurs around year 15 near 40°W. For the following 15 years, relatively high degree nodes only appear in the western part in contrast to the lower degree nodes in the eastern part.

A nonlinear measure of correlation, here the mutual information, appears crucial to identify the westward propagation behavior in the observations. For the PCCN of the

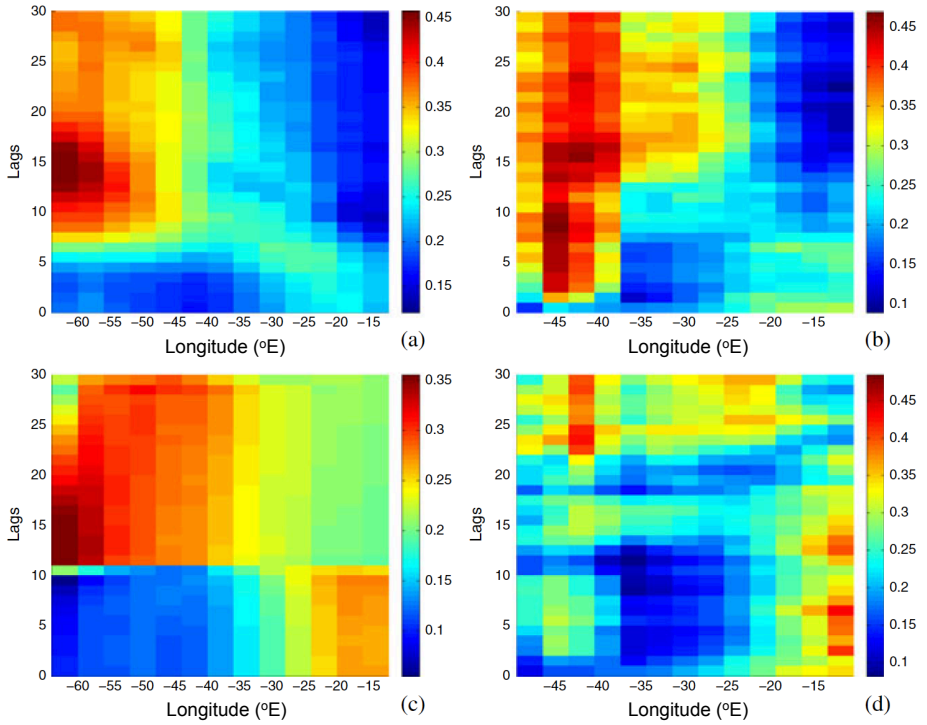

Figure 4.5: *Hovmöller diagram of the 30-60°N averaged relative degree fields of (a) the idealized model data, (b) the observations, (c) the idealized model data, and (d) the observations. The networks of (a) and (b) are reconstructed by using Mutual Information under a link density of 0.2. The networks of (c) and (d) are reconstructed by using Pearson Correlation under a link density of 0.2.*

idealized model data, the Hovmöller diagram of the degree field is plotted in Fig. 4.5c. The relative degree field (Fig. 4.5c) shows the same features as in the MICN (compare with Fig. 4.5a), but the position of the high degree nodes shifts much more abruptly to the west at year 10. The relative degree field of the PCCN reconstructed from the observations (Fig. 4.5d) does not show any westward propagation tendencies. In fact, the patterns of degree do not correspond neither to the one from the PCCN of the idealized model data (Fig. 4.5c), nor to the one from the MICN of the observations (Fig. 4.5b). Apparently, the PCCN analysis fails to distinguish the main features of the westward propagation pattern in the noisy SST signal from the observations.

4.3.2 *Robustness tests*

In the idealized model simulations, the stochastic heat flux Q_{noise} in equation (4.8) is prescribed as 10% temporally white additive noise to the heat flux (with a spatially coherent pattern). The reason we chose 10% as the noise level is that we found the time scale of the westward propagation of SST anomalies pattern increases to 40 years instead of 20-30 years variability without noise. When we increase the amount of noise, for example, to 20% (Fig. 4.6a) and 30% (Fig. 4.6b), the time scales of the westward propagating pattern increases to 60-80 years.

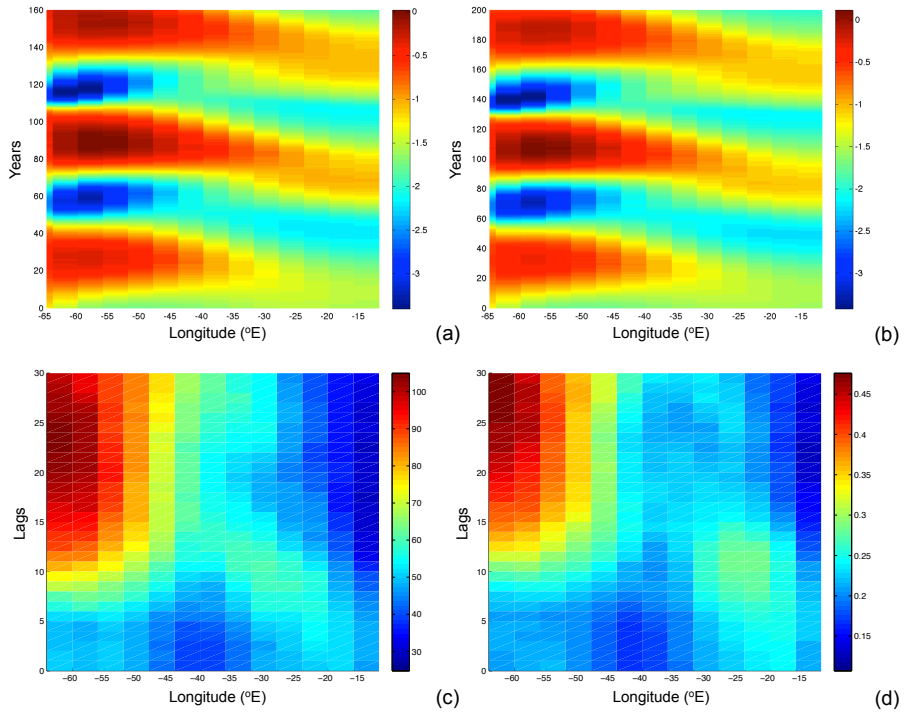

Figure 4.6: *Hovmöller diagram of 30-60°N averaged SST anomalies fields from the idealized model data with (a) 20% noise and (b) 30% noise. Hovmöller diagram of 30-60N averaged relative degree fields for the MICN reconstructed from the idealized model data with (c) 20% noise and (d) 30% noise.*

To investigate the sensitivity of the network results to the levels of the noise, we also reconstructed MICNs for additional sets of idealized model data with different amounts of noise. Fig. 4.6c is the degree field in the case of 20% noise and Fig. 4.6d

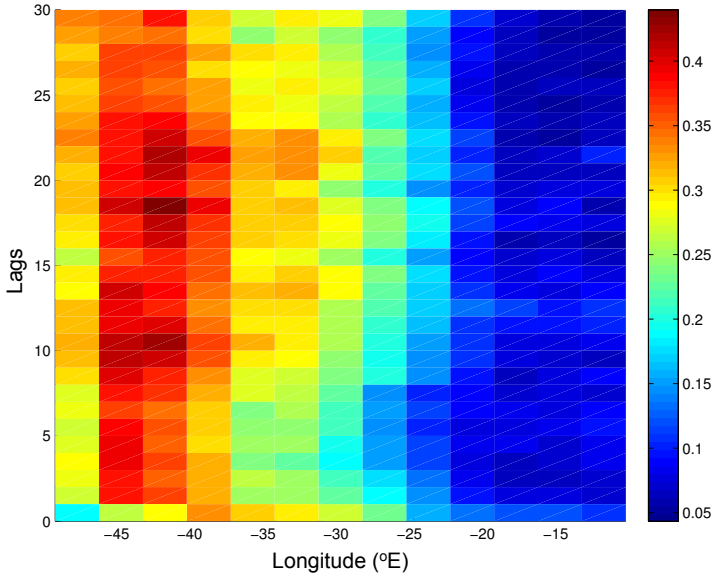

Figure 4.7: *Hovmöller diagram of 30-60°N averaged of the degree field from observations using linear detrending. The network is reconstructed by using Mutual Information under a fixed link density of 0.2.*

is the one with 30% noise. Comparing the three different degree fields (including the results with 10% noise as given in Fig. 4.5a), one can see that the time that high degree nodes appear in the west increases with the noise amplitude. Overall, however, the patterns of the degree fields are fairly robust to the amount of noise.

To investigate whether linear detrending affects the detection of westward propagation, we also reconstructed MICNs from linearly detrended data. The Hovmöller diagram of the 30-60°N averaged degree fields from the linearly detrended HadISST dataset are shown in Fig. 4.7. When comparing them with Fig. 4.5b (without detrending), one can see from the degree fields that the westward propagating signal in the eastern basin at small lags is very weak. It appears, therefore, that much of the AMO signal is lost when linearly detrending the SST anomaly data probably because phase information is lost. This is the reason that no detrending is used.

4.4 PATTERN COMPARISON

To quantify the similarity between the patterns of the relative degree fields in Fig. 4.5a and b, we introduce the conditional Hamming distance H_α. In information theory, the Hamming distance [Hamming, 1950] is the number of positions in two strings of equal length for which the corresponding elements are different [Donges et al., 2009b]. It represents the number of substitutions required to change string into the other and provides a measure of the similarity between two strings.

Here we use the conditional Hamming distance $H_\alpha^j(A,B)$ for each time lag in years j ($j \in [0,30]$) of two degree fields labeled by A and B with relative degree matrices A_{ij} and B_{ij} ($A_{ij}, B_{ij} \in (0,1)$), to quantify the similarity between the averaged relative degree field of the idealized model data and the one of the observations shown in Fig. 4.5a and b. Both degree fields must contain the same length $L = max(i)$ which is determined by the longitude range of the ocean domain chosen. For the degree field of the idealized model data, the longitude range is [-66°E, -10°E] , with the spatial resolution of 4°, it gives $L = 14$. For the degree field of the observations, the longitude range is [-51°E, -9°E] and with the spatial resolution of 3°, it gives the same $L = 14$. Specifically, $H_\alpha^j(A,B)$ is given by

$$H_\alpha^j(A,B) = \sum_{i=1}^{L} XOR(A_{ij}, B_{ij}), \tag{4.9}$$

where

$$XOR(A_{ij}, B_{ij}) = \begin{cases} 1, & \text{if } |A_{ij} - B_{ij}|/B_{ij} > \alpha. \\ 0, & \text{otherwise.} \end{cases} \tag{4.10}$$

This conditional Hamming distance is bounded by $0 \leq H_\alpha^j(A,B) \leq L$ and α is determines how much relative difference between A_{ij} and B_{ij} is allowed.

Considering there are $N_M = 224$ nodes of MICN reconstructed from the idealized model data, while the MICN reconstructed from the observations has $N_O = 308$ nodes, the averaged relative degree fields may be different from each other just because of the different size of CNs. For example, if these two kinds of MICNs are both fully connected CNs, their degree fields should have a relative difference of $(307-223)/223 = 0.38$. Thus we choose $\alpha = 0.15$ to compensate for the different CN sizes, which gives the most significant similarity between the degree fields of the observations and the idealized model data. The blue curve in Fig. 4.8 is the conditional Hamming distance between the relative degree fields of the idealized model data and the observations, allowing for a 15% difference ($\alpha = 0.2$). At small lag, H_α is small but increases up to about a lag of 6 years; a second local minimum occurs around a lag of 15 years.

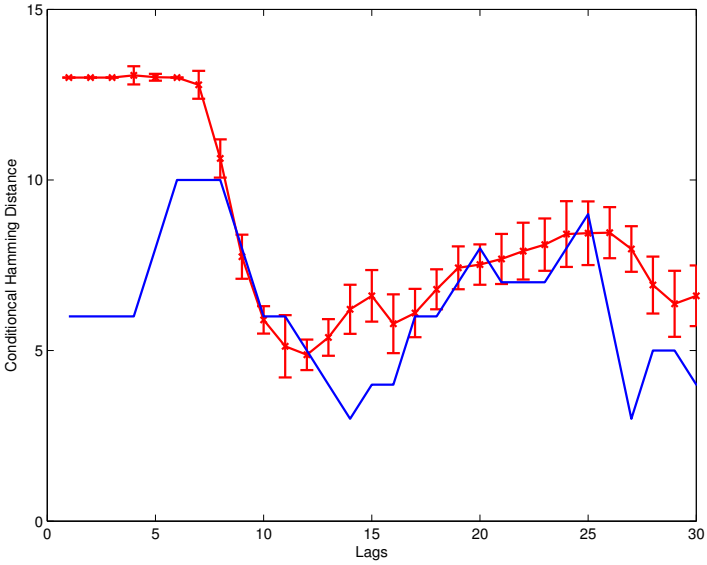

Figure 4.8: *Conditional Hamming distance H_α, between the relative degree field of the idealized model data and that of the observations (blue curve), for $\alpha = 0.15$. The red curve represents H_α between the relative degree field of the idealized model data and that of 200 surrogate data sets derived from the observations through shuffling; the error bars represent the standard deviation in H_α.*

To evaluate the significance of this similarity measure, we use surrogate data obtained by 200 shuffled time series of the observed SST anomalies. We only randomize the sequence of the years and do not shuffle data within a particular year. Hence the probability density function of the observed data is mostly preserved under the shuffling scheme. However, it removes the lagged correlations in the spatial pattern and hence any westward propagation. The red curve in Fig. 4.8 shows the conditional Hamming distance between the relative degree of the MICN reconstructed from the surrogate observations, where the error indicates the standard deviation.

When the lower values of the error bars of the red curve are above the blue curve in Fig. 4.8, the value of the conditional Hamming distances shows a significant similarity between the degree fields of the observations and the idealized model data and hence indicates the existence of westward propagation. Moreover, significance is most prominent near the minima of the blue curve which are in the 10-15 year

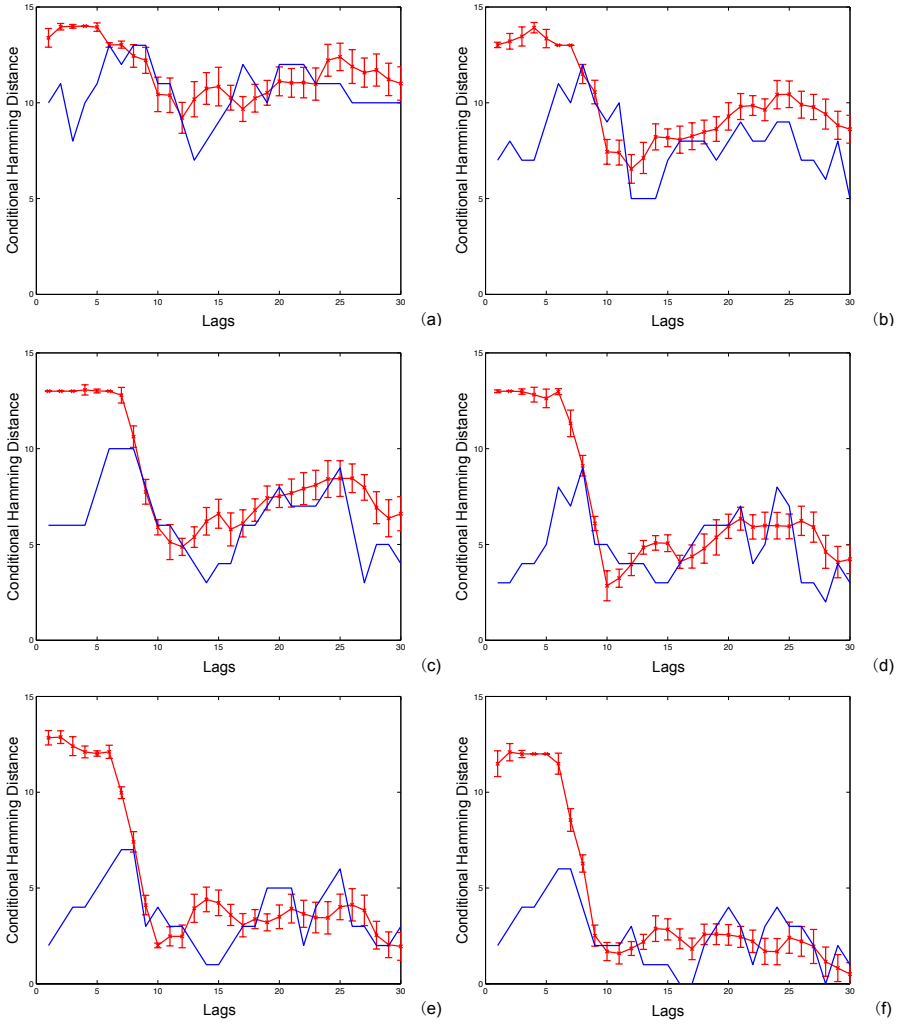

Figure 4.9: *Conditional Hamming distance H_α, between the relative degree field of the idealized model data and that of the observations (blue curve), and between the relative degree field of the idealized model data and that of 200 surrogate data sets derived from the observations through shuffling (red curve, the error bars represent the standard deviation in H_α), for $\alpha =$ (a) 0.05 (b) 0.1 (c) 0.15 (d) 0.2 (e) 0.25 (f) 0.3. There are (a) 75.0% (b) 87.5% (c) 90.2% (d) 75.4% (e) 69.3% (f) 69.5% of the lower values of the error bars of the red curve are above the blue curve.*

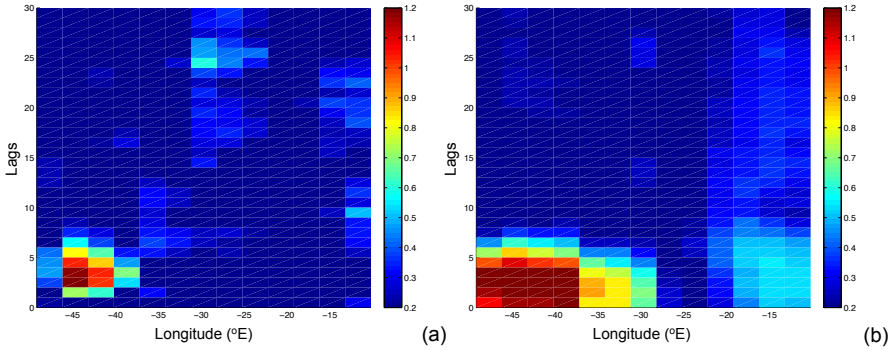

Figure 4.10: *The patterns of relative difference (a) between the relative degree field of the idealized model data and that of the observations, and (b)the relative degree field of the idealized model data and that of 200 surrogate data sets derived from the observations through shuffling.*

and 25-30 year time scale. This result is robust over quite a large range of α values (Fig. 4.9).

To further support our findings, here we also display the relative difference $|A_{ij} - B_{ij}|/B_{ij}$ between the averaged relative degree fields A and B we used to calculate conditional Hamming distances in Fig. 4.8. Fig. 4.10a shows the pattern of relative difference between the averaged relative degree fields of the observations and the idealized model data. The larger relative difference only appear outside of the westward propagating path, which indicates that the westward propagation pattern (such as in the idealized model data) also exists in the observations. Fig. 4.10b shows the pattern of relative difference between the mean degree filed of 200 surrogate data sets of the observations and the idealized model data. High differences occur in the eastern part of the domain, which shows that there is no westward propagation in the surrogate data obtained from the observations.

4.5 DISCUSSION

The thermal Rossby mode mechanism is a promising candidate to explain multidecadal (20-30 years) climate variability in the North Atlantic [Frankcombe et al., 2010]. One of the limitations of the theory is that the spatial patterns of variability have so far only be obtained in ocean-only models [Sevellec and Fedorov, 2013]. One of the main characteristics of the thermal Rossby mode mechanism is the westward propagation of temperature anomalies. Indications for westward propagation were found in observed subsurface temperature fields [Frankcombe et al., 2008] and sea-

level records [Frankcombe and Dijkstra, 2009; Vianna and Menezes, 2013]. However, this property was difficult to distinguish from SST observations because many other processes affect SST in the North Atlantic [Booth et al., 2012; Sutton and Hodson, 2005b].

We have studied the westward propagation of North Atlantic SST anomalies by analyzing the topological properties of MICNs reconstructed from idealized model data (with only the thermal Rossby mode) and from the observations. The relative degree field of the MICNs from the observations show similar propagation properties as the one of MICNs reconstructed from the idealized model results and the conditional Hamming distance provides a quantitative measure of this similarity. Differences between network properties of the MICNs of the idealized model data and the observations may occur due to (i) additional processes affecting SST variability and (ii) the pretreatment of the observations and (iii) the effect of the continental boundaries (in the observations). A limitation of the methodology used here is that it is difficult to determine where these differences originate from.

A good correspondence between observations and idealized model data cannot be clearly seen by using the (linear) Pearson correlation to reconstruct PCCNs. The SST anomaly field is thought to result from advective contributions as well as from a noisy surface heat flux field. In addition, the growth rate of the thermal Rossby mode is known to depend on the time-dependent background state [Dijkstra et al., 2008]. This introduces nonlinear dependencies in the propagation of the mode which may be the reason that the MICN is better suited to detect these features instead of the PCCN.

Finally, this study demonstrates that the CN provides an innovative way to detect spatial propagation of patterns of variability in the climate system. These tools can be directly applied to results from GCMs and can also be extended to look at (lagged) spatial correlations between different fields.

5

CLIMATE NETWORK BASED STABILITY INDEX FOR EL NIÑO VARIABILITY

One of the crucial aspects that is currently limiting the success of El Niño predictions is the stability of the slowly varying Pacific climate. This property determines whether sea surface temperature perturbations will be amplified by coupled ocean-atmosphere feedbacks or not. The so-called Bjerknes stability index has been developed for this purpose, but its evaluation is severely constrained by data availability. Here we present a new promising background stability index based on complex network theory. This index efficiently monitors the changes in spatial correlations in the Pacific climate and can be evaluated by using only sea surface temperature data.

This chapter has been published as:
Q. Y. Feng, and H. A. Dijkstra. Climate Network Based Stability Index for El Niño Variability. *Geophysical Research Letters*, 2015 (resubmitted).

5.1 INTRODUCTION

The development of Pacific sea surface temperature (SST) conditions during the year 2014 has again indicated that we lack a sufficiently detailed understanding of the El Niño-Southern Oscillation (ENSO) phenomenon to predict its developments up to six months ahead with adequate skill. The eastern Pacific equatorial heat content anomalies were very large during March-May 2014 and models predicted strong El Niño conditions by the end of the year. However, the atmospheric response to the associated SST anomalies did not lead to a strong feedback. As a consequence, equatorial Pacific SST anomalies remained relatively small in December and decayed afterwards. The peak of the NINO3.4 index (the area-averaged SST anomalies over the region 120°W-170°W × 5°S- 5°N) in late November 2014 even did not exceed 1.0°C. Early in 2015, warming conditions appeared near the dateline leading to the current (weak) El Niño conditions (http://www.cpc.ncep.noaa.gov/).

After more than thirty years of active research and an initial steep curve toward understanding the basic ENSO processes, the model prediction skill in 2014 appears disappointing. Since ENSO has large effects on the local climate in large parts of the world with severe impacts on nature and society, it is important to (re)consider what processes may be missing or misrepresented in these models.

The Zebiak and Cane (ZC) model [Zebiak and Cane, 1987] is thought to capture the basic processes of ENSO and is used in the suite of models providing predictions of El Niño variability (`http://www.cpc.ncep.noaa.gov/`). Many studies using this model have lead to the recharge-discharge oscillator view of ENSO, where positive Bjerknes feedbacks are responsible for the amplification of SST anomalies and ocean adjustment provides a negative delayed feedback [Jin, 1997; Neelin et al., 1998]. The strength of the feedbacks is represented by a coupling strength, here indicated by μ, which is proportional to the amount of wind-stress anomaly per SST anomaly.

In the ZC model, the (steady or seasonal) background climate (provided by observations) becomes unstable when the strength of the coupled processes exceeds a critical value. The critical boundary $\mu = \mu_c$ is, in dynamical systems theory, referred to as a Hopf bifurcation (steady background state) or a Neimark-Sacker bifurcation (seasonal background state). When $\mu > \mu_c$, oscillatory motion develops spontaneously [Bejarano and Jin, 2008; Fedorov and Philander, 2000] and the spatial pattern of the resulting variability is usually referred to as the ENSO mode. When conditions are such that $\mu < \mu_c$, the ENSO mode is damped and can only be excited by noise [Burgers, 1999; Penland, 1996]. These critical boundaries μ_c have been explicitly calculated for ZC-type models [Jin et al., 1996] and shown to involve the same oscillatory ENSO mode for both steady and seasonal background states.

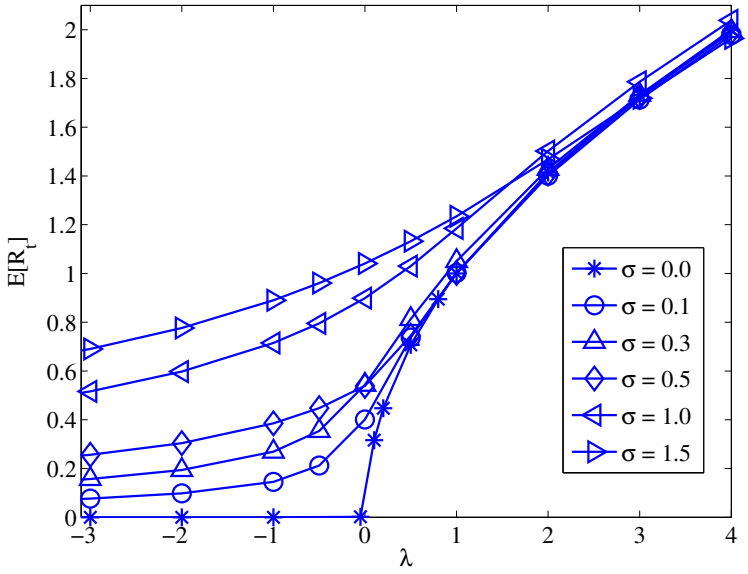

Figure 5.1: *Expected value of R_t of the equation (5.1) near a stochastic Hopf bifurcation. The Hopf bifurcation occurs at the control parameter value $\lambda = 0$ for noise amplitude $\sigma = 0$ (from chapter 4 of [Dijkstra, 2013]).*

The prototype dynamical system displaying this behavior is the normal form of the stochastic Hopf bifurcation, i.e.

$$dX_t = (\lambda X_t - \omega Y_t - X_t R_t^2)dt + \sigma dW_1, \tag{5.1a}$$

$$dY_t = (\lambda Y_t + \omega X_t - Y_t R_t^2)dt + \sigma dW_2, \tag{5.1b}$$

where $R_t = \sqrt{{X_t}^2 + {Y_t}^2}$, λ the control parameter, σ the (additive) noise level and dW_1 and dW_1 are two independent (of each other) Wiener processes. In the deterministic case, the Hopf bifurcation occurs at $\lambda = 0$. When noise is included in this system with an increasing amplitude σ, as shown in Fig. 5.1, there is a response for values $\lambda < 0$, and it increases with the increasing noise level σ. This indicates that oscillatory behaviour can be excited by additive noise when the system is still in the subcritical regime. Applied to the ENSO case, Fig. 5.1 indicates that the oscillatory behaviour can be excited by atmospheric noise when the background Pacific climate is stable [Dijkstra, 2013]; in this case its amplitude is sensitive to the noise strength.

Such a response has been found in typical ZC models when stochastic wind forcing is introduced [Roulston and Neelin, 2000]. Hence, although the noise driven and

sustained ENSO variability are sometimes considered to be two different views, these views are easily reconciled: it just depends on whether the background climate is stable or unstable [Dijkstra, 2013].

In the general circulation model (GCM), both the background state and the growth/-decay of the ENSO mode are controlled by similar coupled processes [Van der Vaart et al., 2000]. In addition, both are also affected by processes outside of the Pacific basin such as those at midlatitudes and in the equatorial Indian and Atlantic Oceans. In these models, the critical boundary separating stable and unstable regimes is not easy to identify. In addition, the model behavior is highly transient due to the fluctuations at sub-annual time scales (such as westerly wind bursts) and external decadal time-scale processes such as a changing radiative forcing.

One successful quantity to analyse the stability of the Pacific climate is the Bjerknes stability (BJ) index [Kim and Jin, 2011a;b; Kim et al., 2014] which is based on the recharge-discharge oscillator framework [Jin et al., 2006]. However, the calculation of the BJ index requires a comprehensive dataset of the mean ocean currents, the mean ocean upwelling, and the zonal and vertical gradients of the mean upper ocean temperature. Moreover, determining the linear correlations between variables in the BJ index formulation requires relatively long time series. Although the BJ index can be applied to reanalysis data, it cannot be used in cases when only SST observations (such as in the period before the TAO/TRITON array) are available or when observational time series are relatively short.

As the stability of the Pacific climate is key to improve the skill in future ENSO predictions [Chen et al., 2004; Fedorov et al., 2003; Yeh et al., 2009], a more practical index (than the BJ index) of the stability of the background state based on only SST data is urgently needed. In this chapter, we develop a new index monitoring the stability of the Pacific climate, building on the success of Climate Network (CN) approaches to efficiently monitor changes in spatial correlations of the atmospheric surface temperature [Gozolchiani et al., 2011], which has also been exploited for ENSO prediction [Ludescher et al., 2013].

5.2 MODEL AND DATA

5.2.1 *ZC model*

To validate the new index, we first use the results from a fully-coupled variant of the original ZC model [Van der Vaart et al., 2000]. The ocean component of this model is a reduced-gravity shallow-water model, and the atmospheric component is a linear, steady-state model [Gill, 1980] forced by SST. In contrast to the original ZC model, this model is not an anomaly model around a prescribed climatological mean state, but the model itself determines the mean climate state and its variability.

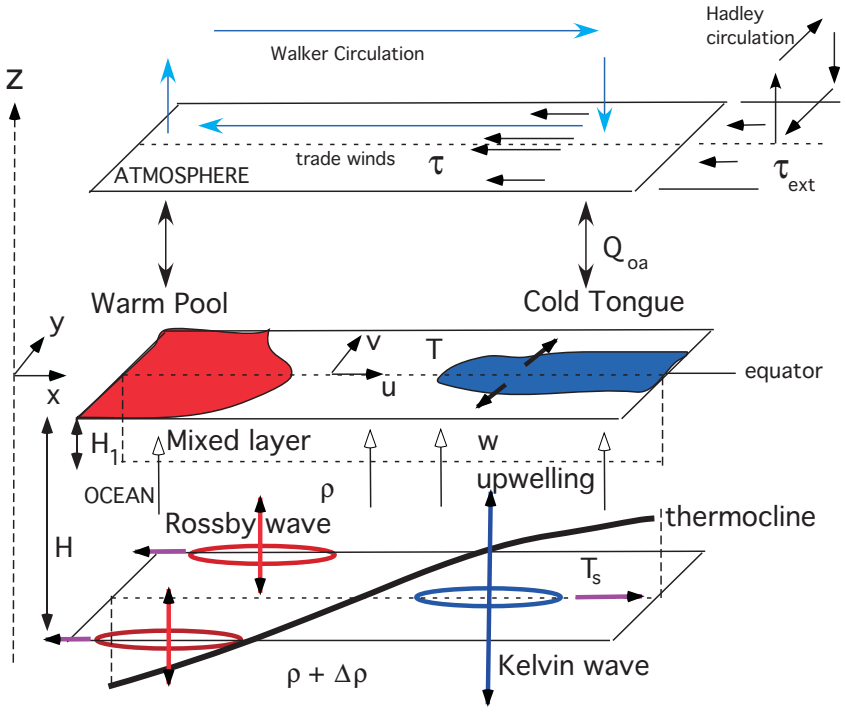

Figure 5.2: *Overview of the oceanic and atmospheric processes of the equatorial coupled ocean-atmosphere system. Figure from [Dijkstra, 2013]*

The ocean is bounded by meridional walls at the west ($x = 0$) and east ($x = L$) coast. The ocean component of the model consists of a well-mixed layer of mean depth H_1 embedded in a shallow water layer of mean depth $H = H_1 + H_2$ having a constant density ρ (see Fig. 5.2). Only long wave motions above the thermocline are considered and the deep ocean (having a constant density $\rho + \Delta\rho$) is assumed to be at rest.

The equations are [Von der Heydt et al., 2011]

$$\frac{\partial u}{\partial t} + a_m u - \beta_0 y v + g' \frac{\partial h}{\partial x} = \frac{\tau^x}{\rho H}, \tag{5.2a}$$

$$\beta_0 y u + g' \frac{\partial h}{\partial y} = \frac{\tau^y}{\rho H}, \tag{5.2b}$$

$$\frac{\partial h}{\partial t} + a_m h + c_0^2 \left(\frac{\partial u}{\partial x} + \frac{\partial v}{\partial y} \right) = 0, \tag{5.2c}$$

with boundary conditions

$$\int_{-\infty}^{\infty} u(0,y,t)\,dy = 0, \;\; u(L,y,t) = 0. \tag{5.3}$$

The equations for the surface (Ekman) layer velocities (u_s, v_s) are

$$a_s u_s - \beta_0 y v_s = \frac{H_2}{H}\frac{\tau^x}{\rho H_1}, \tag{5.4a}$$

$$a_s v_s - \beta_0 y u_s = \frac{H_2}{H}\frac{\tau^y}{\rho H_1}, \tag{5.4b}$$

where $H_2 = H - H_1$. In the equations above, a_m and a_s are linear damping coefficients, in the shallow water and Ekman layer, respectively. $\vec{\tau} = (\tau^x, \tau^y)$ is the wind stress vector, (u_s, v_s) are the Ekman velocities, $g' = g\Delta\rho/\rho$ is the reduced gravity and $c_0 = \sqrt{g'H}$ is the phase speed of the first oceanic baroclinic Kelvin mode.

The zonal wind stress τ^x is decomposed into an external and a coupled contribution:

$$\tau^x = \tau^x_{ext} + \tau^x_c, \tag{5.5}$$

The coupled part of the wind stress is assumed to be proportional to the zonal wind-field u_a, i.e., $\tau^x_c = \gamma_\tau u_a$, with γ_τ a constant. The external wind stress τ^x_{ext} does not depend on the coupled feedbacks within the basin and can be thought of to represent the easterly stress component due the Hadley circulation and it is assumed constant in the zonal direction [Dijkstra and Neelin, 1995]. In the meridional direction the external wind stress is assumed to be symmetric with respect to the equator, having the form [Van der Vaart et al., 2000]

$$\tau^x_{ext} = -\tau_0 e^{[-\frac{(y/L_a)^2}{2}]}, \tag{5.6}$$

where τ_0 is a typical amplitude of the wind stress ($\tau_0 \sim 0.01$ Pa) and L_a the atmospheric Rossby deformation radius. The meridional wind-stress component τ^y is neglected in this model.

The evolution of the sea surface temperature T is described by is

$$\frac{\partial T}{\partial t} + a_T(T - T_0) + \frac{w_1}{H_1}\mathscr{H}(w_1)(T - T_s(h)) + u_1\frac{\partial T}{\partial x} + v_1\frac{\partial T}{\partial y} = 0, \tag{5.7}$$

where a_T is a linear damping coefficient, $u_1 = u_s + u$ and $v_1 = v_s + v$ are the horizontal velocities in the mixed layer, $w_1 = w_s + w$ the vertical velocity just below the mixed layer, $\mathscr{H}$ the Heaviside function and T_0 is the radiation equilibrium temperature. The subsurface temperature T_s depends on the vertical temperature distribution and hence on the thermocline depth h according to

$$T_s(h) = T_{s0} + (T_0 - T_{s0})\tanh(\frac{h + h_0}{\hat{H}}), \tag{5.8}$$

Table 5.1: *Values of parameters used in the ZC model.*

L	=	1.5×10^7	[m]	c_0	=	2	[m/s]
c_a	=	30	[m/s]	H	=	200	[m]
H_1	=	50	[m]				
F_0	=	$\frac{\tau_0 L}{c_0^2\rho H}=0.2$		δ_s	=	0.3	
r	=	$\frac{a_m L}{c_0}=0.1$		η_1	=	$\frac{h}{\hat{H}}=5.01$	
ϵ_s	=	$\frac{a_s L}{c_0}=37.5$		δ	=	1.0	
γ_s	=	$\frac{H_2}{H_1}F_0=3.0$		α	=	$\frac{L_y}{L_a}=0.2$	
Λ_s	=	$\frac{L_y}{L}$		Λ_s	=	$\frac{L_y}{L}=2.0\times10^{-2}$	
ϵ_a	=	$\frac{AL}{c_0}=1.25$		α_w	=	$\frac{H_1}{\hat{H}}=1.0$	
μ	=	$\frac{\alpha_T\Delta T L}{c_a^3}$		η_2	=	$\frac{h_0}{\hat{H}}=0.5$	
ϵ_T	=	$\frac{a_T L}{c_0}=0.694$		T_0	=	30	
δ_w	=	5.0×10^{-2}		T_{s0}	=	23.0	

where h_0 and $\hat{H}$ represent control parameters for the steepness and the offset of T_s profile, and T_{s0} is the characteristic temperature being upwelled into the surface layer.

The ocean model is coupled to a Gill atmosphere model [Gill, 1980] with zonal and meridional velocities (u_a, v_a), geopotential height ϕ and a linear damping coefficient A. The atmosphere is driven by heat fluxes from the ocean that depend linearly on the anomalies of sea surface temperature T with respect to the radiation equilibrium temperature T_0, with proportionality constant α_T. The governing equations of the atmosphere model are

$$\frac{\partial u_a}{\partial t}+Au_a-\beta_0 y v_a-\frac{\partial\phi}{\partial x}=0, \tag{5.9a}$$

$$\frac{\partial v_a}{\partial t}+Av_a+\beta_0 y u_a-\frac{\partial\phi}{\partial y}=0, \tag{5.9b}$$

$$\frac{\partial\phi}{\partial t}+A\phi-c_a^2\left(\frac{\partial u_a}{\partial x}+\frac{\partial v_a}{\partial y}\right)=\alpha_T(T-T_0), \tag{5.9c}$$

where c_a is the phase speed of the atmospheric Kelvin wave.

In order to obtain the proper climatology of the present-day Pacific together with realistic ENSO variability, the standard parameter values, as in Table 5.1, are used.

5.2.2 *The response of the ZC model to the red noise*

In this ZC model, a Hopf bifurcation occurs at $\mu = \mu_c = 3.0$. When the coupling strength is smaller than μ_c, for example $\mu = 2.7$, the system is in the subcritical regime where it exhibits a damped ENSO oscillation when no noise is present. This is shown in the behavior of the NINO3.4 index (red curve) in Fig. 5.3a. When the coupling strength is increased to just above the critical value μ_c, the system will enter the supercritical regime where the NINO3.4 index displays an interannual oscillation (red curve in Fig. 5.3c). The spectrum show a peak at about 4 years (red curve in Fig. 5.3d)).

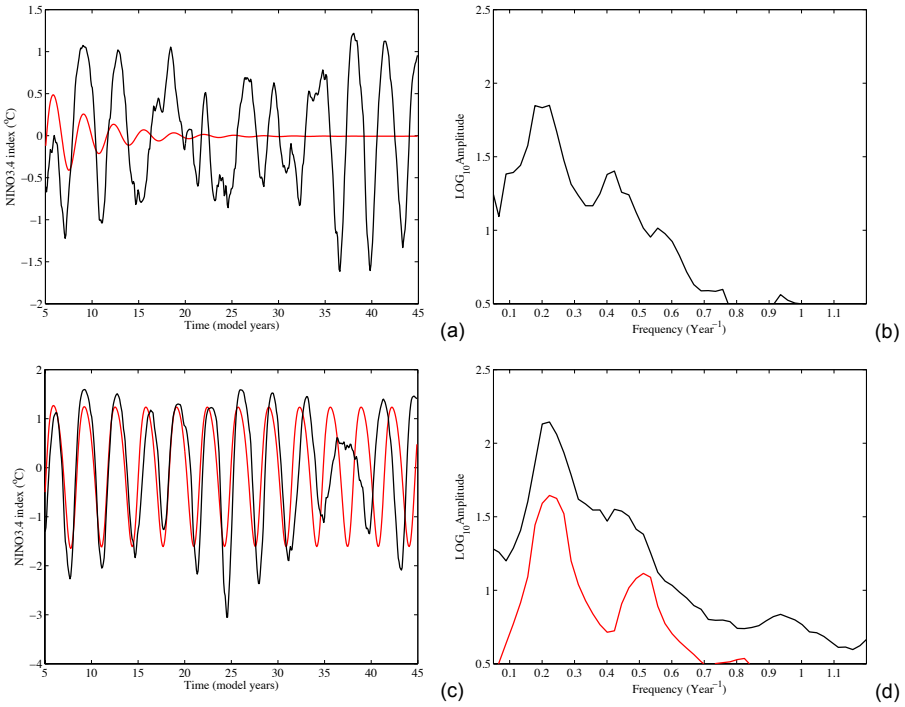

Figure 5.3: *The response of the modified Zebiak and Cane (ZC) model. Red curves are from the model runs without red noise forcing, black curves are from the ones with red noise forcing. (a) The NINO3.4 index from the modified ZC output at the coupling strength $\mu = 2.7$, (b) The amplitude spectrum for (a), (c) Same as (a) but at $\mu = 3.0$, (d) The amplitude spectrum for (c).*

We followed the same procedure of introducing the red noise into the wind-stress forcing (equation 5.6) in the model as in Roulston and Neelin [Roulston and Neelin,

2000]. We used the extended reconstructed sea surface temperature (ERSST) over the Pacific Ocean for the period of 1978-2004 [Smith and Reynolds, 2003], and the Florida State University pseudo-wind-stress data for the same period [Legler and O'Brien, 1988] to get the residual of the wind stress. We first subtracted the part of the wind stress anomalies that is linearly related to ENSO SST anomalies. Then we projected the residual of the wind stress onto its empirical orthogonal function (EOF)s, the first and second EOFs and their principal components (PCs) are shown in Fig. 5.4. Please note that the second EOF (Fig. 5.4b) has the pattern of westerly wind burst (WWB) which are generally located west of the date line [Lian et al., 2014]. Thus the second PC (PC2) can be considered as westerly wind burst time series, in agreement with results in WWB [Lian et al., 2014; Menkes et al., 2014], especially in March 1997 when a strong westerly wind event occurred [Menkes et al., 2014].

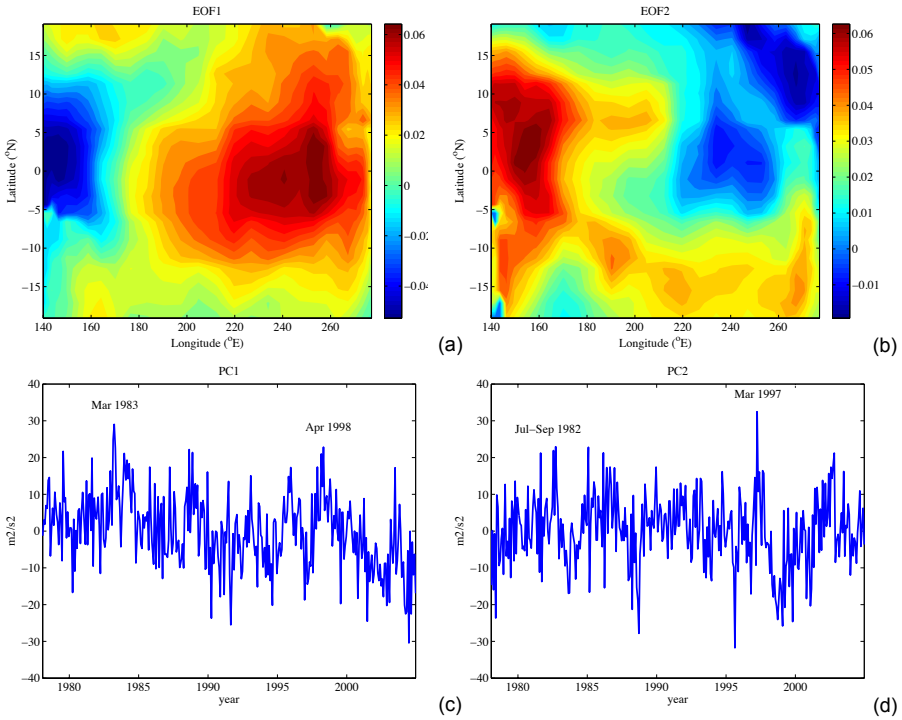

Figure 5.4: *(a)The first empirical orthogonal function (EOF) of the wind stress residual, explaining 11.9% of the variance. (b)The same with (a) but the second EOF, explaining 11.6% of the variance. (c)The first principal component (PC) of the wind stress residual. (d) The same with (c) but the second PC.*

The EOF components of wind stress residual were used to keep the spatial patterns of the red noise, while the PCs were used to produce the time series of red noise. Each red noise time series x_t are modeled as an independent stochastic process using a first order autoregressive model (AR1) described by

$$x_{t+1} = ax_t + \sigma\epsilon_t, \tag{5.10}$$

where a is the lag-1 autocorrelation of each PC and the term $\sigma\epsilon_t$ represents white noise with a variance σ.

The response of the ZC model to the red noise forcing is shown as the black curves in Fig. 5.3a-b (subcritical) and 5.3c-d (supercritical). In the subcritical regime, the red noise is necessary to excite the ENSO mode, while in the supercritical regime, the red noise simply causes a higher amplitude of ENSO variability. This is similar to the results in Roulston and Neelin [Roulston and Neelin, 2000].

For this study, we use ZC model output of 11 simulations, 540 months (45 years) each, at different values of the coupling strength μ (2.70, 2.80, 2.90, 2.95, 2.98, 3.00, 3.02, 3.10, 3.15, 3.25 and 3.40). The Pearson Correlation Climate Network (PCCN)s reconstructed for each value of μ have 30 (longitude) $\times$31 (latitude)$=$ 930 nodes within the domain (140°E, 280°E) $\times$ (20°S, 20°N). A threshold value of $\tau = 0.5$, defining a link between nodes, guarantees that these links are based on significant ($p < 0.05$) correlations.

5.2.3 *BJ index calculation*

The BJ index can be derived using the volume-averaged form of the linearized tendency of an anomalous ocean temperature and balance equations obtained from several systematic approximations [Kim and Jin, 2011b]. The formulation of BJ index is originally given by Jin *et al.* [Jin et al., 2006], and modified by Kim and Jin [Kim and Jin, 2011a] which provides a better approximation of the original SST tendency equation. Here we used the modified formulation used by Lübbecke and McPhaden [Lübbecke and McPhaden, 2013] as the following:

$$2I_{BJ} = -\left(\frac{\langle\bar{u}\rangle_E}{L_x} + \frac{\langle -2y\bar{v}\rangle_E}{L_y^2} + \frac{\langle\bar{w}\rangle_E}{H_m}\right) \tag{5.11a}$$

$$-\alpha \tag{5.11b}$$

$$+\mu_a\beta_u\left\langle -\frac{\partial\bar{T}}{\partial x}\right\rangle_E \tag{5.11c}$$

$$+\mu_a\beta_w\left\langle -\frac{\partial\bar{T}}{\partial z}\right\rangle_E \tag{5.11d}$$

$$+\mu_a\beta_h\left\langle \frac{H(\bar{w})\bar{w}}{H_m}a_h\right\rangle_E \tag{5.11e}$$

where term (5.11a) is mean advection and upwelling (DD); term (5.11b) is thermal damping rate (TD), in the ZC model α is specified as a constant, here $\alpha = 3.0\ yr^{-1}$; term(5.11c) is zonal advection feedback (ZAF); term (5.11d) is Ekman pumping feedback (EF); term (5.11e) is thermocline feedback (TF). $\bar{u}, \bar{v}, \bar{w}$ denote the climatological mean zonal, meridional, and vertical velocity, respectively; $\bar{T}$ represents climatological mixed-layer ($H_1 = 50$ m) ocean temperatures; $\langle\cdot\rangle$ denotes the volume-averaged quantities over the eastern (140°E, 210°E) or western region (210°E, 280°E) of the equatorial Pacific basin, which are recognised by the subscripts E and W; L_x and L_y are the longitudinal and latitudinal extent of the eastern region, and y is the distance from the equator; H_m represents the effective depth for the vertical advection, here $H_m = H_1/0.75$ m; $\mathscr{H}(x) = \{^{1,\ x>0}_{0,\ x\leq 0}$ is the Heaviside function which ensures that only upstream vertical advection is taken into consideration.

The coefficients in equation (5.11) are computed from approximated balance equations based on the recharge oscillator [Kim et al., 2014], using the least-squares regression method. Fig. 5.5 shows an example of the regressions that uses the data from the ZC model output at the coupling strength $\mu = 3.0$. μ_a describes the wind response to SST forcing, and it can be estimated by $[\tau_x] = \mu_a \langle T \rangle_E$, as shown in the Fig. 5.5a, here $[\tau_x]$ is zonal wind stress anomalies averaged over the entire equatorial area; β_u describes the ocean surface zonal current response to wind forcing, and it can be estimated by $\langle u \rangle_E = \beta_u [\tau_x] + \beta_{uh} \langle h \rangle_W$, as shown in the Fig. 5.5b, here h is the thermocline depth; β_w describes the upwelling response to wind forcing, and it can be estimated by $\langle H(\bar{w}) w \rangle_E = -\beta_w [\tau_x]$, as shown in the Fig. 5.5c; β_h describes the thermocline slope response to wind forcing, and it can be estimated by $\langle h \rangle_E - \langle h \rangle_W = \beta_h [\tau_x]$, as shown in the Fig. 5.5d; a_h describes the effect of thermocline depth changes on subsurface temperature, and it can be estimated by $\langle H(\bar{w} T_{sub}) \rangle_E = a_h \langle h \rangle_E$, as shown in the Fig. 5.5e, here T_{sub} is the subsurface temperature.

5.3 RESULTS

5.3.1 *From the ZC model*

We first reconstructed the PCCN for the SST data from ZC-model. The degree fields of the PCCNs reconstructed for four values of μ are shown in Fig. 5.6a-d. When the coupling strength μ is increased from the subcritical $\mu < \mu_c$ to the supercritical regime $\mu > \mu_c$, more nodes in the region between 220°E and 280°E get a higher degree. When the critical boundary is approached, the spatial pattern of the anomalies is more and more controlled by the ENSO mode, leading to large-scale coherence which is efficiently captured by the network degree field. Another distinct change of the degree fields (Fig. 5.6a-d) is that the propagating patterns of equatorially symmetric

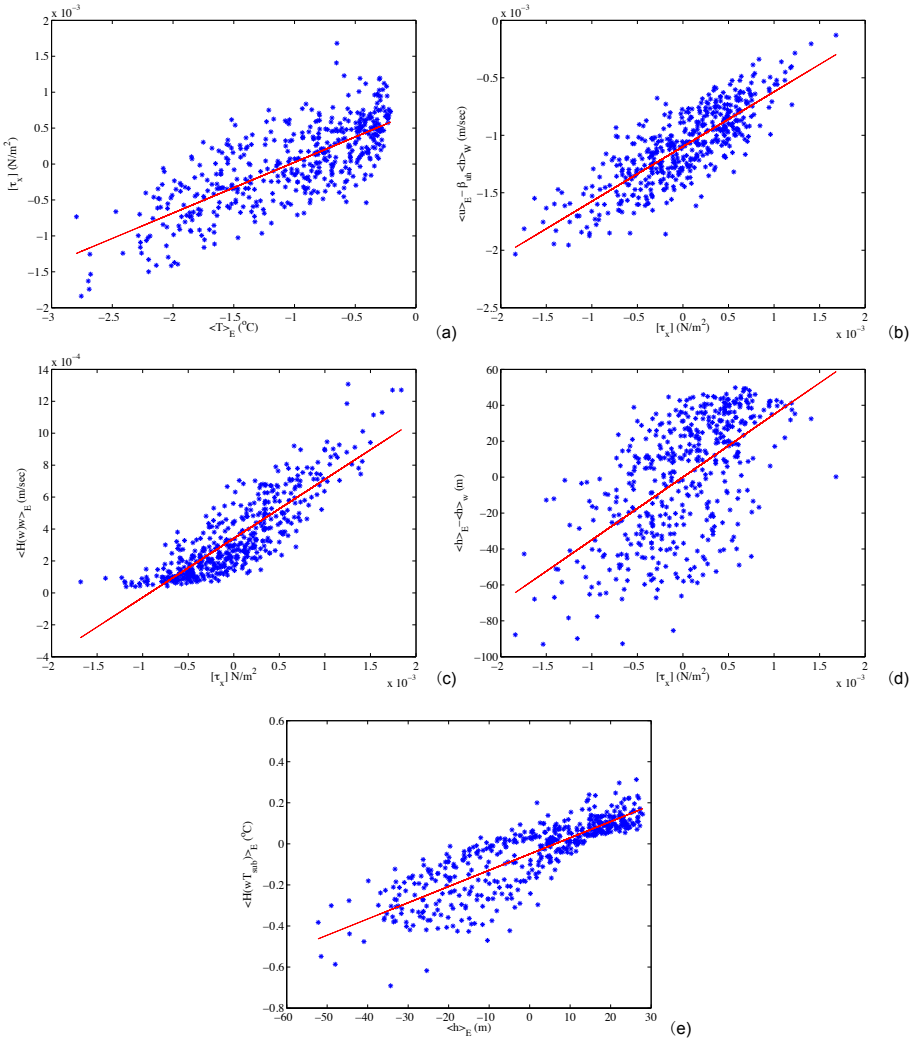

Figure 5.5: *The scatter plots with a regression fitting line for (a)* $[\tau_x] = \mu_a \langle T \rangle_E$ *(r = 0.57), (b)* $\langle u \rangle_E = \beta_u [\tau_x] + \beta_{uh} \langle h \rangle_W$ *(r=0.64), (c)* $\langle H(\bar{w}) w \rangle_E = -\beta_w [\tau_x]$ *(r=0.73), (d)* $\langle h \rangle_E - \langle h \rangle_W = \beta_h [\tau_x]$ *(r=0.35), (e)* $\langle H(\bar{w} T_{sub}) \rangle_E = a_h \langle h \rangle_E$ *(r=0.71). The data is from the modified Zebiak and Cane (ZC) model output at the coupling strength* $\mu = 3.0$.

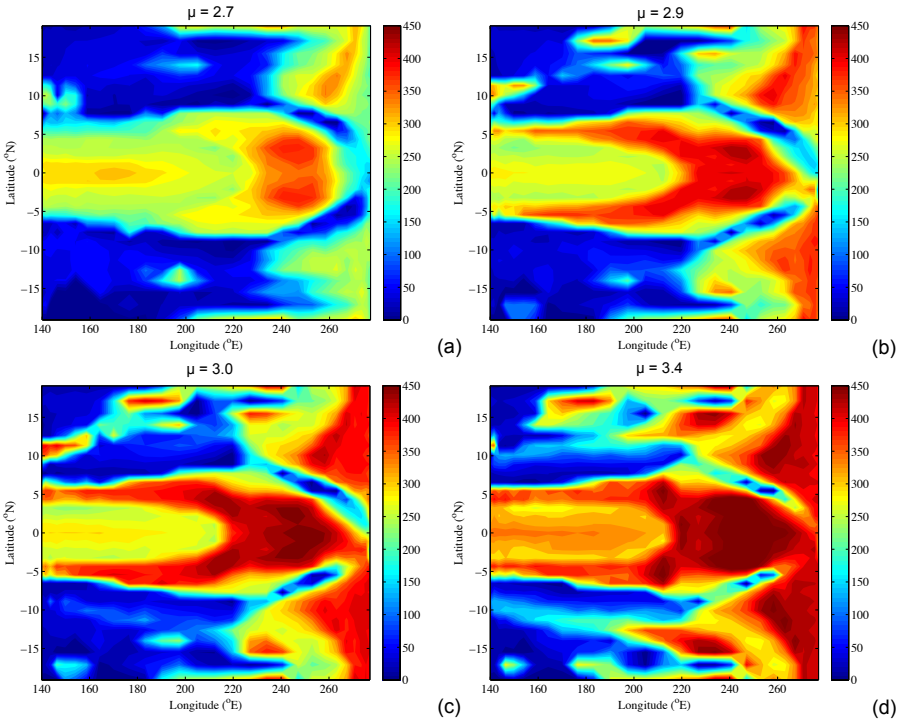

Figure 5.6: *(a) Degree field of the PCCN using a threshold $\tau = 0.5$ reconstructed from the ZC model data at the coupling strength $\mu = 2.7$. (b) Same as (a) but at $\mu = 2.9$. (c) Same as (a) but at $\mu = 3.0$. (d) Same as (a) but $\mu = 3.4$.*

Rossby waves are becoming more prominent when the background state enters the supercritical regime.

Histograms of the degree fields (the degree distributions) for two different values of μ are plotted in Fig. 5.7a-b. For $\mu = 2.7 < \mu_c$ (Fig. 5.7a), the degree distribution is bimodal, where the first peak represents the low degree nodes in Fig. 5.6a and the second peak (located near 250) represents the high degree nodes. When μ is increased (Fig. 5.7b) a peak at even higher degree occurs representing the higher degree nodes appear in Fig. 5.6c, because the ENSO mode becomes more dominant in the SST anomalies when the background climate moves into the supercritical regime [Feng et al., 2014; Mheen et al., 2013].

The changes in the degree distributions with μ can be effectively measured by the skewness of the degree distribution S_d. When the mass of the distribution is concentrated more to the right like in Fig. 5.7b which leads to a lower skewness

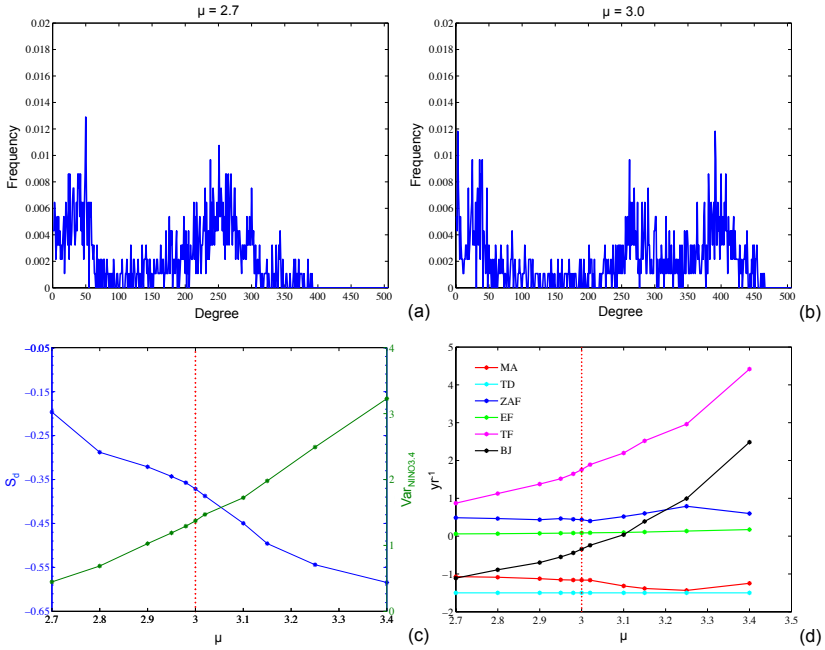

Figure 5.7: *(a) Degree distribution of the PCCN using a threshold $\tau = 0.5$ reconstructed from the ZC model data at the coupling strength $\mu = 2.7$. (b) Same as (a) but at $\mu = 3.0$. (c) The degree skewness index S_d (blue) and the variance of NINO3.4 index $Var_{NINO3.4}$ (green) from the ZC model as a function of μ ($\mu_c = 3.0$, red dash line). (d) The values of Bjerknes stability (BJ) index and its components from the ZC model at different μ ($\mu_c = 3.0$, red dash line): mean advection and upwelling (MA, red), thermal damping (TD, cyan), zonal advection feedback (ZAF, dark blue), Ekman pumping feedback (EF, green), thermocline feedback (TF, magenta), and total BJ index (BJ, black).*

value, thus S_d is monotonically decreasing with increasing μ (blue curve in Fig. 5.7c). There is also a good correlation between S_d and the variance of the NINO3.4 index ($Var_{NINO3.4}$, green curve) as shown in Fig. 5.7c. However, note that at high values of S_d (stable climate, $\mu < \mu_c$), the amplitude of NINO3.4 depends on the noise (cf. Fig. 5.1).

For these ZC-model results, the BJ index (the black curve in Fig. 5.7d) is monotonously increasing with increasing μ and crosses the zero line at about $\mu = 3.1$ which is close to μ_c. This indicates that the BJ index reasonably (but not perfectly) monitors the stability of the background state for this case, which is in accordance with results in [Jin et al., 2006]. The values of different terms in the BJ index (also shown in Fig. 5.7d) indicate that the thermocline feedback is dominant in destabilizing the background state. It has been shown in models [Kim and Jin, 2011b; Kim et al., 2014]

and reanalysis data [Kim et al., 2014] that this feedback has been dominant during past ENSO events. Therefore, when the background state of Pacific climate evolves so that closes to the critical boundary ($\mu = 3.0$ in the ZC model), there is critical slow down and hence the appearance of long-range correlations between SST time series (Fig. 5.6c-d). These correlations are caused by the amplification of SST anomalies by the thermocline feedback, and can be measured by the network degree field based index S_d (Fig. 5.7c).

5.3.2 *From CMIP5 models*

In [Kim et al., 2014], the BJ index is computed from the the 5th Coupled Model Intercomparison Project (CMIP5) model ensemble for the greenhouse warming scenario. To demonstrate that the degree skewness index S_d contains similar information as the BJ index, we reconstruct PCCNs from an ensemble of five CMIP5 GCMs (CCSM4, GFDL-CM3, GFDL-ESM2M, GISS-E2-R, NorESM1-M) from the BEST9 models used in [Kim et al., 2014] under the historical (1910-2005) and greenhouse warming (representative concentration pathway 8.5) conditions (2006-2100). Here, we first remove the trends from the data with a 10-year sliding window, then choose the same size of a sliding windows of 50 years (as in [Kim et al., 2014] for the BJ index) to calculate S_d values.

The results are shown in Fig. 5.8. The Pearson correlations (cor) between S_d indices (blue curves) and the BJ indices (green curves) are significant ($p < 0.05$) with $cor = -0.857$ in CCSM4, $cor = -0.148$ in GFDL-CM3, $cor = -0.486$ in GFDL-ESM2M, $cor = -0.879$ in GISS-E2-R, $cor = -0.689$ in NorESM1-M, and $cor = -0.868$ in the ensemble mean. We also calculated the Fisher weighted mean correlation coefficient of S_d indices and the BJ indices in these five CMIP5 CGCMs as follows: first transform the cor values into Z transformation [Fisher, 1915] by

$$Z = \frac{1}{2} ln[\frac{(1+r)}{1-r}], \tag{5.12}$$

then obtain the Fisher weighted mean correlation coefficient $\bar{r}$ by [Faller, 1981]

$$\bar{r} = \frac{e^{\bar{z}} - e^{-\bar{z}}}{e^{\bar{z}} + e^{-\bar{z}}}, \tag{5.13}$$

where $\bar{z}$ is the mean value of Z in these five CMIP5 GCMs . Here $\bar{r} = -0.684$. Thus the S_d index is significantly and strongly anti-correlated with BJ index.

The ensemble mean result in Fig. 5.8f is a nice example to show the anti-correlation between S_d index and BJ index. From 1910 to around 1960, S_d index slightly increases, and at the same time BJ index decreases a bit, which means the stability of Pacific climate increases. From 1980 to around 2020, the S_d index drops to the lowest level, while the BJ index reaches its climax, both indicating that the Pacific

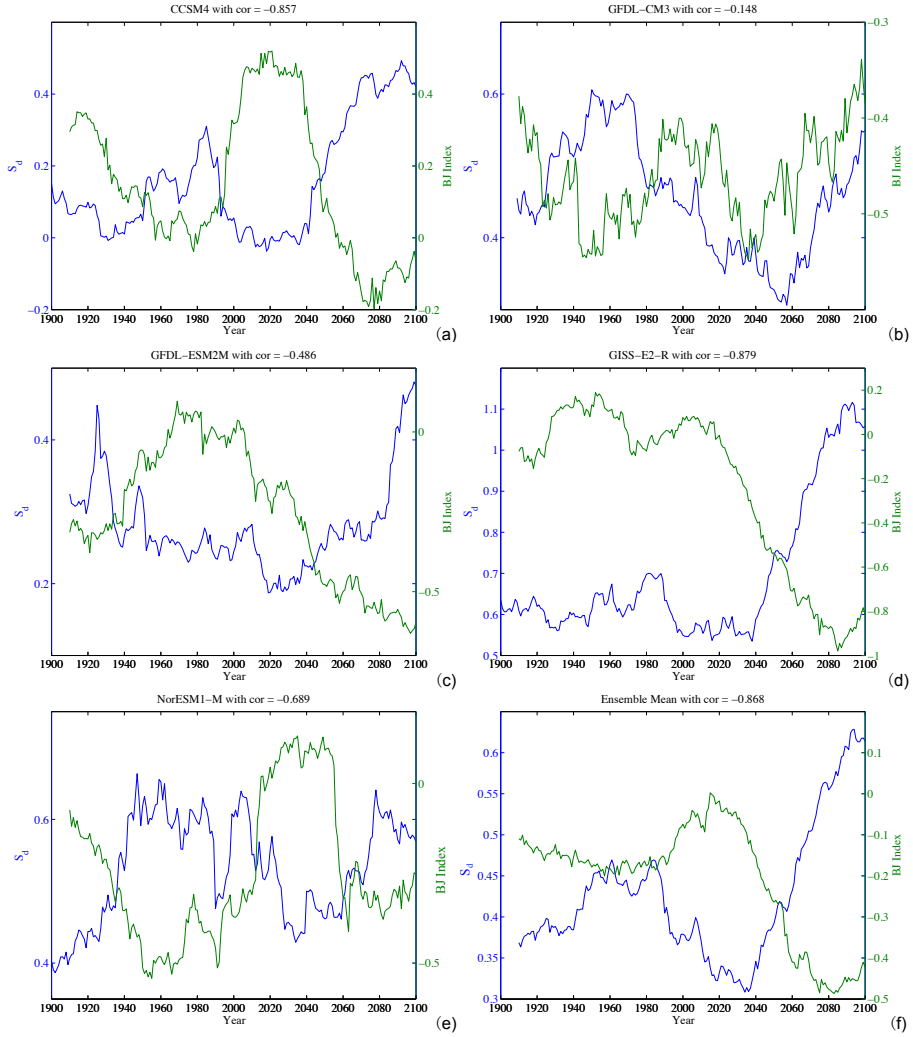

Figure 5.8: *The 50-year sliding window degree skewness index S_d (blue) and BJ index (green) in [Kim et al., 2014] from the historical runs over the period 1910-2005 and the RCP8.5 experiments over the period 2006-2100 of the CMIP5 GCMs (a) CCSM4, (b) GFDL-CM3, (c) GFDL-ESM2M, (d) GISS-E2-R, (e) NorESM1-M, and (f) ensemble mean. The Pearson correlations (cor) between S_d and BJ index stated in the subtitle are all significant ($p < 0.05$).*

climate becomes quite unstable. From around 2040 to 2100, the S_d index decreases and BJ index increases quickly, which indicates that the Pacific climate becomes more stable. This result is in accordance with [Kim et al., 2014].

5.3.3 *From observational data*

Next, we reconstruct PCCNs for the observed monthly mean SST data (the Hadley Centre Sea Ice and Sea Surface Temperature (HadISST) dataset [Rayner et al., 2003a]) over the period December 1951-November 2014. The data were interpolated on a 31 × 30 grid also within the domain (140°E, 280°E) × (20°S, 20°N). A threshold value of $\tau = 0.5$ is chosen to guarantee that connections between nodes are based on significant ($p < 0.05$) correlations.

We first focus on two major ENSO events over the last 60 years, which NINO3.4 index peaked in 1982 and 1997. To show the different network properties for these individual ENSO events, we used monthly SST data of 4 years surrounding the peak of the event (two years before and one year after the year in which the peak occurred). Fig. 5.9a-b indicate that the degree fields of the PCCNs reconstructed for these two major ENSO events are substantially different. The pattern for the 1997 event displays a much larger area of high degree than that of the 1982 event which is more localized and has a smaller degree.

To monitor the changes in the stability of the Pacific climate, we applied the stability index S_d to the HadISST dataset over the period December 1951- November 2014. We reconstructed a PCCN for every 10 years of monthly SST data and computed the value of S_d for this network. By implementing a sliding-window strategy with a shift of one month, we obtained a time series of S_d (black curve in Fig. 5.9c), showing the variation of the stability over the Pacific background climate over the last 60 years. The 3-month running mean of NINO3.4 index of the same period is plotted as the green curve in Fig. 5.9c. We also marked the S_d values of the 1982 and 1997 events, clearly indicating that the S_d value at the onset of the 1982 ENSO event (January-March averaged value of $S_d = 0.03$ in 1982) is much higher than the one of the 1997 event (January-March averaged value of $S_d = -0.37$ in 1997). Actually, the value of S_d was overall low (less stable background state) during the early 90s with a global minimum just before the 1997 event.

The relatively high value of S_d in early 1982 indicates that noise must have had a large influence on the development of the 1982 El Niño event. To verify this statement, the PC2 of the wind stress residual from National Centers for Environmental Prediction (NCEP) wind stress data [Kalnay and coauthors, 1996] is also plotted as the magenta curve in Fig. 5.9c, which can be considered as representing the westerly wind bursts (WWBs) [Lian et al., 2014; Menkes et al., 2014]. One can see that high noise variability was presented during early 1982. Another similar case is the

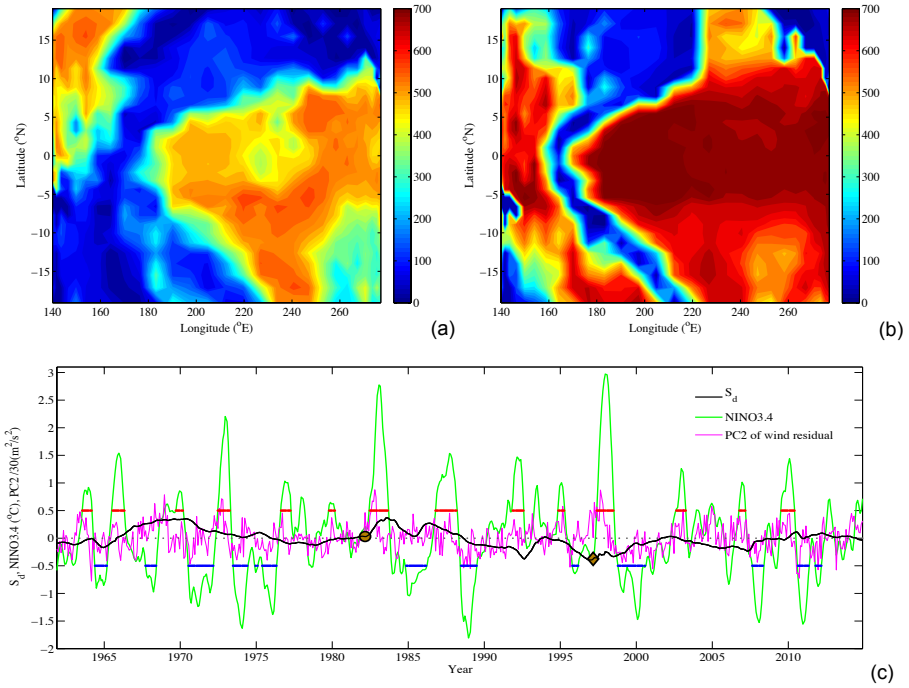

Figure 5.9: *(a) Degree field of the PCCN using a threshold $\tau = 0.5$ reconstructed from the observed SST of Jan 1980 to Dec 1983. (b) Same as (a) but of Jan 1995 to Dec 1998. (c) The 10-year sliding window degree skewness index S_d (black curve) and the 3-month running NINO3.4 index (green curve) from the observed SST of Dec 1951 to Nov 2014, and the second principal component (PC2) of the wind residual (magenta curve) from NCEP zonal windstress data of the same period. The x-axis indicates the end time of the sliding window. The brown disk indicates the mean S_d value of the window ending at January-March 1982, and the brown diamond indicates that of January-March 1997. The red (blue) lines indicate El Niño (La Niña) events that a five consecutive 3-month running mean of NINO3.4 index that is above (below) the threshold of $+0.5°C$ $(-0.5°C)$.*

El Niño event in 1972 which has a relatively stable background state, as indicated by the slightly positive value of S_d, and also high noise variability.

5.4 DISCUSSION

Using techniques of CN [Donges et al., 2009a; Tsonis and Swanson, 2006] we have developed a novel index S_d which provides a simple and adequate measure of the stability of the Pacific climate both in models and observations. The index S_d measures the skewness of the degree distribution of an interaction network determined from significant correlations between the SST anomalies at the nodes.

We tested the index S_d using results from the ZC model for which the stochastic Hopf bifurcation transition behavior applies [Roulston and Neelin, 2000]. The index S_d is anti-correlated with the variance of the NINO3.4 index (under a fixed wind-stress noise amplitude), so a high value of S_d indicates a high stability of the background state. Moreover, a strong support that S_d monitors the stability of the background state comes from the anti-correlated behaviors with the BJ index as determined for an ensemble of five CMIP5 CGCMs for the RCP8.5 scenario (CCSM4, GFDL-CM3, GFDL-ESM2M, GISS-E2-R, NorESM1-M) from the BEST9 models used in [Kim et al., 2014] (cf. Fig. 5.8). Our index S_d is far more easy to compute than the BJ index as it only requires SST data and hence it is more widely applicable. Moreover, since index S_d doesnot require defining the thermocline or mixed layer depth which introduces many more shades of uncertainty, it can be served as an easier model inter-comparison tool than the BJ index.

The same with the BJ index, the S_d index can be considered as an ordinal index for the stability of the Pacific climate, i.e., a background state with a smaller value of S_d is more unstable than one with larger S_d. Thus, we cannot distinguish subcritical from supercritical regimes through absolute values of S_d.

Our results in Fig. 5.9c show nicely the problems which are faced with El Niño prediction. Noise, here through westerly wind bursts (WWBs), is important to induce SST anomalies but whether an El Niño and La Niña will develop depends on the Pacific climate stability that varies on decadal time scales. One can have an El Niño when noise is large even when the background stability is high (as in 1982) and also an El Niño when background stability is low (such as in 1997), however, the lower stability might be one of the reasons that the 1997 event developed into the "El Niño of the century". Note that also the WWBs are not independent of SST development [Eisenman et al., 2005], although we try to filter that out in determining the noise product.

From Fig. 5.9c, it is also interesting to see that the S_d index increased in the beginning of the year 2014, indicating that the Pacific climate became more stable. This is consistent with the fact that although large subsurface temperature anomalies developed in March 2014, there was no growth of SST anomalies because the thermo-

cline feedback was weak and no strong El Niño event could develop. In this way, we hope that our new index can provide an additional tool which can help improve future El Niño predictions.

6

IMPROVING THE SKILL OF EL NIÑO PREDICTIONS USING MACHINE LEARNING TECHNIQUES AND NETWORK MEASURES

The El Niño-Southern Oscillation (ENSO) phenomenon is a dominant mode of interannual climate variability with large impacts on nature and society. However, a good skill of present-day dynamical and statistical model predictions of El Niño occurrences is limited to a few months ahead. Recently, Climate Network (CN) based indicators of El Niño occurrence have been developed using CNs either reconstructed from sea surface temperature or from atmosphere surface temperature data. Here we use these measures in a machine learning approach to develop new schemes for El Niño prediction. We present one scheme that can give a skillful prediction for the occurrence of El Niño events one year ahead, and another scheme provides reasonable NINO3.4 index forecasts with a lead time of three months.

This chapter is based on:
Q. Y. Feng, R. Vasile, M. Segond, A. Gozolchiani, Y. Wang, A. Tantet, M. Abel, S. Havlin, A. Bunde, and H. A. Dijkstra. Improving the Skill of El Niño Predictions Using Machine Learning Techniques and Network Measures. *Geoscientific Model Development*, 2015 (submitted).

6.1 INTRODUCTION

The occurrence of an El Niño event has large impacts on the weather around the Pacific causing many climate-related disasters, such as droughts in Australia and torrential rains in South America [Reilly, 2009]. For the adaptation to such events, it is therefore crucial to develop skillful predictions for whether such an event will occur (say one year ahead) and if so, how the events will develop in time.

Since the 1990s, both dynamical models and statistical models have been used to predict El Niño events [Chen et al., 2004; Fedorov et al., 2003; Latif and Barnett, 1994; Yeh et al., 2009]. Although the fact that about 20 models currently provide El Niño-Southern Oscillation (ENSO) forecasts routinely, a good skill is generally limited to about 6 months ahead. The reason is the presence of a so-called "spring predictability barrier", where errors are greatly amplified due to the coupled feedbacks in the equatorial ocean-atmosphere system [Duan and Wei, 2013; Goddard et al., 2001]. Moreover, the prediction for the development of El Niño events (e.g. NINO3.4 forecast) is still disappointing.

As shown in Fig. 6.1, during March-May 2014 most of the models predicted strong El Niño conditions by the end of 2014. However, equatorial Pacific sea surface temperature (SST) anomalies remained relatively small and the peak of the NINO3.4 index (the area-averaged SST anomalies over the region [120°W- 170°W × 5°S- 5°N]) in late November 2014 even did not exceed 1.0°C. Only by early 2015, warming conditions appeared near the dateline, and have subsequently developed into a weak El Niño event (`http://www.cpc.ncep.noaa.gov/`).

Recently, the applications of Climate Network (CN) to surface temperature observations of the Tropical Pacific has shown that the links based on the spatial correlations of the temperature anomalies tend to weaken significantly during El Niño events [Yamasaki et al., 2008]. The changes in the links also show that the emergence of El Niño acts as an autonomous component in the CN [Gozolchiani et al., 2011]. A large-scale cooperative mode, linking the El Niño basin and the rest of the ocean builts up one calendar year before the warming event [Ludescher et al., 2013]. Based on such findings on the temporal evolution of the CN, [Ludescher et al., 2014] developed a forecasting scheme for El Niño events. According to them, a threshold on the average link weight in the reconstructed CN (Fig. 6.2) can skillfully predict an El Niño event one year ahead. However, the average link weight of the network [Ludescher et al., 2013] may not capture the full picture of the dynamics of ENSO and thus limit the skill of the prediction.

Machine learning techniques have been increasingly employed in the study of generalization from data, especially to the predictions that are difficult to solve by traditional statistics [Mitchell, 1997]. One recent example of prediction using machine learning is solar energy prediction for solar power plants [Sharma et al., 2011]. This

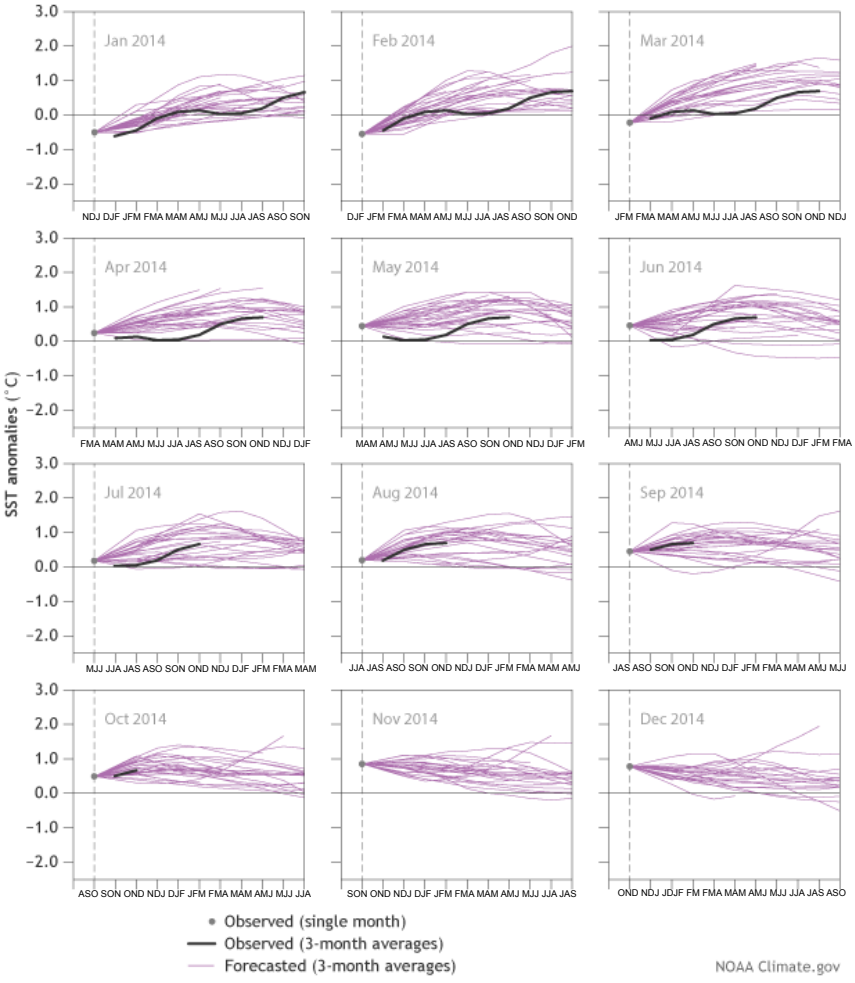

Figure 6.1: *Model forecasts of 3-month averaged SST anomalies in the NiNO3.4 region (120°W-170°W × 5°S-5°N) in 2014. Each purple line represents the ensemble mean forecast from a different model. The black line shows the SST observations from ERSSTv3b (NOAA-NCDC) and the grey, dashed vertical line is the forecast starting point using observed conditions (Figure from* `http://www.climate.gov/`*).*

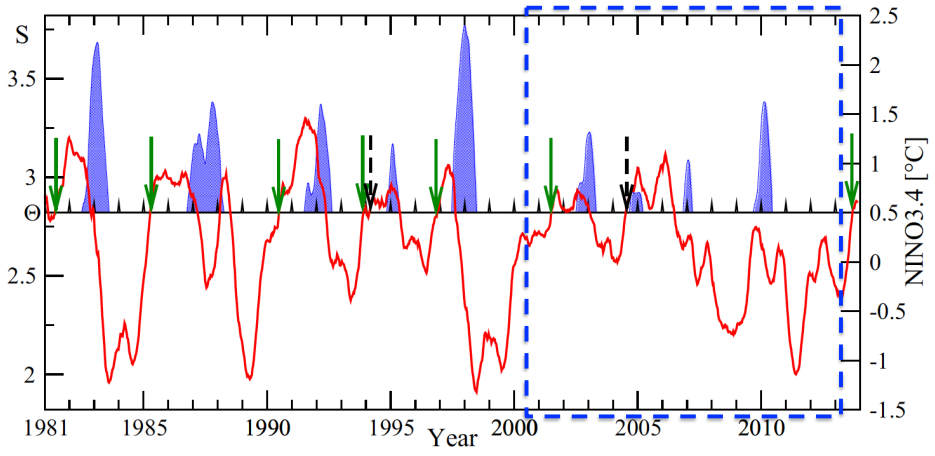

Figure 6.2: *Climate network based El Niño forecasting scheme proposed by [Ludescher et al., 2014]. The red curve is the average link weight S of the network, the horizontal line indicates the decision threshold $\theta = 2.82$, and the solid blue areas show the El Niño events between January 1981 and November 2013. When the link weight crosses the threshold from below, an alarm is given that an El Niño event will start in the following calendar year. Correct predictions are marked by green arrows and false alarms by dashed arrows. The blue dashed rectangle indicates the period of the test set we used for prediction by implementing the machine learning toolbox. Figure is adopted from [Ludescher et al., 2014].*

prediction task can be reduced to learning how the solar plant reacts to the climatic conditions, and predicting the future response of the plant using weather forecasts. Machine learning has shown to be very efficient in prediction, however, it also has shown to require some adaptations, in particular to be able to take into account the temporal aspects, like gradient over preceding time steps [Bishop et al., 2006].

When machine learning techniques are applied to the prediction of climate variability using data from CNs, the task is then to "learn" on the dynamics of the climate system from past states and then be able to predict its future states. The originality and advantage of this approach is that the temporal information is already contained in the measures of CN, so the machine learning techniques will, by default, take it into account in making predictions of the future states of the system. This is a big advantage that is not that common in most of the applications where machine learning is used for prediction.

In this chapter, we present a machine learning toolbox using the measures of CNs to improve the skill of El Niño predictions, especially for the occurrence of El Niño events and the development of NINO3.4 index.

6.2 MACHINE LEARNING TOOLBOX

The machine learning toolbox is presented as a software package written in python 2.7, and it also makes full use of the open source software packages written in Java, namely Weka (available at `http://www.cs.waikato.ac.nz/ml/weka/`) and ECJ (available at `https://cs.gmu.edu/~eclab/projects/ecj/`). This toolbox allows for basic operations of data mining, i.e. reading, merging, and cleaning data, as well as more sophisticated processes of building time-ordered training and test sets, and calling the scripts for the machine learning methods, such as decision trees, artificial neural networks (ANNs) and genetic programming (GP). Of course, the full software package contains more general functions for data mining, and allows for more machine learning methods that we do not employ in this chapter.

6.2.1 *Algorithm overview*

The algorithms for machine learning can be divided into three main categories [Russell and Norvig, 2003]: supervised learning, unsupervised learning, and reinforcement learning. Supervised learning aims at building a statistical or deterministic model from labeled instances, thus it needs a certain proportion of the available data as the training set, then it applies this model to find the unlabelled instances in the rest of the available data, namely the test set. On the contrary, there is no labelled instances in unsupervised learning, and the goal is to find hidden structures (e.g. clustering) in the available data on its own. In reinforcement learning, a certain goal is pursued in a dynamic environment without knowing explicitly whether the goal is coming close or not, and the learning process is driven by the feedbacks from the environment [Bishop et al., 2006].

For the prediction for the occurrence of El Niño events, since the available data is a labelled set, where each instance (El Niño event) has an outcome belonging to a finite set, i.e. occurrence or absence of an El Niño event, we will employ supervised learning algorithms to tackle this classification task. For the prediction for the development of NINO3.4 index, it is a typical regression task, thus supervised learning algorithms also apply.

Therefore, the goal of the supervised learning algorithms used in this chapter is to find good predictor models, avoiding under training and overfitting on the training set, which can label the El Niño events with few false alarms or misses in the test set, or give predicted NINO3.4 values with a small normalized errors from the actual ones. This goal can be achieved in many ways, such as, by varying the number of attributes in the available data, or by extending the training set to incorporate more labelled instances, or by tuning the specific algorithm parameters, e.g. the structures of ANNs.

The standard procedure of the supervised learning is as follows: the predictor model that generates reasonable prediction is constructed by performing an appropriate method (e.g. ANNs or GP) on a training set, and then tested on a test set for validity. When the predictor model is validated, the last part of the test set can be used for prediction.

6.2.2 *Methods overview*

For El Niño predictions, we mainly use the ANNs and GP as main machine learning methods.

The ANN is a powerful method to find highly non linear boundaries for classification problems, or non-linear functions for regression problems [Zou et al., 2009]. It is derived by the working principle of a real neural network, thus has a multilayer structure – an input layer, an output layer, and few/many/none hidden layers, in which each neuron is connected to all neurons in the previous and following layer. In each layer we can insert a given number of perceptrons, i.e. logistic/other function units which locally discriminate different inputs configuration. Because these units are connected in such a network structure with different layers, when discrimination becomes deeper and deeper, complicated classifications can be computed, far beyond the abilities of other simpler methods, such as logistic regression or support vector machines. Of course, the computational complexity of an ANN increases dramatically with the number of layers and the mean number of units per layer.

In the supervised learning, the ANN is initially trained using a training set in order to find the optimal coefficients to connect the different perceptron units. The most common method used for training is called "back-propagation" [Rummelhart, 1986], aiming at minimizing the mean squared error between prediction and actual values in both classification and regression problems. Once the training is complete, the predictor model, i.e. the network structure plus the coefficients of the units, can be tested and its performance can be analyzed in the test set. Usually ANNs do not have big overfitting problems [Tetko et al., 1995], once a suitable network is chosen, and the training set and test set are homogeneous.

The GP is introduced as a symbolic regression method to find the functional form which fit the available data, by optimizing the combination and composition of functions in a predetermined function set. It is an evolutionary based technique inspired by biological evolution where each individual is a function [Banzhaf et al., 1998]. Once the function base is chosen and ready to span, a set of initial individuals is generated and evaluated on a training set using a fitness function. Depending on the results of the evaluation, the best individuals are kept, and new ones are generated by applying operations like crossover or mutation, then a new generation is obtained. This procedure is performed in several generations till a set of "best fit" individuals are obtained and then tested on the training set. Overfitting can be avoided by limit-

ing the complexity of the individuals, i.e. by do not allow very long functions to enter the population, because such functions have the tendency to adapt very well on the training set, but may not generalizable to the test set in a satisfactory way.

6.2.3 *Data overview*

Most of the supervised learning algorithms used in the context of prediction have a multivariate dataset as input. The dataset can be represented by a $T \times N$ matrix, ordered in such a way that at time t has a set of N attributes $x_1(t)....x_N(t)$ $(t = 1, ..., T)$. The goal is to construct a predictor model that generates reasonable prediction at time $t + \tau$ on the instance y, we call τ as prediction time. The training set is built by choosing an interval of time $[t_i^{train}, t_f^{train}]$ $(t_i^{train}, t_f^{train} \in [1, T])$, and the test set is chosen from $[t_i^{test}, t_f^{test}]$ $(t_i^{test}, t_f^{test} \in [1, T])$. Please note, for El Niño predictions, the condition $t_i^{test} > t_f^{train}$ has to be satisfied, that means the instances in the test set happen after the one in the training set, since we are only interested in a chronological prediction for the El Niño event. However, for the cross-validation of the prediction by regression, no such condition applies.

For El Niño predictions, the instance y in general is the NINO3.4 index, by which the occurrence of an El Niño event can be also determined that a five consecutive 3-month running mean of NINO3.4 index is above the threshold of $+0.5$°C (see `http://www.cpc.ncep.noaa.gov/`). Since the prediction for the occurrence of El Niño events is a classification task, to tackle this task, we take the approach to apply a pure classifier as the predictor model. Therefore we need to transform the instance y from a numeric quantity of NINO3.4 index to a nominal quantity belonging to two possible classes, i.e., 1 stands for the occurrence of an El Niño event and 0 means absence. For the convenience of the computation, the criterion for the occurrence of an El Niño event is a bit loose than the definition above, here we flag an El Niño event when NINO3.4 values are continuously above the threshold of $+0.4$°C for five months.

6.3 RESULTS

6.3.1 *Prediction for El Niño events occurrence*

Although [Ludescher et al., 2014] demonstrate that measures of the CN can be used to anticipate the occurrence of El Niño events, the forecasting scheme (in Fig. 6.2) they provided has its problems. For example, the choice of the decision threshold θ (horizontal line in Fig. 6.2) is subjective and the results are sensitive to the choices of θ values. Moreover, the false alarms (dashed arrows in Fig. 6.2) and the misses (the El Niño events in 2006 and 2009 are not detected in Fig. 6.2) are show the limitations

of the scheme. These deficiencies may be caused by the fact that this forecast scheme is based only on one single measure of the CN.

Here we use the machine learning toolbox to predict the occurrence of El Niño events. We choose the time t from the period of May 1949 - March 2014 with a time interval of 10 days, hence $T = 2365$. Several measures of the same weighted and directed CN as in [Ludescher et al., 2014] (CN reconstruction details can be found in Section 2.2) are used as the attributes ; here eight measures are chosen (with time t as an additional attribute, thus $N = 9$): the averaged values of the maximum correlation $\mathrm{MAX}(C_{ij})$, the minimum correlation $\mathrm{MIN}(C_{ij})$, the maximum delay $\mathrm{MAX}(\Delta t^*)$, the minimum delay $\mathrm{MIN}(\Delta t^*)$, the maximum link weight $\mathrm{MAX}(W_{ij})$, the minimum link weight $\mathrm{MIN}(W_{ij})$, the standard deviation of the correlation $\mathrm{STD}(C_{ij})$, and the mean correlation $\mathrm{MEAN}(C_{ij})$.

The method we choose for the supervised learning is ANN with a 3×3 layer structure (3 neurons per layer). The training set is from May 1949 to June 2001 (80% of T), the test set is from June 2001 to March 2014 (20% of T). The prediction time τ is 12 months which is consistent with [Ludescher et al., 2014]. Fig. 6.3a shows the classification results on the test set, where 1 stands for the occurrence of an El Niño event and 0 means absence. By applying a specific time-series filter, which eliminates the isolated and transient events, and joints the adjacent events, Fig. 6.3b also shows that our forecasting scheme gives accurate alarms 12 months ahead for the El Niño events in 2002, 2006 and 2009, without a false alarm in 2004. Compared with the results in Fig. 6.2 (in the blue dashed rectangle), the machine learning toolbox enables us to give better a prediction for the occurrence of El Niño events when using more measures of the same CN as in [Ludescher et al., 2014].

One advantage of using supervised learning for prediction is that the predictor model is constructed automatically from the training set without subjective decisions like the choice of thresholds. However, if the available data for prediction as well as the amount of instances is limited, (for example, only a few El Niño events occurred between May 1949 and March 2014), the accuracy of the prediction will mostly depend on the length of the training set. This means we need to choose proper proportions of the available data as the training/test set to avoid "under training".

To demonstrate that the current proportion for the test set (20% of T) gives the best performance, we conduct a Receiver Operating Characteristic (ROC)- type analysis by varying the proportion from 16% to 30% of T as the test set. As shown in Fig. 6.4, with a proportion between 16% and 20%, the averaged hit rate $D = 0.90$ and the averaged false-alarm rate $\alpha = 0.10$, for 21% to 25%, we find $D = 0.71$ and $\alpha = 0.29$, and from 26% to 30%, $D = 0.21$ and $\alpha = 0.79$. Thus, to have a higher hit rate and a lower false-alarm rate, the best proportion for the test set is $\leq 20\%$. Of course, we should also maximize the length of the test set to incorporate more El Niño events for testing, and this motivated our choice of 20%.

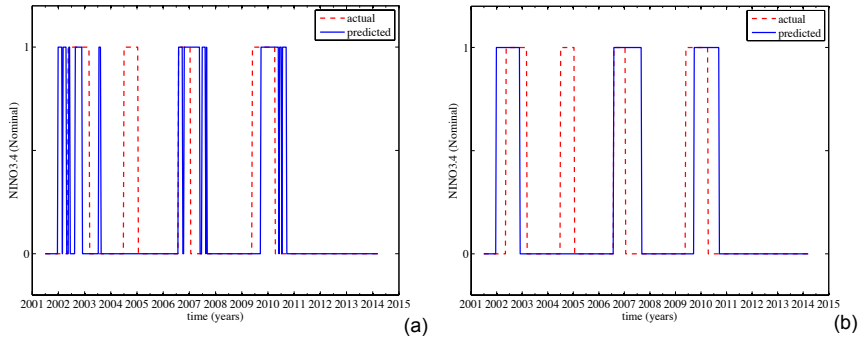

Figure 6.3: *Prediction results on the test set from June 2001 to March 2014 (a) without filtering and (b) with filtering, using an artificial neural network (ANN) with a* 3×3 *layer structure (3 neurons per layer) for the 12 months lead time prediction for the occurrence of El Niño events. The red dashed lines are the actual nominal quantity of the NINO3.4 index (*1 *stands for the occurrence of an El Niño event where NINO3.4 values are continuously above the threshold of* $+0.4°C$ *for five months, and* 0 *for the absence of such an event), and the blue solid lines indicate the predicted one.*

6.3.2 *Prediction for NINO3.4 index development*

Predictions for the development of NINO3.4 index are more difficult than those for the occurrence of El Niño events. For example, consider the CFS version 2 (CFSv2) model developed by the Environmental Modeling Center at National Centers for Environmental Prediction (NCEP). This is a fully coupled model representing the interaction between the Earth's atmosphere, oceans, land and sea ice [Saha et al., 2014]. In August 2014 this model predicted that the NINO3.4 index would go over $+1.0°C$ in October 2014 (Fig. 6.5a) but the actual value in October 2014 was just around $+0.5°C$ (Fig. 6.5b). Hence even for short term predictions (up to few months) a good skill of the NINO3.4 index development is still hard to achieve by this model.

The short-term development of NINO3.4 index is strongly related to the stability of the Pacific background state and the occurrence of westerly wind bursts (WWBs) near the dateline. Using the SST data, in **chapter 5**, we found that the stability of the Pacific climate can be measured by the skewness of the degree distribution, indicated by S_d, of a Pearson Correlation Climate Network (PCCN) network reconstructed from these observations. As a WWB measure, we use the time series of the second principal component (PC2) of the wind stress residual as determined in **chapter 5**.

Next, we use the machine learning toolbox to investigate the importance of S_d and PC2 for the El Niño development by supervised learning regression. The attributes

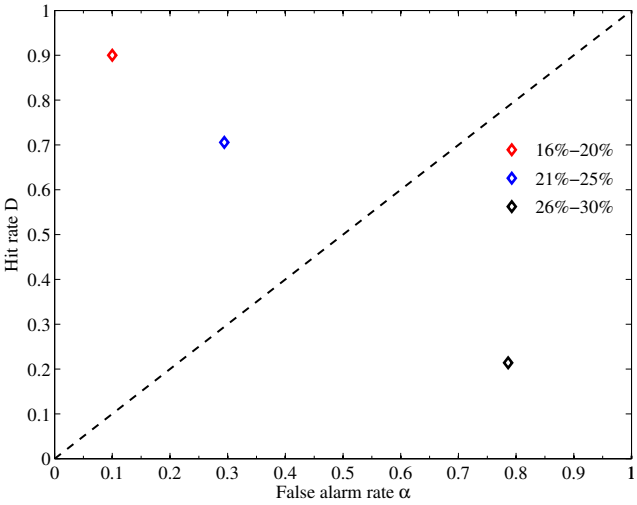

Figure 6.4: *The Receiver Operating Characteristic (ROC)- type analysis on the prediction accuracy. The red dot shows the averaged hit rate D and false alarm rate α by taking* 16%−20% *of the total available data as the test set, the blue dot shows the ones when taking* 21%−25% *and the black dot shows the ones when taking* 26%−30%*.*

are therefore the background stability index $x_1 = S_d$, the westerly wind burst measure $x_2 =$ PC2 and the time $x_3 = t$ from November 1961 to October 2014 with a time interval of one month; hence $T = 636$ and $N = 3$. The training set is from November 1961 to April 2004 (80% of T) and the test set is from May 2004 to October 2014 (20% of T). The quality of the predicted results in the test set is measured by the normalized root mean squared error (NRMSE) between the actual time series of NINO3.4 index $y^A(t)$ and the predicted one $y^P(t)$, defined as

$$NRMSE(y^A, y^P) = \frac{1}{\max_k(y^A, y^P) - \min_k(y^A, y^P)} \sqrt{\frac{\sum\limits_{t_i^{test} \le t \le t_f^{test}} (y^A(t) - y^P(t))^2}{n}}, \tag{6.1}$$

where n is the number of points in the time series.

We first employ an ANN with a 2×1 layer structure (2 neurons in the first layer and 1 neuron in the second one) to do the regression. Since we do not know the optimal prediction time τ which would give a reasonable prediction $y(t+\tau)$ at time $t+\tau$, we vary τ from 1 month up to 12 months. Fig. 6.6 shows the regression results on

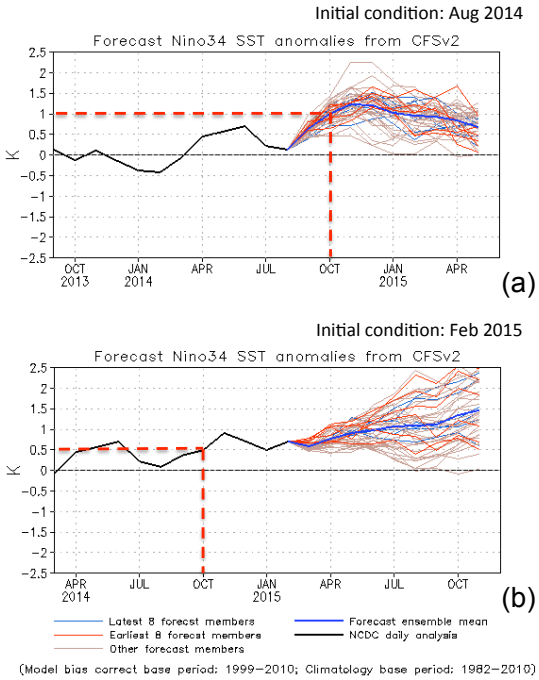

Figure 6.5: *Predicted and observed NINO3.4 index from the NCEP Coupled Forecast System Model (CFSv2) released by Climate Diagnostics Bulletin (available via* `http://www.cpc.ncep.noaa.gov/products/CDB/`*) in (a) August 2014 and (b) February 2015. The forecasts consist of a 40 forecast member ensemble. The ensemble mean of all 40 forecast members is shown by the blue line while the individual members are shown by thin lines. The observed NINO3.4 index is indicated by the black curve. The red dashed lines indicate the values of the NINO3.4 index in October 2014.*

the test set for the 2-4 months ahead NINO3.4 forecasts. The best prediction is given at $\tau = 3$ months with the smallest value of NRMSE=0.18 (Fig. 6.6b).

To test the robustness of the regression result of the three months lead time NINO3.4 index forecast (Fig. 6.6b), we perform a series of cross-validations by keeping certain percentage splits between training set and test set (70-30, 75-25, 80-20, and 85-15), but randomly choosing 200 initial times of the test set t_i^{test} from November 1961 to October 2014 for each percentage split. From Fig. 6.7 one can see that the peak values of the NRMSE remains near 0.17, independent of the choices of the

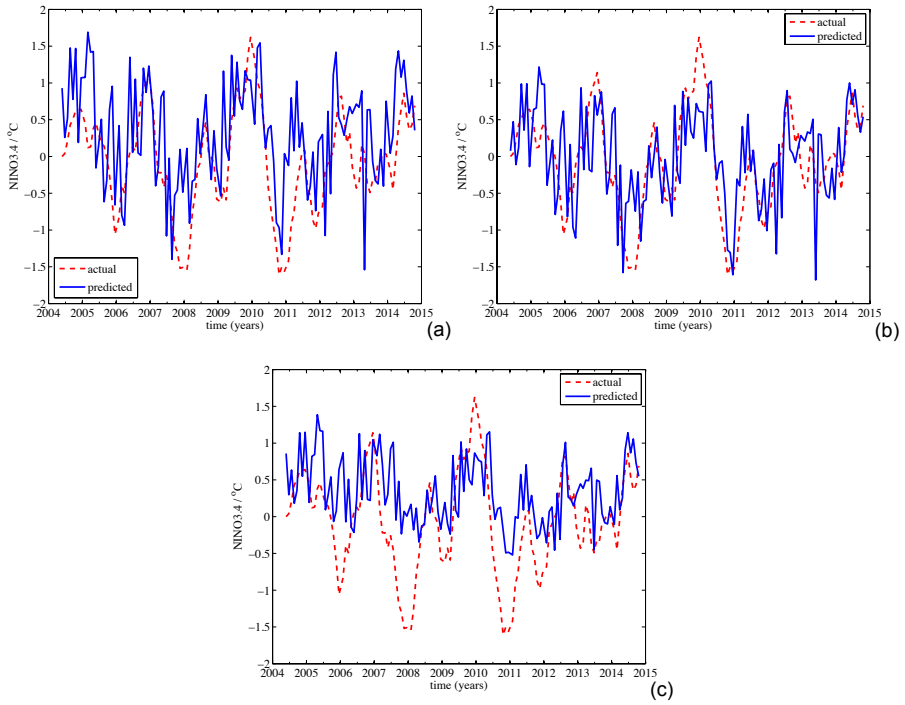

Figure 6.6: *Regression results on the test set from May 2004 to October 2014 using an ANN with a* 2×1 *layer structure (2 neurons in the first layer and 1 neuron in the second one) for the prediction of the NINO3.4 index with a lead time of (a) 2 months (NRMSE*=0.23*), (b) 3 months (NRMSE*=0.18*), and (c) 4 months (NRMSE*=0.22*). The red dashed lines are the actual values of NINO3.4 index, and the blue solid lines indicate the predicted ones.*

percentage splits and t_i^{test}. Therefore the regression result in Fig. 6.6b is considered robust.

Due to the irregular behavior of the PC2 representing the WWBs (cf. Fig. 5.9), the predicted NINO3.4 indices in Fig. 6.6 show more fluctuation than the actual one. When a 3-month running mean is applied to the predicted NINO3.4 index (three months lead time, Fig. 6.6b) as well as the actual one, the forecast has a better skill (NRMSE=0.14) as shown in Fig. 6.8a. To further demonstrate that the result in Fig. 6.8a is robust and independent of the choices of ANN layer structures and the methods for the supervised learning, we perform the same regression task with an ensemble of 49 ANNs with different binary layer structures and up to 7 neurons per layer and an ensemble of 50 GP runs. The averaged result of the best 10 ANNs

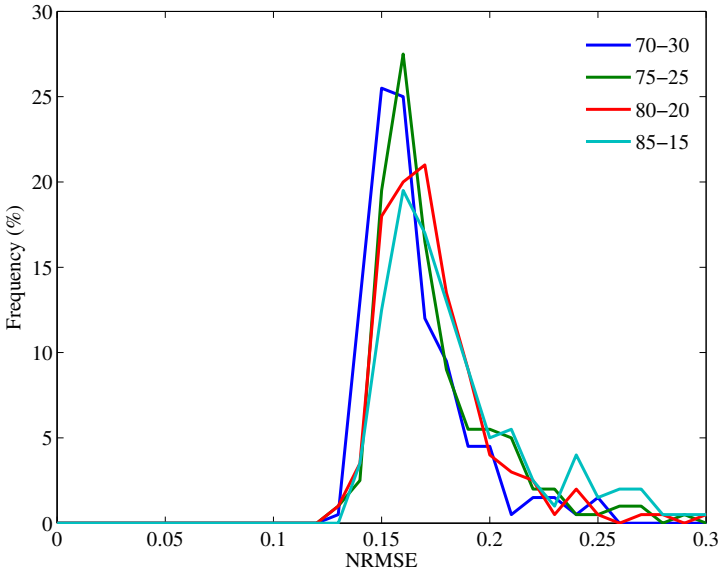

Figure 6.7: *Cross-validation results of NINO3.4 index forecast on the test set by keeping certain percentage splits between training set and test set (70-30, 75-25, 80-20, and 85-15), but randomly choosing 200 initial times of the test set* t_i^{test} *from November 1961 to October 2014 for each percentage split. The blue dashed curve is the NRMSE distribution of 70-30 split (70% of* T *as the training sets and 30% of* T *as test sets), the green solid line for a 75-25 split, the red solid curve for a 80-20 split and the cyan solid curve for a 85-15 split.*

(with lower NRMSE values) is shown in Fig. 6.8b with NRMSE=0.15. The averaged result of the best 10 GP runs (with lower NRMSE values) is shown in Fig. 6.8c with NRMSE=0.17, which are both similar to the one obtained by the ANN with a 2×1 layer structure in Fig. 6.8a.

6.3.3 *Prediction for ENSO Variability in 2014*

In the previous sections we have seen that by using the measures of the CNs from [Ludescher et al., 2014] and **chapter 5**, the machine learning toolbox can give robust predictions on the occurrence of El Niño events one year ahead and the development of NINO3.4 index with a lead time of three months, respectively. We now apply these techniques to the occurrence and development of the situation in 2014.

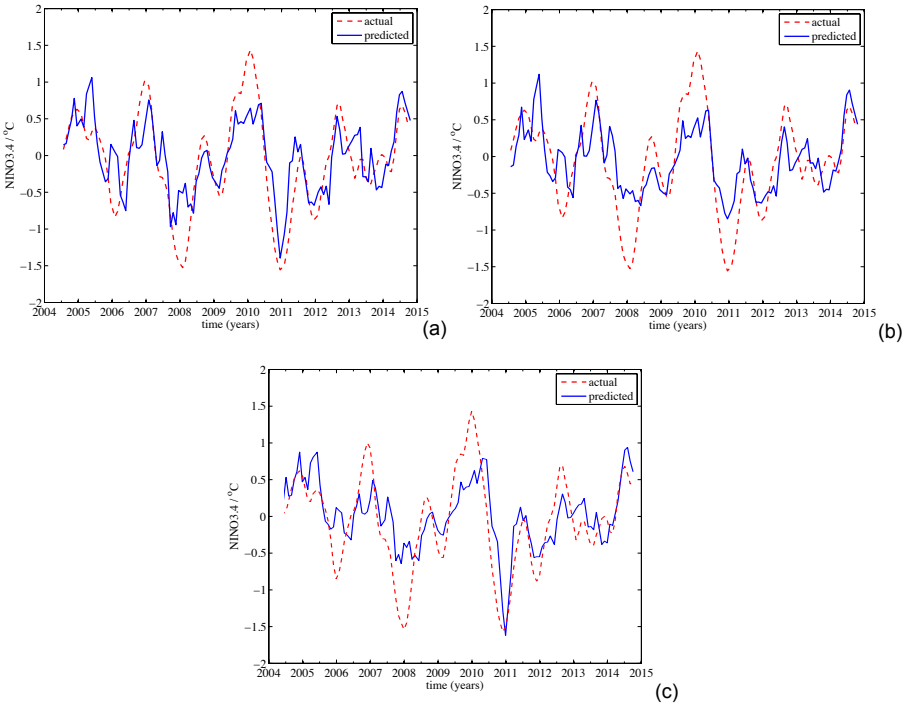

Figure 6.8: *Results for a 3-month running mean regression on the test set from May 2004 to October 2014 using (a) an ANN with a* 2×1 *layer structure (2 neurons in the first layer and 1 neuron in the second one, NRMSE*=0.14*), (b) an ensemble of 49 ANNs with different binary layer structures and up to 7 neurons per layer (only the ensemble mean of the best 10 is showed, NRMSE*=0.15*) and (c) an ensemble of genetic programmings (only the ensemble mean of the best 10 is showed, NRMSE*=0.17*) for the three months ahead prediction for the development of the NINO3.4 index. The red dashed curves are the actual values of NINO3.4 index, and the blue solid curves indicate the predicted ones.*

First, we consider the occurrence of an El Niño event up to March 2015, by using the same data used in Section 6.3.1 till March 2014. The prediction results on ENSO variability in 2014 are shown in Fig. 6.9a, by employing an ensemble of 36 ANNs with different binary layer structures and up to 6 neurons per layer. Like the event in 2012 in Fig. 6.3b, our forecast scheme tends to ignore the ENSO-neutral favored events or the weak El Niño events. Hence, no El Niño event between January 2014 to March 2015 is predicted one year ahead (Fig. 6.9a).

Second, we consider the development of the NINO3.4 index from January 2014 till January 2015 using the same data used in Section 6.3.2 till October 2014. The skill of the predicted NINO3.4 index over 2014 with a lead time of three months (Fig. 6.9b) is quite reasonable (NRMSE=0.19) compared with the one given by CFSv2 model in Fig. 6.5.

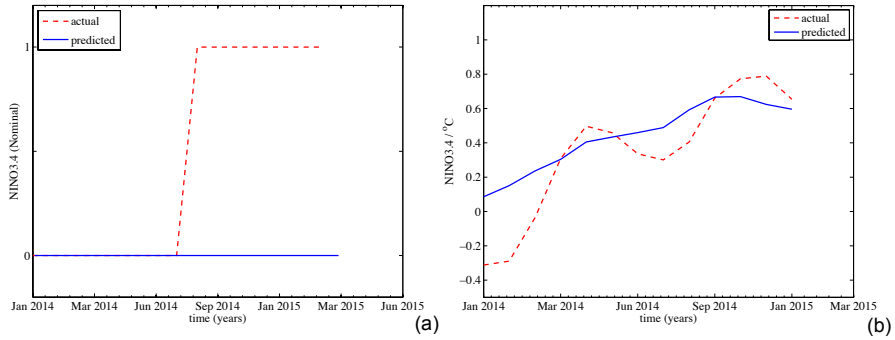

Figure 6.9: *Prediction results on ENSO variability in 2014 using an ensemble of 36 ANNs with different binary layer structures and up to 6 neurons per layer. (a) The occurrence of the El Niño event given one year ahead, and (b) the development of NINO3.4 index with a three months a lead time (only the ensemble mean is shown, NRMSE=0.19). The red dashed lines are the actual nominal quantity/actual values of NINO3.4 index, and the blue solid lines indicate the predicted ones.*

6.4 DISCUSSION

Using machine learning techniques with the measures from reconstructed CN, we have provided novel prediction schemes for the occurrence of an El Niño event (with a lead time of one year) and for the development of the NINO3.4 index (with a lead time of three months).

By using measures of a directed and weighted CN [Ludescher et al., 2014] and supervised learning classification, we developed a forecast scheme that apparently does

not suffer from the "spring predictability barrier" [Goddard et al., 2001] to predict the occurrence of an El Niño event one year ahead. In addition, by using measures of a PCCN that monitor the stability of the Pacific climate state (in **chapter 5**) and a measure of the atmospheric wind-stress noise in combination with supervised learning regression, we provided reasonable forecasts of the development of the NINO3.4 index three months ahead.

Besides handing multivariate data from CNs and other sources, another advantage of using this machine learning toolbox for climate variability prediction is that the development of predictor models is dynamic and data-driven [Bishop et al., 2006]. Therefore, the prediction schemes can represent the nonlinear relationships among the attributes and give objective prediction. For example, in the forecast scheme proposed by [Ludescher et al., 2014], the prediction may be sensitive to the choice of the decision threshold θ (horizontal line in Fig. 6.2), while based on the supervised learning method our forecast scheme does not have this problem.

The machine learning toolbox can also be used to test hypotheses regarding important factors for ENSO variability. For example in **chapter 5**, we indicated that El Niño variability is strongly determined by the stability of the Pacific climate (as measured by the S_d index) and the WWBs (as measured through the PC2). Fig. 6.8 shows that by combining these two factors, reasonable NINO3.4 index forecasts can be given three months ahead. A lead time of three months of course is too short to make this forecast scheme outcompete existing ones. However, comparing these forecast results with those from much more sophisticated models like the CFSv2 model in Fig. 6.5, shows that indeed the quantities S_d and PC2 are important factors in the development of ENSO.

Finally, building on the success of complex network approaches to investigate aspects of climate variability, the machine learning toolbox provides an innovative and convenient way to predict the occurrence and development of El Niño events. This toolbox can also be directly applied to the prediction of other climate variability phenomena and can be also extended to assess the importance specific processes in these phenomena.

7

SUMMARY AND DISCUSSION

The main goal of this thesis was to improve the understanding of climate variability through a complex network approach. Three specific phenomena of climate variability were studied in this thesis: the collapse of the Atlantic Meridional Overturning Circulation (MOC), the multidecadal variability associated with the Atlantic Multidecadal Oscillation (AMO), and the interannual variations of El Niño-Southern Oscillation (ENSO). All these phenomena are caused by critical behavior, where climate feedbacks amplify perturbations, leading to transitions in behavior when critical boundaries are crossed. Our approach was to study these transition phenomena first in idealized climate models, then develop early warning indicators based on Climate Network (CN) in these models and subsequently apply them to observational data and/or general circulation model (GCM) output.

The main results of this thesis are summarized as point-by-point answers to the central questions posed in **chapter 1**:

(i) Can network based indicators be developed that provide useful "peaky" early warning indicators of a collapse of the Atlantic MOC? (chapter 3)

The Atlantic MOC is a crucial part of the climate system because of its associated northward heat transport [Ganachaud and Wunsch, 2000; Johns et al., 2011]. As a consequence of greenhouse gas emissions, the MOC may rapidly (within a few decades) change in strength when the freshwater balance of the northern North Atlantic changes. This transition behavior is caused by the salt-advection feedback and associated with a saddle-node bifurcation. The main goal was to develop early warning indicators for a potential collapse of Atlantic MOC preferably based on relatively short time series.

Using techniques of complex network theory, we have provided a novel indicator of the MOC collapse based on spatial correlations that efficiently monitors spatial changes in deep ocean circulation. In an idealized ocean model for which the saddle-node bifurcation could be explicitly computed, we showed that the kurtosis value of the normalized degree distribution K_d of the CN is a "peaky" indicator when the

bifurcation is approached. The "peakyness"' of this indicator could be explained by the increased dominance of the first empirical orthogonal function (EOF) in the variance of the solution in a large part of the domain.

We applied the indicator K_d to the data from the coupled atmosphere-ocean GCM - FAMOUS model [Hawkins et al., 2011]. Our results showed that a strong early warning signal can be detected at least 100 years before the occurrence of the MOC collapse. Our results also indicate that an increase in spatial resolution of the MOC observations (i.e., at more sections), especially in the midlatitude North and South Atlantic ocean, can improve early detection using this indicator, because the spatial coherence arising near the transition is better captured.

The strength of the Atlantic MOC is currently actively monitored [Cunningham et al., 2007] by the RAPID-MOCHA array (see Fig. 1.7). Up to now, there is about 10 years of data on the MOC, however, the temporal extend of the time series proceeds very slowly. Thus, the time series of the MOC strength derived from the RAPID-MOCHA program are certainly too short to be able to apply the early warning indicator K_d to determine whether the recent downward trend in the observed MOC strength at 26°N [Smeed et al., 2013] is the start of a collapse (see Fig. 1.7). Such MOC behavior may just be related to natural variability such as that associated with the AMO [Kerr, 2000; Knight et al., 2005].

(ii) Can network theory be used to identify patterns of low-frequency climate variability, such as the AMO, using the relatively short instrumental record? (chapter 4)

The thermal Rossby mode mechanism [Frankcombe et al., 2010] is a promising candidate to explain the multidecadal (20-30 years) climate variability in the North Atlantic. One of the main characteristics of this mechanism is the westward propagation of temperature anomalies. However, indications for this westward propagation are difficult to distinguish from sea surface temperature (SST) observations because many other processes affect SST in the North Atlantic [Booth et al., 2012; Sutton and Hodson, 2005b].

We reconstructed CNs by using a linear Pearson correlation measure (resulting in Pearson Correlation Climate Network (PCCN)s) and a nonlinear mutual information measure (resulting in Mutual Information Climate Network (MICN)s) of spatial correlations between SST variations from both idealized model data (with only the thermal Rossby mode) and the observations. We compared the relative degree field of the CNs from the observations with the one of CNs from the idealized model results, and quantitatively measure the similarity between these network properties by the Hamming distance. We found that the MICNs are better in capturing the main features of

propagating patterns from the noisy SST data than PCCNs, and that westward propagation of multidecadal SST anomalies indeed seems to occur in the North Atlantic.

The SST anomaly field is thought to result from advective contributions as well as from a noisy surface heat flux field. In addition, the growth rate of the thermal Rossby mode is known to depend on the time-dependent background state [Dijkstra et al., 2008]. This introduces nonlinear dependencies in the dynamics of this low-frequency climate variability which may be the reason that a nonlinear mutual information measure is better suited to identify the patterns than a linear Pearson correlation measure.

Although a good correspondence between observations and idealized model data can be clearly seen by reconstructing MICNs, the differences between network properties of the MICNs may occur due to (i) additional processes affecting SST variability, (ii) the pre-treatment of the observations and (iii) the effect of the continental boundaries (in the observations). A limitation of the methodology of CN is that it is difficult to determine where these differences originate from.

(iii) Does network theory provide a possibility to develop indicators of the stability of the Pacific climate, important for the amplitude and development of ENSO? (chapter 5)

The Zebiak and Cane (ZC) model [Zebiak and Cane, 1987] captures the basic processes of ENSO and has provided the recharge-discharge oscillator view of ENSO. In this view, where positive Bjerknes feedbacks are responsible for the amplification of SST anomalies and ocean adjustment provides a negative delayed feedback [Jin, 1997; Neelin et al., 1998]. The strength of the feedbacks is represented by a coupling strength; when this quantity exceeds a critical value, the background climate becomes unstable through a Hopf bifurcation. When noise is included in this system, the oscillatory behaviour can be excited by additive noise when the system is still in the subcritical regime. Hence, both noise, especially westerly wind bursts (WWBs)[Lian et al., 2014; Menkes et al., 2014], and the stability of the Pacific climate are important for the development of ENSO. One successful quantity to analyse the stability of the Pacific climate is the Bjerknes stability (BJ) index [Kim and Jin, 2011a;b; Kim et al., 2014], but its evaluation is severely constrained by data availability. Thus, a more practical stability index (than the BJ index) is urgently needed.

We have developed a novel index S_d, the skewness of the degree distribution of a CN, which provides a simple (only requires SST data) and adequate measure of the stability of the Pacific climate. We tested the S_d index in the ZC model in which a stochastic Hopf bifurcation occurs [Roulston and Neelin, 2000]. When the critical transition is approached, the spatial pattern of the SST anomalies is more and more controlled by the ENSO mode, leading to large-scale coherence which is efficiently

measured by the CN based S_d index. The S_d index is therefore anti-correlated with the variance of the NINO3.4 index under a fixed noise amplitude. Hence, a high (low) value of S_d indicates a relatively high (low) stability of the background state. Strong support that S_d monitors the stability of the background state comes from the anti-correlated behavior (cf. Fig. 5.8) with the BJ index in an ensemble of CMIP5 models [Kim et al., 2014].

When the S_d index applied to the observations, the results clearly shows the problems which are faced with El Niño prediction. The WWBs is important to induce SST anomalies, but whether an El Niño and La Niña will develop also depends on the Pacific climate stability that varies on decadal time scales. For example, one can have an El Niño when noise is large even when the background stability is relatively high (as in 1982), and also an El Niño when background stability is low (such as in 1997). This also nicely explains why there was no big El Niño developed in late 2014 as most models predicted. The S_d index already increased in the beginning of the year 2014, indicating that the Pacific climate became more stable. This is consistent with the fact that although large subsurface temperature anomalies developed in March 2014, there was no growth of SST anomalies because the thermocline feedback was weak and no strong El Niño event could develop.

(iv) Can network-based information be used to enhance the skill of ENSO predictions? (chapter 6)

The ENSO phenomenon is a dominant mode of interannual climate variability with large impacts on nature and society. However, a good skill of present-day dynamical and statistical model predictions of El Niño occurrences is limited to a few months ahead. Building on the success of complex network approaches to investigate aspects of climate variability, we have provided an approach combining machine learning and network reconstruction resulting in new schemes for El Niño prediction.

By using measures of a directed and weighted CN [Ludescher et al., 2014] and the supervised learning classification, we presented a forecast scheme that apparently does not suffer from the "spring predictability barrier" [Goddard et al., 2001] to predict the occurrence of an El Niño event one year ahead. In addition, by using measures of an undirected and unweighted CNs that monitor the stability of the Pacific climate state (in **chapter 5**) and a measure of the atmospheric wind-stress noise in combination with the supervised learning regression, we provided forecasts of the development of the NINO3.4 index three months ahead.

This machine learning approach can also be used to test hypotheses regarding important factors for ENSO variability. For example in **chapter 5**, we indicated that El Niño variability is strongly determined by the stability of the Pacific climate (as measured by the S_d index) and the variability of the atmospheric noise. Our results

show that by combining these two factors, reasonable NINO3.4 index forecasts can be given three months ahead. A lead time of three months of course is too short to make this forecast scheme outcompete existing ones. However, comparing these forecast results with those from much more sophisticated models like the CFSv2 model in Fig. 6.5, shows that indeed the quantities S_d and noise are important factors in the development of ENSO.

This approach can also be directly applied to the prediction of other climate variability phenomena and can be also extended to assess the importance of specific processes in these phenomena.

To conclude, each of the results in the **chapters 3-6** in this thesis has given an example where the use of the techniques from complex network theory has resulted in new and useful information on the behavior of aspects of climate variability. This definitely motivates to use these techniques in the future in other areas of climate research.

BIBLIOGRAPHY

N. Andronova and M. Schlesinger. Causes of global temperature changes during the 19th and 20th centuries. *Geophysical Research Letters*, 27:2137–2140, 2000.

K. E. Atkinson. *An Introduction to Numerical Analysis*. John Wiley and Sons, 1976.

W. Banzhaf, P. Nordin, R. E. Keller, and F. D. Francone. *Genetic programming: an introduction*, volume 1. Morgan Kaufmann San Francisco, 1998.

A.-L. Barabási and R. Albert. Emergence of scaling in random networks. *science*, 286: 509–512, 1999.

A.-L. Barabási et al. Scale-free networks: a decade and beyond. *science*, 325:412, 2009.

A. D. Barnosky, E. A. Hadly, J. Bascompte, E. L. Berlow, J. H. Brown, M. Fortelius, W. M. Getz, J. Harte, A. Hastings, P. A. Marquet, N. D. Martinez, A. Mooers, P. Roopnarine, G. Vermeij, J. W. Williams, R. Gillespie, J. Kitzes, C. Marshall, N. Matzke, D. P. Mindell, E. Revilla, and A. B. Smith. Approaching a state shift in Earth's biosphere. *Nature*, 486:52–58, 2012.

L. Bejarano and F.-F. Jin. Coexistence of equatorial coupled modes of ENSO. *Journal of Climate*, 21:3051–3067, 2008.

S. Bialonski, M. Wendler, and K. Lehnertz. Unraveling Spurious Properties of Interaction Networks with Tailored Random Networks. *PLoS ONE*, 6:e22826, 2011.

C. M. Bishop et al. *Pattern recognition and machine learning*, volume 4. springer New York, 2006.

G. Bond, W. Broecker, S. Johnsen, J. McManus, L. Labeyrie, J. Jouzel, and G. Bonani. Correlations between climate records from north atlantic sediments and greenland ice. *Nature*, pages 143–147, 1993.

B. B. Booth, N. J. Dunstone, P. R. Halloran, T. Andrews, and N. Bellouin. Aerosols implicated as a prime driver of twentieth-century North Atlantic climate variability. *Nature*, 484:228–232, 2012.

F. O. Bryan. High-latitude salinity effects and interhemispheric thermohaline circulations. *Nature*, 323:301–304, 1986.

G. Burgers. The El Niño Stochastic Oscillator. *Clim. Dyn.*, 15:352–375, 1999.

W. Cai and T. Cowan. La Niña modoki impacts australia autumn rainfall variability. *Geophysical Research Letters*, 36, 2009.

D. Chen, M. A. Cane, A. Kaplan, S. E. Zebiak, and D. Huang. Predictability of El Niño over the past 148 years. *Nature*, 428:733–736, 2004.

M. Collins, R. Knutti, J. Arblaster, J.-L. Dufresne, T. Fichefet, P. Friedlingstein, X. Gao, W. Gutowski, T. Johns, G. Krinner, M. Shongwe, C. Tebaldi, A. Weaver, and M. Wehner. Long-term Climate Change: Projections, Commitments and Irreversibility. In T. Stocker, D. Qin, G.-K. Plattner, M. Tignor, S. Allen, J. Boschung, A. Nauels, Y. Xia, V. Bex, and P. Midgley, editors, *Climate Change 2013: The Physical Science Basis. Contribution of Working Group I to the Fifth Assessment Report of the Intergovernmental Panel on Climate Change*, pages 1029–1136. Cambridge: University of Cambridge Press Syndicate., UK, 2013.

C. R. Committee et al. *Natural climate variability on decade-to-century time scales*. National Academies Press, 1996.

S. Cunningham, T. Kanzow, D. Rayner, M. Baringer, W. Johns, J. Marotzke, H. Longworth, E. Grant, J. Hirschi, L. Beal, et al. Temporal Variability of the Atlantic Meridional Overturning Circulation at 26.5° N. *Science*, 317:935, 2007.

V. Dakos, S. Kéfi, M. Rietkerk, E. H. van Nes, and M. Scheffer. Slowing down in spatially patterned ecosystems at the brink of collapse. *The American Naturalist*, 177:154–166, 2011.

A. De Niet, F. Wubs, A. T. van Scheltinga, and H. A. Dijkstra. A tailored solver for bifurcation analysis of ocean-climate models. *Journal of Computational Physics*, 227:654–679, 2007.

T. L. Delworth and M. E. Mann. Observed and simulated multidecadal variability in the Northern Hemisphere. *Clim. Dyn.*, 16:661–676, 2000a.

T. Delworth and M. Mann. Observed and simulated multidecadal variability in the Northern Hemisphere. *Climate Dynamics*, 16:661–676, 2000b.

M. Den Toom, H. A. Dijkstra, and F. W. Wubs. Spurious multiple equilibria introduced by convective adjustment. *Ocean Modelling*, 38:126–137, 2011.

C. Deser and M. L. Blackmon. Surface climate variations over the North Atlantic ocean during winter: 1900–1989. *J Climate*, 6:1743–1753, 1993.

H. A. Dijkstra and M. Ghil. Low-frequency variability of the large-scale ocean circulation: A dynamical systems approach. *Rev. Geophys.*, 2005.

H. A. Dijkstra and J. Neelin. Coupled ocean-atmosphere models and the tropical climatology. II: Why the cold tongue is in the east. *J Climate*, 8:1343–1359, 1995.

H. A. Dijkstra, L. M. Frankcombe, and A. S. Von der Heydt. A stochastic dynamical systems view of the Atlantic Multidecadal Oscillation. *Philosophical Transactions of the Royal Society A*, 366:2543–2558, 2008.

H. A. Dijkstra. *Nonlinear climate dynamics*. Cambridge University Press, 2013.

R. Donangelo, H. Fort, V. Dakos, M. Scheffer, and E. Van Nes. Early warnings for catastrophic shifts in ecosystems: comparison between spatial and temporal indicators. *International Journal of Bifurcation and Chaos*, 20:315–321, 2010.

J. F. Donges, Y. Zou, N. Marwan, and J. Kurths. Complex networks in climate dynamics. *The European Physical Journal Special Topics*, 174:157–179, 2009a.

J. F. Donges, Y. Zou, N. Marwan, and J. Kurths. The backbone of the climate network. *EPL (Europhysics Letters)*, 87:48007, 2009b.

J. F. Donges. *Functional network macroscopes for probing past and present Earth system dynamics*. PhD thesis, Humboldt-Universität zu Berlin, Mathematisch-Naturwissenschaftliche Fakultät I, 2013.

R. V. Donner, Y. Zou, and J. F. Donges. Recurrence networks—a novel paradigm for nonlinear time series analysis. *New Journal of . . .* , 2010.

R. V. Donner, M. Small, J. F. Donges, N. Marwan, Y. Zou, R. Xiang, and J. Kurths. Recurrence-based time series analysis by means of complex network methods. *International Journal of Bifurcation and Chaos*, 21:1019–1046, 2011.

S. N. Dorogovtsev and J. F. Mendes. *Evolution of networks: From biological nets to the Internet and WWW*. Oxford University Press, 2013.

W. Duan and C. Wei. The "spring predictability barrier" for ENSO predictions and its possible mechanism: results from a fully coupled model. *International Journal of Climatology*, 33:1280–1292, 2013.

I. Eisenman, L. Yu, and E. Tziperman. Westerly Wind Bursts: ENSO's Tail Rather than the Dog? *J. Climate*, 18:5224–3238, 2005.

D. B. Enfield, A. M. Mestas-Nunes, and P. Trimble. The Atlantic multidecadal oscillation and its relation to rainfall and river flows in the continental US. *Geophys. Res. Letters*, 28:2077–2080, 2001a.

D. Enfield, A. Mestas-Nunez, P. Trimble, et al. The atlantic multidecadal oscillation and its relation to rainfall and river flows in the continental u. s. *Geophysical Research Letters*, 28:2077–2080, 2001b.

P. Erdös and A. Réyi. On random graphs i. *Publ. Math. Debrecen*, 6:290–297, 1959.

A. J. Faller. An average correlation coefficient. *Journal of Applied Meteorology*, 20: 203–205, 1981.

A. V. Fedorov and S. G. Philander. Is El Niño Changing? *Science*, 288:1997–2002, 2000.

A. Fedorov, S. Harper, S. Philander, B. Winter, and A. Wittenberg. How predictable is El Niño? *Bulletin of the American Meteorological Society*, 84:911–919, 2003.

Q. Y. Feng, J. P. Viebahn, and H. A. Dijkstra. Deep ocean early warning signals of an Atlantic MOC collapse. *Geophysical Research Letters*, 41: doi:10.1002/2014GL061019, 2014.

S. Feng and Q. Hu. How the North Atlantic Multidecadal Oscillation may have influenced the Indian summer monsoon during the past two millennia. *Geophysical Research Letters*, 35:L01707, 2008.

R. A. Fisher. Frequency distribution of the values of the correlation coefficient in samples from an indefinitely large population. *Biometrika*, pages 507–521, 1915.

L. M. Frankcombe and H. A. Dijkstra. Coherent multidecadal variability in North Atlantic sea level. *Geophysical Research Letters*, 36:L15604, 2009.

L. M. Frankcombe, A. S. Von Der Heydt, and H. A. Dijkstra. North Atlantic multidecadal climate variability: an investigation of dominant time scales and processes. *Journal of Climate*, 23:3626–3638, 2010.

L. Frankcombe, H. Dijkstra, and A. von der Heydt. Sub-surface signatures of the Atlantic Multidecadal Oscillation. *Geophys. Res. Lett*, 35:L19602, 2008.

A. Ganachaud and C. Wunsch. Improved estimates of global ocean circulation, heat transport and mixing from hydrographic data. *Nature*, 408:453–457, 2000.

A. E. Gill. Some simple solutions for heat induced tropical circulation. *Quart. J. Roy. Meteor. Soc.*, 106:447–462, 1980.

L. Goddard, S. J. Mason, S. E. Zebiak, C. F. Ropelewski, R. Basher, and M. A. Cane. Current approaches to seasonal to interannual climate predictions. *International Journal of Climatology*, 21:1111–1152, 2001.

A. Gozolchiani, S. Havlin, and K. Yamasaki. Emergence of El Niño as an Autonomous Component in the Climate Network. *Physical Review Letters*, 107:148501, 2011.

W. M. Gray, J. D. Sheaffer, and C. W. Landsea. Variability of Atlantic Hurricane activity. In H. Diaz and D. Pulwarthy, editors, *Hurricanes*, pages 15–53. Springer, Germany, 1997.

O. C. Guez, A. Gozolchiani, and S. Havlin. Influence of autocorrelation on the topology of the climate network. *Physical Review E*, 90:062814, 2014.

K. H. Hamed and A. R. Rao. A modified mann-kendall trend test for autocorrelated data. *Journal of Hydrology*, 204:182–196, 1998.

R. W. Hamming. Error detecting and error correcting codes. *Bell Syst. Tech. J.*, 26: 147–157, 1950.

E. Hawkins, R. S. Smith, L. C. Allison, J. M. Gregory, T. J. Woollings, H. Pohlmann, and B. De Cuevas. Bistability of the Atlantic overturning circulation in a global climate model and links to ocean freshwater transport. *Geophysical Research Letters*, 38: L10605, 2011.

R. Hegger, H. Kantz, and T. Schreiber. Practical implementation of nonlinear time series methods: The tisean package. *Chaos: An Interdisciplinary Journal of Nonlinear Science*, 9:413–435, 1999.

H. Held and T. Kleinen. Detection of climate system bifurcations by degenerate fingerprinting. *Geophysical Research Letters*, 31:L23207, 2004.

S. E. Huisman, M. den Toom, H. A. Dijkstra, and S. Drijfhout. An Indicator of the Multiple Equilibria Regime of the Atlantic Meridional Overturning Circulation. *Journal Of Physical Oceanography*, 40:551–567, 2010.

H. Ihshaish, A. Tantet, J. Dijkzeul, and H. Dijkstra. Par@ graph–a parallel toolbox for the construction and analysis of large complex climate networks. *Geoscientific Model Development Discussions*, 8:319–349, 2015.

F.-F. Jin. An equatorial recharge paradigm for ENSO. II: A stripped-down coupled model. *J. Atmos. Sci.*, 54:830–8847, 1997.

F.-F. Jin, J. Neelin, and M. Ghil. El Niño/Southern Oscillation and the annual cycle: Subharmonic frequency-locking and aperiodicity. *Physica D-Nonlinear Phenomena*, 98:442–465, 1996.

F.-F. Jin, S. T. Kim, and L. Bejarano. A coupled-stability index for ENSO. *Geophysical Research Letters*, 33, 2006.

W. Johns, M. Baringer, and L. Beal. Continuous, array-based estimates of Atlantic Ocean heat transport at 26.5 N. *Journal Of Climate*, 24:2429–2449, 2011.

J. H. Jungclaus, H. Haak, M. Latif, and U. Mikolajewicz. Arctic-North Atlantic Interactions and Multidecadal Variability of the meridional overturning circulation. *J Climate*, 18:4013–4031, 2005.

E. Kalnay and coauthors. The NCEP/NCAR reanalysis 40-year project. Bull. American Meteorological Society, 1996.

H.-Y. Kao and J.-Y. Yu. Contrasting eastern-pacific and central-pacific types of ENSO. *Journal of Climate*, 22:615–632, 2009.

R. W. Katz. Sir Gilbert Walker and a connection between El Niño and statistics. *Statistical Science*, pages 97–112, 2002.

H. B. Keller. Numerical solution of bifurcation and nonlinear eigenvalue problems. In P. H. Rabinowitz, editor, *Applications of Bifurcation Theory*. Academic Press, New York, U.S.A., 1977.

R. A. Kerr. A North Atlantic climate pacemaker for the centuries. *Science*, 288:1984–1986, 2000.

H.-M. Kim, P. J. Webster, and J. A. Curry. Impact of shifting patterns of pacific ocean warming on north atlantic tropical cyclones. *Science*, 325:77–80, 2009.

J. Kim and T. Wilhelm. What is a complex graph? *Physica A: Statistical Mechanics and its Applications*, 387:2637–2652, 2008.

S. T. Kim and F.-F. Jin. An ENSO Stability Analysis. Part I: Results from a Hybrid Coupled Model. *Climate Dynamics*, 36:1593–1607, 2011a.

S. T. Kim and F.-F. Jin. An ENSO stability analysis. part ii: Results from the twentieth and twenty-first century simulations of the cmip3 models. *Climate Dynamics*, 36: 1609–1627, 2011b.

S. T. Kim, W. Cai, F.-F. Jin, A. Santoso, L. Wu, E. Guilyardi, and S.-I. An. Response of El Nino sea surface temperature variability to greenhouse warming. *Nature Climate Change*, 4:786–790, 2014.

J. R. Knight, R. J. Allan, C. K. Folland, M. Vellinga, and M. E. Mann. A signature of persistent natural thermohaline circulation cycles in observed climate. *Geophysical Research Letters*, 32:L20708, 2005.

J. R. Knight, C. K. Folland, and A. A. Scaife. Climate impacts of the Atlantic Multidecadal Oscillation. *Geophysical Research Letters*, 33:L17706, 2006.

R. Knutti, J. Flückiger, T. Stocker, and A. Timmermann. Strong hemispheric coupling of glacial climate through freshwater discharge and ocean circulation. *Nature*, 430: 851–856, 2004.

C. Kuehn. A mathematical framework for critical transitions: Bifurcations, fast–slow systems and stochastic dynamics. *Physica D-Nonlinear Phenomena*, 240:1020–1035, 2011.

Y. Kushnir. Interdecadal variations in North Atlantic sea surface temperature and associated atmospheric conditions. *Journal Of Physical Oceanography*, 7:141–157, 1994.

N. K. Larkin and D. Harrison. On the definition of El Niño and associated seasonal average us weather anomalies. *Geophysical Research Letters*, 32, 2005.

M. Latif. Dynamics of interdecadal variability in coupled ocean-atmosphere models. *J Climate*, 11:602–624, 1998.

M. Latif and T. P. Barnett. Causes of decadal climate variability over the North Pacific and North America. *Science*, 266:634–637, 1994.

D. Legler and J. O'Brien. Tropical Pacific Wind Stress Analysis for TOGA. *Intergovernmental Oceanographic Commission*, pages 1–11, 1988.

T. M. Lenton. Early warning of climate tipping points. *Nature Publishing Group*, 1: 201–209, 2011.

T. M. Lenton, H. Held, E. Kriegler, J. W. Hall, W. Lucht, S. Rahmstorf, and H. J. Schellnhuber. Tipping elements in the earth's climate system. *Proceedings of the National Academy of Sciences*, 105:1786–1793, 2008.

T. Lenton, V. Livina, V. Dakos, and M. Scheffer. Climate bifurcation during the last deglaciation? *Climate of the Past*, 8:1127–1139, 2012.

A. Levermann, A. Griesel, M. Hofmann, M. Montoya, and S. Rahmstorf. Dynamic sea level changes following changes in the thermohaline circulation. *Climate Dynamics*, 24:347–354, 2005.

T. Lian, D. Chen, Y. Tang, and Q. Wu. Effects of westerly wind bursts on El Niño: A new perspective. *Geophysical Research Letters*, 41:3522–3527, 2014.

V. N. Livina and T. M. Lenton. A modified method for detecting incipient bifurcations in a dynamical system. *Geophysical Research Letters*, 34, 2007.

V. N. Livina, F. Kwasniok, G. Lohmann, J. W. Kantelhardt, and T. M. Lenton. Changing climate states and stability: from Pliocene to present. *Climate Dynamics*, 37:2437–2453, 2011.

V. N. Livina, F. Kwasniok, and T. M. Lenton. Potential analysis reveals changing number of climate states during the last 60 kyr. *Climate Of The Past*, 6:77–82, 2010.

J. F. Lübbecke and M. J. McPhaden. A comparative stability analysis of Atlantic and Pacific Niño modes. *Journal of Climate*, 26:5965–5980, 2013.

J. Ludescher, A. Gozolchiani, M. I. Bogachev, A. Bunde, S. Havlin, and H. J. Schellnhuber. Improved El Niño forecasting by cooperativity detection. *Proceedings of the National Academy of Sciences*, 110:11742–11745, 2013.

J. Ludescher, A. Gozolchiani, M. I. Bogachev, A. Bunde, S. Havlin, and H. J. Schellnhuber. Very early warning of next El Niño. *Proceedings of the National Academy of Sciences*, 111:2064–2066, 2014.

N. Marwan, J. F. Donges, Y. Zou, R. V. Donner, and J. Kurths. Complex network approach for recurrence analysis of time series. *Physics Letters A*, 373:4246–4254, 2009.

M. J. McPhaden. Genesis and evolution of the 1997-98 El Niño. *Science*, 283:950–954, 1999.

G. A. Meehl, T. F. Stocker, W. D. Collins, P. Friedlingstein, A. T. Gaye, J. M. Gregory, A. Kitoh, R. Knutti, J. M. Murphy, A. Noda, S. C. B. Raper, I. G. Watterson, W. A. J, and Z.-C. Zhao. Global Climate Projections. In *Climate Change 2007: The Physical Science Basis. Contribution of Working Group I to the Fourth Assessment Report of the Intergovernmental Panel on Climate Change [Solomon, S., D. Qin, M. Manning, Z. Chen, M. Marquis, K.B. Averyt, M. Tignor and H.L. Miller (eds.)]*. Cambridge University Press, Cambridge, United Kingdom and New York, NY, USA, 2007.

C. E. Menkes, M. Lengaigne, J. Vialard, M. Puy, P. Marchesiello, S. Cravatte, and G. Cambon. About the role of Westerly Wind Events in the possible development of an El Niño in 2014. *Geophysical Research Letters*, 41:6476–6483, 2014.

M. Mheen, H. A. Dijkstra, A. Gozolchiani, M. den Toom, J. Feng, Q. Kurths, and E. Hernandez-Garcia. Interaction network based early warning indicators for the Atlantic MOC collapse. *Geophysical Research Letters*, 40:2714–2719, 2013.

T. Mitchell. *Machine Learning*. McGraw-Hill, New York, 1997.

V. Moron, R. Vautard, and M. Ghil. Trends, interdecadal and interannual oscillations in global sea-surace temperature. *Clim. Dyn.*, 14:545–569, 1998.

R. A. Muller, J. Curry, D. Groom, R. Jacobsen, S. Perlmutter, R. Rohde, A. Rosenfeld, C. Wickham, and J. Wurtele. Decadal variations in the global atmospheric land temperatures. *Journal of Geophysical Research: Atmospheres*, 118:5280–5286, 2013.

J. Neelin, D. S. Battisti, A. C. Hirst, F.-F. Jin, Y. Wakata, T. Yamagata, and S. E. Zebiak. ENSO Theory. *Journal of Geophysical Research*, 103:14,261–14,290, 1998.

M. Newman. *Networks: an introduction*. Oxford University Press, 2010.

C. Penland. A stochastic model of IndoPacific sea surface temperature anomalies. *Physica D: Nonlinear Phenomena*, 98:534–558, 1996.

S. G. H. Philander. *El Niño and the Southern Oscillation*. Academic Press, New York, 1990.

S. Rahmstorf. On the freshwater forcing and transport of the Atlantic thermohaline circulation. *Climate Dynamics*, 12:799–811, 1996.

S. Rahmstorf. The thermohaline circulation: a system with dangerous thresholds? *Climatic Change*, 46:247–256, 2000.

S. Rahmstorf, M. Crucifix, A. Ganopolski, H. Goosse, I. Kamenkovich, R. Knutti, G. Lohmann, R. Marsh, L. A. Mysak, Z. Wang, and A. J. Weaver. Thermohaline circulation hysteresis: A model intercomparison. *Geophysical Research Letters*, 32: L23605, doi:10.1029/2005GL023655, 2005.

N. A. Rayner, D. E. Parker, E. B. Horton, C. K. Folland, L. V. Alexander, D. P. Rowell, E. C. Kent, and A. Kaplan. Global analyses of sea surface temperature, sea ice, and night marine air temperature since the late nineteenth century. *Journal of Geophysical Research*, 108:10.1029/2002JD002670, 2003a.

N. Rayner, D. Parker, E. Horton, C. Folland, L. Alexander, D. Rowell, E. Kent, and A. Kaplan. Global analyses of sea surface temperature, sea ice, and night marine air temperature since the late nineteenth century. *Journal of Geophysical Research*, 108:4407, 2003b.

B. Reilly. *Disaster and Human History: Case Studies in Nature, Society and Catastrophe*. McFarland, Jefferson, 2009.

M. Roulston and J. Neelin. The response of an ENSO model to climate noise, weather noise and intraseasonal forcing. *Geophys. Res. Letters*, 27:3723–3726, 2000.

D. Rummelhart. Learning representations by back-propagation errors. *Nature*, 323: 533–536, 1986.

S. J. Russell and P. Norvig. *Artificial Intelligence: A Modern Approach*. Pearson Education, 2 edition, 2003.

S. Saha, S. Moorthi, X. Wu, J. Wang, S. Nadiga, P. Tripp, D. Behringer, Y.-T. Hou, H.-y. Chuang, M. Iredell, et al. The ncep climate forecast system version 2. *Journal of Climate*, 27:2185–2208, 2014.

M. Scheffer, J. Bascompte, W. A. Brock, and V. Brovkin. Early-warning signals for critical transitions. *Nature*, 461:53–59, 2009.

M. Scheffer, S. R. Carpenter, T. M. Lenton, J. Bascompte, W. Brock, V. Dakos, J. van de Koppel, I. A. van de Leemput, S. A. Levin, E. H. van Nes, M. Pascual, and J. Vandermeer. Anticipating Critical Transitions. *Science*, 338:344–348, 2012.

M. E. Schlesinger and N. Ramankutty. An oscillation in the global climate system of period 65-70 years. *Nature*, 367:723–726, 1994a.

M. Schlesinger and N. Ramankutty. An oscillation in the global climate system of period 65-70 years. *Nature*, 367:723–726, 1994b.

C.-F. Schleussner, D. Divine, J. Donges, A. Miettinen, and R. Donner. Indications for a north atlantic ocean circulation regime shift at the onset of the little ice age. *Climate Dynamics*, pages 1–11, 2015.

A. Schmittner, M. Latif, and B. Schneider. Model projections of the North Atlantic thermohaline circulation for the 21st century assessed by observations. *Geophys. Res. Letters*, 32:L237108, 2005.

F. Sevellec and A. V. Fedorov. The Leading, Interdecadal Eigenmode of the Atlantic Meridional Overturning Circulation in a Realistic Ocean Model. *Journal Of Climate*, 26:2160–2183, 2013.

N. Sharma, P. Sharma, D. Irwin, and P. Shenoy. Predicting solar generation from weather forecasts using machine learning. In *Smart Grid Communications (SmartGridComm), 2011 IEEE International Conference on*, pages 528–533. IEEE, 2011.

D. A. Smeed, G. McCarthy, S. A. Cunningham, E. Frajka-Williams, D. Rayner, W. E. Johns, C. S. Meinen, M. O. Baringer, B. I. Moat, A. Duchez, and H. L. Bryden. Observed decline of the atlantic meridional overturning circulation 2004 to 2012. *Ocean Science Discussions*, 10:1619–1645, 2013.

T. M. Smith and R. W. Reynolds. Extended reconstruction of global sea surface temperatures based on coads data (1854-1997). *Journal of Climate*, 16:1495–1510, 2003.

K. Steinhaeuser, N. V. Chawla, and A. R. Ganguly. An exploration of climate data using complex networks. *ACM SIGKDD Explorations Newsletter*, 12:25–32, 2010.

V. Stolbova, P. Martin, B. Bookhagen, N. Marwan, and J. Kurths. Topology and seasonal evolution of the network of extreme precipitation over the indian subcontinent and sri lanka. *Nonlinear Processes in Geophysics*, 21:901–917, 2014.

H. Stommel. Thermohaline convection with two stable regimes of flow. *Tellus*, 13: 224–230, 1961.

R. T. Sutton and D. L. Hodson. Atlantic Ocean Forcing of North American and European Summer Climate. *Science*, 309:115–118, 2005a.

R. Sutton and D. Hodson. Atlantic ocean forcing of north american and european summer climate. *Science*, 309:115–118, 2005b.

L. A. Te Raa and H. A. Dijkstra. Instability of the thermohaline ocean circulation on interdecadal timescales. *Journal of physical oceanography*, 32:138–160, 2002.

I. V. Tetko, D. J. Livingstone, and A. I. Luik. Neural network studies. 1. comparison of overfitting and overtraining. *Journal of chemical information and computer sciences*, 35:826–833, 1995.

J. M. T. Thompson and J. Sieber. Predicting Climate Tipping as a Noisy Bifurcation: a Review. *International Journal of Bifurcation and Chaos*, 21:399–423, 2011.

S. Tietsche, D. Notz, J. Jungclaus, and J. Marotzke. Recovery mechanisms of arctic summer sea ice. *Geophysical Research Letters*, 38, 2011.

A. Timmermann, S. An, U. Krebs, and H. Goosse. ENSO suppression due to weakening of the north atlantic thermohaline circulation. *Journal of Climate*, 18:3122–3139, 2005.

M. Ting, Y. Kushnir, R. Seager, and C. Li. Forced and internal twentieth-century sst trends in the north atlantic. *Journal of Climate*, 22:1469–1481, 2009.

C. Tominski, J. F. Donges, and T. Nocke. Information visualization in climate research. In *Information Visualisation (IV), 2011 15th International Conference on*, pages 298–305. IEEE, 2011.

Y. M. Tourre, B. Rajagopalan, and Y. Kushnir. Dominant Patterns of Climate Variability in the Atlantic Ocean during the Last 136 Years. *Journal Of Climate*, 12:2285–2299, 1999.

A. A. Tsonis and P. J. Roebber. The architecture of the climate network. *Physica A: Statistical Mechanics and its Applications*, 333:497–504, 2004.

A. A. Tsonis and K. L. Swanson. What do networks have to do with climate? *Bulletin Of The American Meteorological Society*, 87:585–595, 2006.

A. A. Tsonis and K. L. Swanson. On the origins of decadal climate variability: a network perspective. *Nonlinear Processes in Geophysics*, 19:559–568, 2012.

A. A. Tsonis. Introducing networks in climate studies. In *Nonlinear Dynamics in Geosciences*, pages 1–15. Springer, 2007.

P. C. F. Van der Vaart, H. A. Dijkstra, and F.-F. Jin. The Pacific Cold Tongue and the ENSO mode: Unified theory within the Zebiak-Cane model. *J. Atmos. Sci.*, 57: 967–988, 2000.

M. Vellinga, R. A. Wood, and J. M. Gregory. Processes governing the recovery of a perturbed thermohaline circulation in HadCM3. *J Climate*, 15:764–780, 2002.

M. L. Vianna and V. V. Menezes. Bidecadal sea level modes in the north and south atlantic oceans. *Geophysical Research Letters*, 40:5926–5931, 2013.

A. Von der Heydt, A. Nnafie, and H. Dijkstra. Cold tongue/warm pool and ENSO dynamics in the pliocene. *Climate of the Past*, 7:903–915, 2011.

G. Walin. The thermohaline circulation and the control of ice ages. *Paleogeogr. Paleoclim. Paleoecol.*, 50:323–332, 1985.

J. M. Wallace, T. P. Mitchell, E. Rasmusson, V. Kousky, E. S. Sarachik, and H. Von Storch. On the structure and evolution of ENSO-related climate variability in the Tropical Pacific: lessons from TOGA. *Journal of Geophysical Research*, 103:14,241–14,260, 1998.

Y. Wang, A. Gozolchiani, Y. Ashkenazy, Y. Berezin, O. Guez, and S. Havlin. Dominant imprint of rossby waves in the climate network. *Physical review letters*, 111:138501, 2013.

S. Wasserman. *Social network analysis: Methods and applications*, volume 8. Cambridge university press, 1994.

D. J. Watts and S. H. Strogatz. Collective dynamics of Ôsmall-worldÕnetworks. *nature*, 393:440–442, 1998.

W. Weijer and H. A. Dijkstra. A bifurcation study of the three-dimensional thermohaline ocean circulation: The double hemispheric case. *Journal of Marine Research*, 59:599–631, 2001.

K. Yamasaki, O. Gazit, and S. Havlin. Pattern of climate network blinking links follows El Niño events. *Europhysics Letters*, 2008.

S.-W. Yeh, J.-S. Kug, B. Dewitte, M.-H. Kwon, B. P. Kirtman, and F.-F. Jin. El Niño in a changing climate. *Nature*, 461:511–514, 2009.

Y. Yuan and H. Yan. Different types of La Niña events and different responses of the tropical atmosphere. *Chinese Science Bulletin*, 58:406–415, 2013.

S. E. Zebiak and M. A. Cane. A model El Niño-Southern Oscillation. *Monthly Weather Review*, 115:2262–2278, 1987.

R. Zhang and T. L. Delworth. Impact of Atlantic multidecadal oscillations on India/Sahel rainfall and Atlantic hurricanes. *Geophysical Research Letters*, 33:L17712, 2006.

J. Zou, Y. Han, and S.-S. So. Overview of artificial neural networks. In *Artificial Neural Networks*, pages 14–22. Springer, 2009.

ACKNOWLEDGEMENTS

Being this far, I have a lot of people to thank. However, if I start listing all the names, probably several pages are not enough. Thus, first of all, I apologize that I didn't mention most of you individually, but your help, care and company are definitely deeply thanked in my heart. Thank you for being you these years, my dearest families, friends and colleagues.

Of course, I have to mention a few people who deeply influenced me in pursuing my academic career. First of all are my parents, especially my father. I was very curious about everything when I was a kid, and asked a lot of "why". My father was never bothered by my endless questions, instead he encouraged me to find the answers by myself from books and little experiments. Besides giving me the right guidance in science, my parents also showed enormous understanding towards my choices. I know it is not easy for them to accept the fact that their 24-year-old only child decided to quit her stable new job and go abroad for new studies and a completely different life.

Second, I would like to thank my former supervisor Prof. Lihe Chai at Tianjin University, who imparted the newest knowledge of science, guided me to the "door" of Complexity, and encouraged me to go further. Special thanks to Prof. Robert MacKay and Prof. Robin Ball at the University of Warwick. Without their quick responses to my inquiry about the funding of studying Complexity, I might be still doing the "boring" job just for living. Of course, I have to thank Erasmus Mundus Masters Program in Complex Systems Science to give me such a great opportunity to start my amazing journey in Europe. Although it was not an easy start for me both in life and studies, many thanks to my classmates and all the members in the Centre for Complexity Science in Warwick and in the Insitut des Systemes Complexes in Paris, I made it through with joy.

I also want to thank Marie-Curie Initial Training Network Program in Learning about Interacting Networks in Climate (LINC), which supported my PhD studies and extended my journey from Europe to the world. Via this wonderful program, I worked with and got inspired by lots of intelligent people all over the world, especially our own LINCers, I'm truly thankful for knowing you all.

Another big "thank you" to my PhD supervisor Prof. Henk A. Dijkstra. There is a funny comparison between a PhD and a marriage, I can't agree most of the similarities, but I do believe that to have a successful PhD you need some special chemistry with your supervisor just like with your partner – to build faith in each other of getting good results. Luckily, Henk and I have such chemistry which I must credit to his art of supervision – just enough of guidance and freedom. Besides being a good supervisor, Henk, together with Julia, also give me lots of care like my parents,

I'm really grateful for having such family feeling through work. This family feeling also exists in my current institute IMAU, I'm also grateful for having such a firm "home" base.

Speaking of family, I heartily thank my husband Mark for giving me a real one. Having him is the biggest surprise through my journey in Europe. I even joked about our "anti-fairytale" romance that the girl had to cross the biggest continent in the world, even searched in UK and France, and finally found her Mr. Right in The Netherlands! However, no matter which version our fairytale is, our goal is the same "happily ever after". That's what I learn from Complexity: life is full of surprises (open boundaries), you may have different starting points (initial conditions), but if you work towards one goal under your limits (constraints), and make best usage of your resources from your environment (optimization), you will have a fabulous life.

CURRICULUM VITAE

Educations:

07/2012-06/2015 PhD in Climate Dynamics, Universiteit Utrecht, NL
09/2011-06/2012 MSc in Cognition and Complex Systems, École Polytechnique, FR
10/2010-08/2011 MSc in Complex Systems Science, University of Warwick, UK
09/2008-06/2010 MSc in Environmental Science, Tianjin University, CN
09/2004-06/2008 BSc in Environmental Science, Tianjin University, CN

Academic Experience:

07/2012-06/2015 IMAU, Utrecht University (Collaborated with Marie-Curie Initial Training Network), NL, PhD Researcher
04/2014-05/2014 Secondment in Israel (Collaborated with Bar-Ilan University)
03/2013-04/2013 Secondment in Germany (Collaborated with Potsdam Institute for Climate Impact Research)

- Developed new mechanistic indicators based on network analysis, which are crucially important in the interpretation and evaluation of climate models and observations.

03/2011-12/2012 Diamond Cohort Study, University of Warwick (Collaborated with The University of Melbourne), UK, Junior Researcher

- Introduced a new way to identify depression patterns based on information theory and machine learning, which may lead to tailored medical interventions for depression.

01/2012-06/2012 U943 INSERM, Université Pierre et Marie Curie (Collaborated with École Polytechnique), FR, Junior Researcher

- Proposed a more comprehensive measure to capture the full picture of HIV epidemic based on nonlinear dynamic modeling, which can be used to estimate HIV transmission at the population level and the risk of HIV acquisition at the individual level.

02/2007-10/2010 National Basic Research Program & National Natural Science Foundation, Tianjin University, CN, Student Researcher

- Proposed several new models for complex systems based on multivariate statistics and statistical mechanics, which have been applied in ecosystems and economics.

Publications Included in this Thesis:

1. J. F. Donges, J. Heitzig, B. Beronov, M. Wiedermann, J. Runge, **Q. Y. Feng**, L. Tupikina, V. Stolbova, R. V. Donner, N. Marwan, H. A. Dijkstra, and J. Kurths. Unified Functional Network and Nonlinear Time Series Analysis for Complex Systems Science: The `pyunicorn` Package. *Chaos: An Interdisciplinary Journal of Nonlinear Science*, 2015 (resubmitted).
2. M. Van der Mheen, H. A. Dijkstra, A. Gozolchiani, M. Den Toom, **Q. Feng**, J. Kurths, and E. Hernandez-Garcia. Interaction network based early warning indicators for the Atlantic MOC collapse. *Geophysical Research Letters*, 2013, 40(11): 2714-2719.
3. **Q. Y. Feng**, J. P. Viebahn, and H. A. Dijkstra. Deep Ocean Early Warning Signals of an Atlantic MOC Collapse. *Geophysical Research Letters*, 2014, 41(16): 6009-6015.
4. **Q. Y. Feng**, and H. A. Dijkstra. Are North Atlantic Multidecadal SST Anomalies Westward Propagating? *Geophysical Research Letters*, 2014, 41(2): 541-546.
5. **Q. Y. Feng**, and H. A. Dijkstra. Climate Network Based Stability Index for El Niño Variability. *Geophysical Research Letters*, 2015 (resubmitted).
6. **Q. Y. Feng**, R. Vasile, M. Segond, A. Gozolchiani, Y. Wang, A. Tantet, M. Abel, S. Havlin, A. Bunde, and H. A. Dijkstra. Improving the Skill of El Niño Predictions Using Machine Learning Techniques and Network Measures. *Geoscientific Model Development*, 2015 (submitted).

Other Publications:

7. **Q. Y. Feng**, F. Griffiths, N. Parsons, and J. Gunn. An Exploratory Statistical Approach to Depression Pattern Identification. *Physica A: Statistical Mechanics and its Applications*, 2012, 392(4): 889-901.
8. Y. J. Wang, **Q. Y. Feng**, and L. H. Chai. Structural Evolutions of Stock Markets Controlled by Generalized Entropy Principles of Complex Systems. *International Journal of Modern Physics B*, 2010, 30(24): 5949-5971.

9. **Q. Y. Feng**, and L. H. Chai. A New Statistical Dynamic Analysis on Vegetation Patterns in Land Ecosystems. *Physica A: Statistical Mechanics and its Applications*, 2008, 387(14): 3583-3593.

10. Y. J. Wang, **Q. Y. Feng**, H. Wang, and L. H. Chai. New Simulation Method of Ecosystem Evolution Based on Neural Network. *In: 6th International Conference on Natural Computation (ICNC10) Vol.4*, Yantai, China: 2010. 1749-1753.

11. Y. J.Wang, **Q. Y. Feng**, S. J. Chen, and L. H. Chai. Simulation of Transportation-Economic Complex System Based on SOM Network. *In: 6th International Conference on Natural Computation (ICNC10) Vol.4*, Yantai, China: 2010. 1842-1846.

12. Y. J. Wang, **Q. Y. Feng**, and L. H. Chai. A New Model on Origin and Evolution of Biology (In English & Chinese). *Agricultural Science & Technology*, 2009,10(4): 4-7.

13. Y. J. Wang, **Q. Y. Feng**, and L. H. Chai. Evolution of Stock Markets Driven by Generalized Entropy Principles (In Chinese). *Journal of Tianjin University of Technology*, 2009, 25(5): 8-11.

14. **Q. Y. Feng**, and L. H. Chai. Ecosystem Evolution Dynamics Based on Generalized Entropy Principle (In Chinese). *Science & Technology Review*, 2009, 27(4): 36-41.

15. **Q. Y. Feng**, and L. H. Chai. Maximum Flux Principle: A New Method of Multivariate Statistical Analysis and Its Applications (In Chinese). *Journal of Tianjin University of Technology*, 2009, 25(1): 15-19.

16. **Q. Y. Feng**, and L. H. Chai. Riddle of Growth: A Principle for Growth Basing on Non Equilibrium Statistical Mechanics (In Chinese). *Science & Technology Review*, 2008, 26(4): 80-86.

17. **Q. Y. Feng**, and L. H. Chai. The Function Law of Nature: The Research Progress of Maximum Flux Principle (In Chinese). *Science & Technology Review*, 2007, 25(24): 73-80.

For a complete up-to-date list of publications, please visit `http://www.uu.nl/medewerkers/QFeng`

This document was typeset using `classicthesis` developed by André Miede.